CRYSTAL-SPECIFIC INSIGHTS FROM RHYOLITE ERUPTIVE DEPOSITS INTO VOLATILE ELEMENT TRANSFER IN THE MAGMATIC SYSTEM BELOW TAUPŌ VOLCANO

Max S. Sharpe

A thesis submitted to Victoria University of Wellington in
partial fulfilment of the requirements for the degree of
Master of Science in Geology

Victoria University of Wellington
School of Geography, Environment and Earth Sciences
Thesis Advisors: Dr Simon J. Barker, Prof Colin J.N. Wilson, Dr Isabelle Chambefort

Wellington, New Zealand

May 2019

ABSTRACT

Knowledge on the chemical pathways of volatiles in large silicic magmatic systems, from the parental mantle-derived mafic magmas to their more evolved silicic derivatives, is central to understanding a range of topics from magmatic processes through to the climate impacts of volcanism, as well as geothermal and ore resources. However, establishing the pre-eruptive volatile contents of magma from silicic eruptive deposits requires capturing the intermediate steps of the magmatic evolution. The concentrations of sulfur, chlorine, and fluorine were investigated in selected deposits from Taupō volcano: (1) silicic groundmass glass and microphenocryst apatite that equilibrated in the shallow melt-dominant magma body; (2) silicic melt and apatite inclusions sourced from deeper in the crystal mush; and (3) olivine-hosted basaltic melt inclusions representing the most primitive magmas. *In-situ* geochemical analyses were carried out on orthopyroxene and apatite from the Oruanui supereruption, orthopyroxene from post-Oruanui dacites and rhyolites, and high-Mg olivine from Taupō basaltic-andesite. The volatile contents at each stage reveal unique magmatic volatile pathways from the source magmas through to the silicic system, that are primarily a function of intensive parameters (pressure, temperature, oxygen fugacity), crystallising mineral phases, and the presence of an aqueous fluid phase. The relatively high sulfur contents in the basalts drop by ~2000 ppm to near detection limits in dacitic compositions due to pyrrhotite crystallisation during the magnetite crisis. In contrast, chlorine increases from basaltic to dacitic compositions, due to the incompatibility of chlorine in magmatic minerals. Fluorine values are similar between basaltic and dacitic-rhyolitic compositions, primarily controlled by the onset of amphibole/apatite crystallisation. Sulfur and chlorine are both inferred to partition strongly into an aqueous vapour across the whole range of silicic compositions analysed. Volatile pathways within the silicic magmas are faithfully recorded in apatite compositions, which can be a valuable petrological tool for assessing magmatic processes.

ACKNOWLEDGEMENTS

Although my time in Wellington has only just clocked two years, there are several people from the department (and further abroad!) that have made this experience so much richer. First and foremost, I would like to thank my supervisors. Simon – you were an endless help, from the volc lab through to the laser, you were always making yourself available for my constant queries. Colin – it has been an eye-opening experience to see the work that goes on at the top, and I am very thankful for the time you always seemed to be able to spare to edit my writing. Isabelle – my long distance correspondence skills were considerably poor but your trips down to VUW and subsequent discussions more than made up for my attempts at regular communication. Collectively the mad scramble of editing by you all (deeply sorry) completely re-shaped this work, for which I am highly appreciative.

Another large thank you goes out to Ian. I pestered you so much about various probe-related issues, but you were always helpful and willing. Despite all the times it screwed up on me, I've almost developed a soft spo… no. I hate that damn machine. Kudos to you Ian for putting up with successive generations of students on it. Also, Dr. Edwin (setting me up with all of my lab work at the start of the year), Hannah (I remember you did something for me and asked to be acknowledged), and Bruce (laser and fielding random questions) were each a great help.

I probably would have either starved or lived out of the internal room in the JB library if I weren't the grateful recipient of the W.R. Lauder Memorial Scholarship, for which I am very thankful. Further support from Isabelle, Colin, and the SGEES was also very much appreciated, as otherwise I would not have been able to conduct this research!

Although I didn't go through the seemingly silty undergraduate geology degree at VUW, everyone in the School of Rock was very quick to say g'day and make friends, so cheers to everyone, you all know who you are! A massive thank you also goes out to Mitch Keenan and Dr Withrington, whose added insights, ideas, critiquing, and support kept this thesis alive.

Also, thanks to mum, dad, and Smeloise. It was great living in the same island again for constant trips home. You've always encouraged me to do what I want, and so I know you cannot wait to dive into the analytical methods with fervour and see what it's all about…

Table of Contents

LIST OF FIGURES

LIST OF TABLES

1. Introduction

1.1 Motivation for research

Large silicic magma systems exhibit enormous variability in terms of the processes that define their behaviour, from the flux of primitive mantle-sourced mafic magmas to the magma-biosphere interactions that occur during volcanic eruptions. However there are many challenges involved with interpreting these diverse processes, with global examples displaying broad differences in total eruptive volume, magma composition, and the frequency of volcanic events. One problem that is of significant interest is constraining the behaviour of the volatile components (e.g. H_2O, CO_2, S, Cl, F) within large silicic magma systems. Characterised by their tendency to remain incompatible in both silicate melt and associated minerals, the volatile components of a magma typically exsolve from an evolving melt, driven by magmatic decompression and fractional crystallisation (Edmonds and Wallace, 2017). Through preferential partitioning into a coexisting volatile phase, the volatile components of a silicic melt exert significant controls on geologic processes (e.g. metasomatism; magma ascent, degassing, and eruption; and shallow crust hydrothermal mineralisation: Mungall, 2003; Webster and Botcharnikov, 2011; Edmonds and Wallace, 2017). Sulfur, chlorine, and fluorine are three such volatile elements that can affect a broad range of these processes, and will be the focus of this thesis. However, there are difficulties in measuring these elements, as studies of whole-rock and groundmass glass compositions often give lower than anticipated volatile estimates. These depleted values are inferred to represent syn-eruptive degassing (Oppenheimer, 2003, and references therein). This concept is particularly true for sulfur, which is far less soluble in the melt than either chlorine or fluorine at shallow crustal pressures (Scaillet et al., 1998; Wallace and Edmonds, 2011; Zajacz et al., 2012). Estimating original pre-eruptive volatile contents requires direct analyses of melt, volatile-accommodating hydrous minerals (e.g. apatite), or exsolving volatile-rich phases, without any re-equilibration through elemental diffusion, decompression, or crystallisation. This can be achieved through targeting melt, fluid, and mineral inclusions, but it is not always possible to ascertain whether or not these phases represent genuine pre-eruptive magmatic

compositions (Lowenstern, 1995). Textural and compositional studies can aid in this dilemma by accurately constraining the magmatic history for the host crystal of a melt, fluid, or mineral inclusion, and can provide clues into where in the magmatic system the included phase may have originated.

Among global rhyolitic magma systems, the central Taupō Volcanic Zone (TVZ) stands out for its productivity and frequency of eruptions (Houghton et al., 1995; Wilson et al., 1995, 2009). The stratigraphic framework of eruptive deposits from Taupō volcano and the processes by which the system can remobilise magma and erupt on relatively rapid timescales have been the subject of many studies over recent decades (e.g. Wilson, 1993; Wilson, 2001; Sutton et al., 1995, 2000; Charlier et al., 2005, 2008; Wilson and Charlier, 2009; Allan et al., 2012, 2013, 2017; Barker et al., 2014, 2015, 2016), which have contributed towards a high resolution petrologic reconstruction of the large silicic magmatic system. However, there is currently a limited understanding of the way in which sulfur, chlorine, and fluorine are transported through the magmatic system. Thus Taupō is an excellent volcano on which to investigate the transport and behaviour of volatile elements within the subsurface silicic magma system, knowledge of which is important for understanding a range of topics from magmatic processes through to the potential climate impacts of large rhyolitic eruptions.

1.2 Thesis objectives and outline

Previous studies investigating the volatile contents of Taupō volcano and the wider Taupō Volcanic Zone through melt inclusion-specific studies have reported sulfur contents below equipment detection limits (Dunbar et al., 1989a; Dunbar and Kyle, 1993; Johnson et al., 2011; Bégué et al 2015a, 2015b). However these studies tended to focus primarily on quartz-hosted melt inclusions, with a smaller suite of analyses conducted on plagioclase-hosted melt inclusions. Quartz is inferred to be a late-crystallising phase in Taupō magma system, and is inferred to not be stable until near the upper section of the system (120-150 MPa: Liu et al., 2006; Allan, 2013). Therefore it is likely that the melt hosted in quartz crystals represents a region of the system in

which a sulfur-rich phase has already exsolved. A potential solution to this problem lies in the crystal-specific textural and compositional investigations of eruptive deposits from Taupō volcano (Charlier et al., 2008; Allan et al., 2013, 2017; Barker et al., 2015). The majority of orthopyroxene and plagioclase crystal cores are inferred to have grown from a range of pressures within the deeper magmatic system (~140-270 MPa), whereas the outermost rims represent much more evolved melt conditions that grew at shallow crustal levels (~90-140 MPa: Allan et al., 2017). The orthopyroxene cores in particular are rich in melt and mineral inclusions. Therefore it is inferred that targeting and analysing the volatile compositions of the melt and mineral inclusions within orthopyroxene cores, and comparing these values to those from groundmass glass analyses, may better constrain melt volatile compositions from a range of depths through the magma system beneath Taupō volcano. In addition to melt inclusions, apatite is ubiquitously distributed throughout the inherited orthopyroxene cores, and also as a microphenocryst phase in the groundmass glass. Comparison of the volatile contents of the two apatite crystal populations can be used to supplement that of the melt inclusions. Furthermore, the occurrence of juvenile basaltic inclusions within Taupō rhyolite eruptives provides a window into the deep mafic system and the starting composition of primitive magmas that feed the crustal magmatic reservoir (Allan et al., 2017; Simon Barker, pers. comm, 2019).

The overall aim of this thesis is to better constrain the behaviour, transport, and loss of sulfur, chlorine, and fluorine in the magmatic plumbing system beneath Taupō volcano, and to propose a volatile pathway model that describes the evolution of each element through the system, from the deep mafic feeder zone though to the shallowest region of the silicic mush system. The key objectives for this study are as follows:

1. Record the abundances and distributions of sulfur, chlorine, and fluorine in the silicic system, both from melt and apatite inclusions hosted in inherited crystal cores, and from groundmass glass and microphenocryst apatite.
2. Compare the volatile compositions between the melt and apatite equilibrated at depth in the mush system with the shallower groundmass glass and microphenocryst apatite.

3. Compare the volatile compositions of the silicic system with the deeper mafic reservoir by investigating sulfur, chlorine, and fluorine in olivine-hosted melt inclusions from mafic enclaves in the rhyolite eruptives.
4. Establish the nature of the volatile pathway through the entire magmatic system below Taupō volcano, and constrain the processes by which S, Cl, and F are partitioned between melt, magmatic fluid(s), and mineral phases.

These objectives are explored throughout five chapters, which are outlined below:

Chapter 1 introduces the aims and central themes of the thesis, and provides context for the study. The geologic background to the Taupō Volcanic Zone is outlined, Taupō volcano and the studied eruptions are introduced, and the prior research that has provided the basis for this thesis is summarised.

Chapter 2 outlines the methodologies involved for preparing and analysing glass, and orthopyroxene and apatite crystals with EPMA and LA-ICP-MS.

Chapter 3 presents new glass major and trace element data from several Taupō volcano eruptions, expanding existing data sets. Additionally the first major and trace element data for apatite crystals from Taupō volcano are presented.

Chapter 4 forms an extended discussion that integrates the new data sets from glass and apatite crystals presented in this study. The partitioning behaviours of S, Cl, and F in the system rhyolite melt-fluid(s)-sulfide/apatite are addressed in the context of Taupō volcano, and a model for the transport and evolution of the volatile components is presented.

Chapter 5 presents the main conclusions of this work and considers areas for future research.

1.3 Silicic magmatic systems

Highly evolved silicic magma systems have been suggested to form and accumulate through a variety of processes, including: (1) sequential fractional crystallisation of more primitive mantle-derived magmas (e.g. Hildreth, 1981; Marsh, 1981); (2) partial melting of a less evolved protolith on small scales (e.g. Sisson et al., 2005; Streck and Grunder, 2008; Streck, 2014; (3) assimilation of country rock by lesser evolved magma through large-scale partial melting and/or physical mixing (e.g. Hildreth and Moorbath, 1988; Bindeman and Simakin, 2014). Regardless of the process, the generation of large-volume evolved silicic magmas is associated with the presence of significantly larger quantities of a less evolved crystal-rich residuum. Despite this fact, many eruptive deposits associated with large silicic eruptions are crystal poor (Bachmann and Bergantz, 2004; Wilson et al., 2006; Streck and Grunder, 2008; Allan et al., 2017).

The mechanism by which large volumes of melt-dominant silicic magma and an associated dense crystal residue decouple is difficult to constrain, as melt viscosity increases with increasing melt evolution, leading to less efficient crystal-melt separation (Whittington et al., 2009). Suggested methods of crystal extraction from magma (e.g. gravitational settling: Martin and Nokes, 1988) are too inefficient in terms of magma reservoir size and time required to create eruptible silicic magma (e.g. Hawkesworth et al., 2000; Eichelberger et al., 2006). However, approaching the problem from a different angle led to the crystal mush model, which proposes that silicic melt-dominant magma is extracted from a crystal-rich residue, or mush (Figure 1.1: see Bachmann and Bergantz, 2004; Hildreth, 2004 for overviews). The mush reservoirs beneath silicic volcanic centres are inferred to be composed of compositionally intermediate, uneruptible magma, which is zoned with respect to composition, temperature, and crystallinity (Hildreth, 1981). The generation and removal of eruptible melt from such a mush reservoir is intricately linked to the degree of crystallisation. At low (<45 vol%) crystallinity, the reservoir can circulate relatively freely with the crystals held in a chaotic suspension. Although the bulk composition of the magma is broadly intermediate in composition, crystallisation drives the interstitial melt towards increasingly silicic compositions. Once the crystallinity increases above a critical threshold (>45-60 vol%: Vigneresse et al., 1996) the mush becomes

rheologically locked through a rapid increase in viscosity, but the crystal network is still permeable enough to allow percolation of the interstitial melt. The method by which melt plus crystals is extracted from such a mush zone and subsequently accumulated at shallow crustal levels is not completely understood (see Bachmann and Bergantz, 2008, Allan et al., 2013, 2017; Streck 2014; Bachmann and Huber, 2016 for various discussions). Regardless of the process, it is clear that the crystal mush regions of a silicic system operate on long time scales (e.g. 10^4-10^5 years: Cole et al., 2014), whereas the accumulation of eruptible melt-dominant bodies are thought to be transient events, with crystallisation back into mush occurring on timescales of 10^2-10^3 years (e.g. Allan et al., 2017).

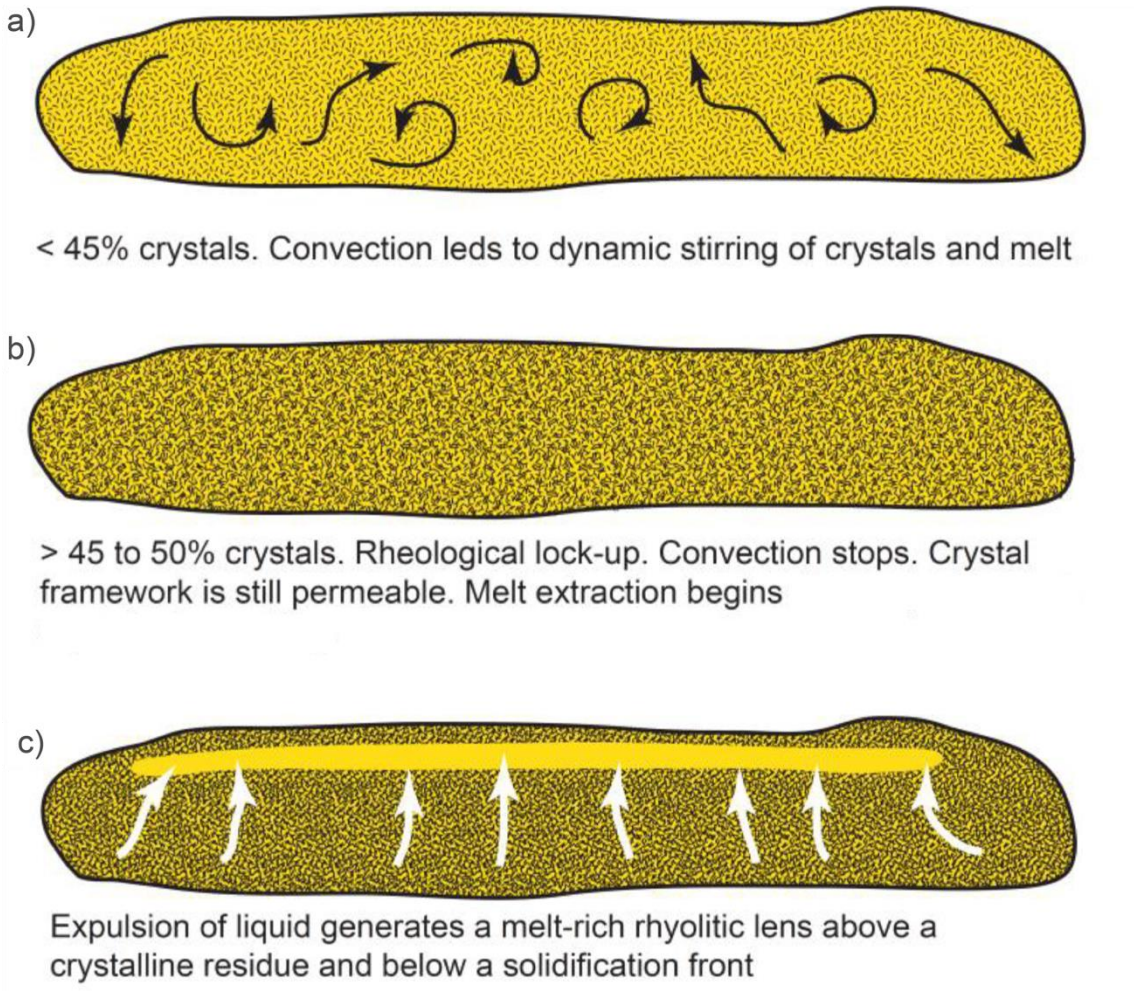

Figure 1.1. Schematic illustration of the crystal mush model. **a)** Convection of a compositionally intermediate magma <45 vol% crystallinity keeps crystals in suspension. **b)** Gradual cooling and crystallisation leads to >45-60 vol% crystallinity, where the crystals form an interlocking network containing interstitial residual silicate melt. Convection is impeded. **c)** Silicate melt is extracted from the mush through several possible processes. A rhyolitic melt-dominant lens forms above the crystalline mush and below a crystallising roof zone. Figure modified from Allan (2013) after Bachmann and Bergantz (2004).

1.4 Sulfur, chlorine, fluorine: behaviour and analysis

The most significant components of global magmatic volatile budgets are H_2O, CO_2, S, Cl, and F (Webster and Botcharnikov, 2011, and references therein). All of these components can play important and distinct roles in the formation, evolution, and eruption of magma (Wallace and Edmonds, 2011). Improving the current state of knowledge on volatile behaviour can help with understanding the flux of volatiles through subduction systems, the explosive behaviour of volcanoes, and the flux of gaseous species to the atmosphere (Wallace and Edmonds, 2011). However S, Cl, and F have further controls on the partitioning and associated fluxes of metals between silicate melt, sulfide-, chloride-, or fluoride-phases, and associated vapour or hypersaline liquid (brine) phases (Zhu and Sverjensky, 1991; Sillitoe and Hedenquist, 2003; Webster, 2004; Wallace and Edmonds, 2011). Many ore metals display a strong affinity for S-complexes (e.g. immiscible sulfide liquids: Mungall, 2003; Webster and Botcharnikov, 2011), and aqueous halide complexes (Burnham, 1979; Webster, 1997; Webster et al., 1999). In addition, the emission of volatile components can have significant environmental consequences. For example, the potential for sulfur to shape global climate through large volcanic eruptions has been well documented, with clouds of sulfate aerosol particles affecting the Earth's radiation balance and leading to extended periods of global cooling (Devine et al., 1984; Graf et al., 1997; Robock 2000).

In silicic systems fed by subduction zone magmas, the main contributions to the S, Cl, and F budget are thought to come ultimately from the subducting slab. Arc magmas typically have enriched S, Cl, and F contents relative to N-MORBs (Woodhead et al., 1987; Wallace and Edmonds, 2011; Jenner and O'Neill, 2012; Dalou et al., 2014), which is thought to occur through contributions from subducting oceanic crust altered by interaction with seawater (Pyle and Mather, 2009, and references therein). The processes by which sulfur and chlorine are added to the overlying mantle wedge are thought to be related to the high affinity of both elements for aqueous phases. As such the main control on enrichment of the mantle wedge in S and Cl is considered to be dewatering of the subducting slab and ascent of the resulting fluids (Brenan 1994; Philippot et al., 1998; Straub and Layne, 2003; Scambelluri et al., 2004; Wallace, 2005; Bonifacie et al., 2008; Marschall et al., 2009; John et al., 2011). The enriched levels of

fluorine in subduction-derived basaltic melts relative to N-MORB, however, are harder to explain due to the deviation of F from typical volatile behaviour. Despite both F and Cl being classified as volatile halogens, there is a difference in ionic radii between the two which allows the substitution of F^- for O^{2-} and OH^- in mineral phases to a far greater extent than Cl^- (Figure 1.2: Dolejš and Zacjacs, 2018). This atomic difference leads to a greater solubility of F in silicate melts and the hydrous minerals such as apatite and amphibole, and a far lower preference for aqueous phases relative to Cl (e.g. Bureau and Keppler, 1999). Suggested processes by which F is enriched in the mantle wedge include: (1) younger subducting slabs with higher temperatures, leading to melting-induced F mobilisation (Van den Bleeken and Koga, 2015); and (2) percolation of fluids derived from the breakdown of F-accommodating minerals (e.g. biotite, amphibole: Dolejš and Zajacz, 2018) through overlying mantle wedge basalts (Urann et al., 2017, and references therein).

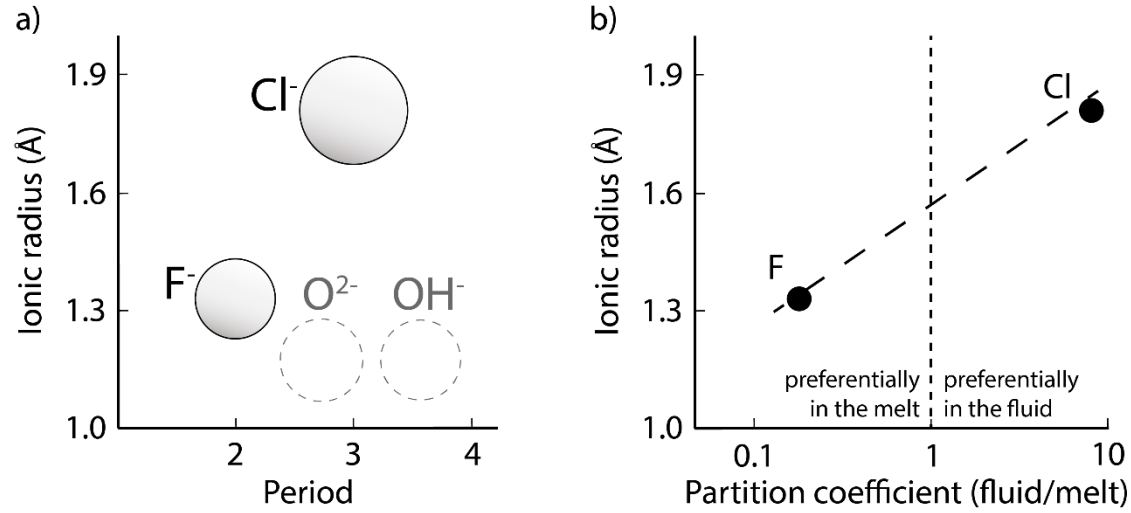

Figure 1. 2. a) Ionic radius (Å) versus period of the periodic table detailing the difference in ionic size between F^- and Cl^-. **b)** Ionic radius (Å) versus typical partitioning coefficients (fluid/silicate melt) for fluorine and chlorine. Modified from Dolejš and Zajacz (2018).

1.4.1 Sulfur

The multiple oxidation states of sulfur (S^{2-}, S^0, S^{4+}, S^{6+}) allow it to take part in a large range of geochemical processes. However S is predominantly present as either sulfide (S^{2-}) or sulfate (SO_4^{2-}) when dissolved in silicate magmas, whereas the predominant magmatic gaseous species are H_2S, SO_2, and S_2 (Fincham and Richardson, 1954;

Clemente et al., 2004). The ratio of sulfate to sulfide speciation is dependent on several factors (e.g. temperature, pressure, melt composition), but is chiefly controlled by the redox state of the magma. Under reduced conditions sulfide is the principal species, whereas under oxidised conditions sulfate is the principal species (for high-silica magmas the transition from reduced to oxidised conditions typically occurs near the nickel-nickel oxide [NNO] buffer: Figure 1.3: Fincham and Richardson, 1954; Carroll and Rutherford, 1985, 1987; Clemente et al., 2004; Behrens and Gaillard, 2006; Métrich and Mandeville, 2010; Baker and Moretti, 2011; Wilke et al., 2011). How much sulfur the melt can hold before reaching saturation (i.e. sulfur concentration at sulfide saturation [SCSS], or at anhydrite saturation [SCAS]: Jugo, 2009) is highly dependent on the oxygen fugacity. Under oxidised conditions sulfur solubility in the melt tends to be considerably higher than under reduced (Scaillet et al., 1998; Keppler, 2010; Baker and Moretti, 2011; Binder et al., 2018). However the values of SCSS and SCAS are also affected by temperature and melt composition, in that the sulfur solubility of a magma will decrease with a cooling, increasingly silicic magma (Fincham and Richardson, 1954; Wendlandt, 1982; Liu et al., 2007).

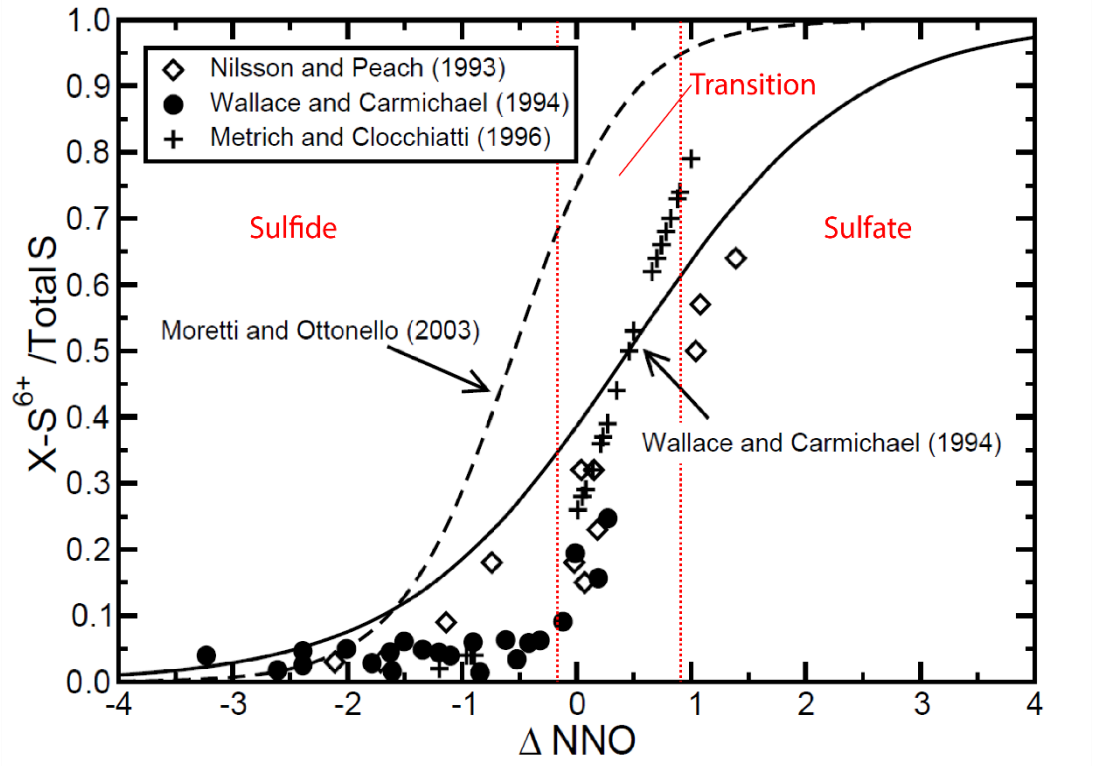

Figure 1. 3. The mol fraction of total sulfur as S^{6+} in melts as a function of the difference between the fO_2 of the melt and the fO_2 of the NNO mineral redox buffer. Also shown are expected S^{6+}/S^T vs ΔNNO from experimental studies. The red dotted lines delineate the transition from sulfide to sulfate. Modified from Baker and Moretti (2011).

1.4.2 Chlorine

In the absence of a magmatic fluid phase, the chlorine solubility of a melt is expected to behave predictably as a melt evolves (Carroll and Webster, 1994). With increasing silica and decreasing Ca/Mg/Fe/Na in a melt, the amount of total dissolved Cl the melt can hold decreases linearly (Liu et al., 2007). However Cl has an affinity for magmatic fluids (e.g. aqueous vapour phase, hypersaline brine) and partitions readily into them over a co-existing melt phase. In hydrous magmatic systems (e.g. Taupō) the Cl/H_2O value of the melt is indicative of what type of fluid phase will saturate within the melt. Cl/H_2O values less than 0.35 and 0.05 for intermediate and felsic compositions at 200 MPa respectively suggest that H_2O will saturate in the melt first, exsolving a low-density H_2O-dominant vapour phase into which chlorine will partition. Values exceeding these Cl/H_2O ratios suggest that chlorine will saturate in the melt first instead, exsolving a high-density hypersaline brine phase (Webster, 2004). However, at magmatic temperatures and low crustal pressures (<140 MPa: Webster, 2004, and references within), it is possible for either an aqueous vapour phase or hypersaline brine phase to unmix at the miscibility gap in the system $NaCl\text{-}H_2O$, forming two separate phases.

1.4.3 Fluorine

In contrast to both sulfur and chlorine, fluorine is highly soluble in silicate melts relative to magmatic fluid phases, and is thus expected to be retained in the melt through the differentiation, ascent, and degassing of fluid-saturated magmas (Aiuppa et al., 2009; Dolejš and Zajacz, 2018). Published fluid/melt partitioning coefficients for fluorine are <0.4 at magmatic temperatures and pressures (London et al., 1988; Webster 1990; Webster and Holloway, 1990; Dolejš and Baker, 2007). Fluorine does, however, substitute readily for O^{2-} and OH^- in hydrous minerals such as apatite, amphibole and biotite, and these minerals can comprise a significant component of the fluorine budget in magmatic systems (Dolejš and Zajacz, 2018). There have been many studies investigating the relationships between fluorine in apatite and a range of silicate melt compositions (e.g. Zhu and Sverjensky, 1991; Piccoli and Candela, 2002;

Mathez and Webster, 2005; Webster et al., 2009, 2017; Doherty et al., 2014), but little work has gone into fluorine partitioning between amphibole and silicic melt, although experimentally derived partition coefficients for hydrous andesitic to dacitic compositions do indicate that fluorine is preferentially incorporated into amphibole (e.g. Van den Bleeken and Koga, 2015). A significant area of concern in constraining fluorine partitioning coefficients between different phases in silicic melts, however, is the error involved with the analysis of F (and Cl) in apatite, and F in glass (Potts and Tindle, 1989; Stormer et al., 1993; Zhang et al., 2016). There have been significant improvements in analytical technique for both of these phases in recent years (e.g. Witter and Kuehner, 2004; Zhang et al., 2016), but many of the most relevant studies in fluorine partitioning were conducted prior to the latest error-reducing techniques (e.g. Mathez and Webster, 2005; Webster et al., 2009; Doherty et al., 2014). Thus care has to be taken when applying F partitioning models to unknown datasets, especially those characterised by relatively low F contents.

1.4.4 Volatile analysis

The most common method to infer the pre-eruptive volatile contents from an eruptive deposit is to analyse melt inclusions hosted in the crystal phases. Melt inclusions are small (generally <100 μm) aliquots of pre-eruptive melt trapped during crystallisation by crystal growth (Figure 1.4) (Qin et al., 1992; Lowenstern, 2003; De Vivo et al., 2005). Once confined within the host crystal the melt pocket is theoretically sealed off, preventing any re-equilibration with the surrounding melt (Qin et al., 1992; Sobolev, 1996). The level to which the melt phase composition remains unchanged is a function of the gradients and concentrations of specific elements in the host mineral and their diffusion coefficients (Qin et al., 1992; Sobolev, 1996). Elements that are incompatible in a mineral have a much reduced capacity for diffusion transport than elements readily taken in to the host mineral (Qin et al., 1992). Chlorine, sulfur and fluorine are all highly incompatible in orthopyroxene, the host mineral phase targeted in this study (Luth, 2003; Joachim et al., 2015; Marzoli et al., 2015; McCubbin et al., 2015).

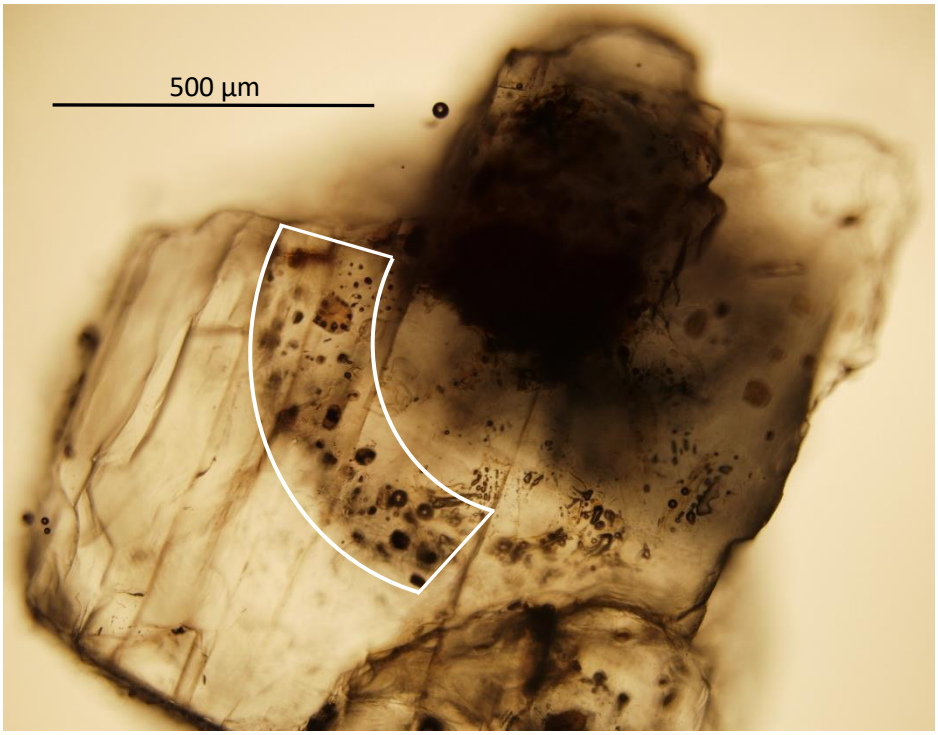

Figure 1. 4. Image of a plagioclase crystal (plane polarised light) with a crystal growth zone delineated by melt inclusions highlighted with white lines.

Although melt inclusions are the only way to infer exact melt compositions, relative changes in volatile elements can also be tracked throughout the magmatic system using volatile-bearing crystal phases. In this regard, apatite has emerged as a key mineral for tracking volatile element behaviour in magmas (e.g. Scott et al., 2015; Webster and Piccoli, 2015; Stock et al., 2018). Apatite is a common accessory phase in silicic magmas (Liu and Comodi, 1993; Piccoli and Candela, 2002), and is typically characterised by three end-members that differ in terms of the 0,0,z anion and its position: fluorapatite, chlorapatite, and hydroxylapatite [$Ca_5(PO_4)_3$(F, Cl, OH)], (Figure 1.5: Hughes and Rakovan, 2002, Marks et al., 2012). Between the three end-members the open structure and chemistry of apatite allows for a large range of elemental substitutions: almost half of the elements in the periodic table can be incorporated within its structure. In magmatic systems fluorapatite is the dominant form of apatite, but it commonly incorporates significant levels of chlorine and minor levels of sulfur through the substitution S + Si = 2P (Piccoli and Candela, 1994, 2002; Peng et al., 1997; Streck and Dilles, 1998; Seifert et al., 2000; Parat et al., 2002; Rønsbo, 2008; Scott et al., 2015; Stock et al., 2018). The primary controls on apatite growth in magmatic

systems are thought to be the concentration of SiO_2 and P_2O_5, and temperature (Watson, 1979). As SiO_2 increases and/or temperature decreases, the melt content of P_2O_5 required to crystallise apatite decreases. Thus apatite has the potential to crystallise constantly from initial crystallisation, even with gradually depleting melt phosphorous contents. Through virtue of its frequent appearance in igneous rocks and its ability to accommodate many different chemically substitutions, apatite is an exceedingly useful mineral to look at volatile evolution through a magmatic crustal system. Trace and rare earth element abundances in magmas can also be significantly altered by the presence of apatite, along with the volatile elements that characterize the three end-members (Hughes and Rakovan, 2002).

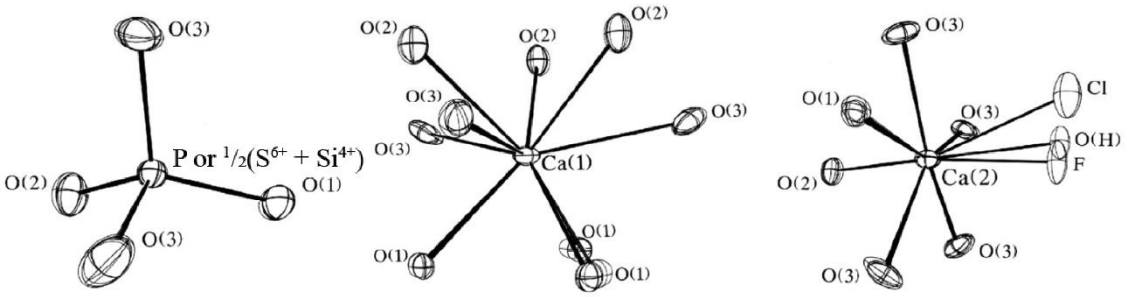

Figure 1. 5. The three cation polyhedral of fluorapatite, chlorapatite, and hydroxylapatite superimposed upon each other. The only notable difference between the three end-members is the positioning of the three substituting anions; F, Cl, and OH. Sourced from Hughes and Rakovan (2002).

The crystallographic structure of apatite results in different patterns of diffusion along its different axes. Experiments investigating the kinetics of volatile exchange within natural fluorapatite found that diffusional zoning gradients develop rapidly along the *c*-axis of apatite, contrasting with a lack of zoning along the *a*-axis (Brenan, 1994). The ambient physical conditions and scale of the zoning can all affect the diffusivity, but under general magmatic conditions, the composition of apatite crystals along the *c*-axis is expected to equilibrate over months to years (Brenan, 1994; Boyce and Hervig, 2008). Due to the analytical constraints on analysis of apatite under an EPMA electron beam (crystals must be oriented parallel to the *c*-axis; Goldoff et al., 2012), only the most recent changes in the halogen composition of an apatite can therefore be recorded. Microphenocryst apatites of a large silicic magma system are thus expected

to represent the immediate pre-eruptive volatile contents of the melt-dominant magma body. However the initial halogen composition of apatite contained within another crystal phase is likely to be preserved due to chemical isolation from the magma (Brenan, 1994).

1.5 Geologic background: Taupō Volcanic Zone

1.5.1 Introduction

The Taupō Volcanic Zone (TVZ) is a distinct volcanic region, located in New Zealand's North Island, with a unique geologic setting and history. The TVZ represents the southernmost section of the Tonga-Kermadec arc, where the Pacific Plate is subducted beneath the Australian Plate (Cole and Lewis, 1981; Wilson et al., 1995). It is a NNE-trending region of arc volcanism and rifting that extends from a termination point just SSW of Mount Ruapehu up to the edge of the continental shelf in the north (Figure 1.6). By encompassing all vent sites and caldera structures associated with the strong NNE trend and active during the 2 Ma lifetime of the zone, Wilson et al. (1984) defined the geographical extent of the TVZ to a narrow corridor <60 km wide and 300 km long (200 km onshore). Several studies have separated the TVZ into an andesite arc and a rhyolite-dominated back-arc (e.g. Cole et al., 1995; Giggenbach, 1995; Stern and Benson, 2011). However, Wilson et al. (1995) mapped the temporal and spatial distribution of andesite and rhyolite vents and concluded that there is no separation between an arc and back-arc for either composition, and that the TVZ is a rifting arc. Extension values vary systematically along strike from 0 mm/yr at Ohakune in the south, to 8 mm/yr at Taupō and up to 18 mm/yr at the Bay of Plenty coastline in the north (Rowland and Sibson, 2001; Villamor and Berryman, 2001; Wallace et al., 2004; Rowland et al., 2010, Seebeck et al., 2014).

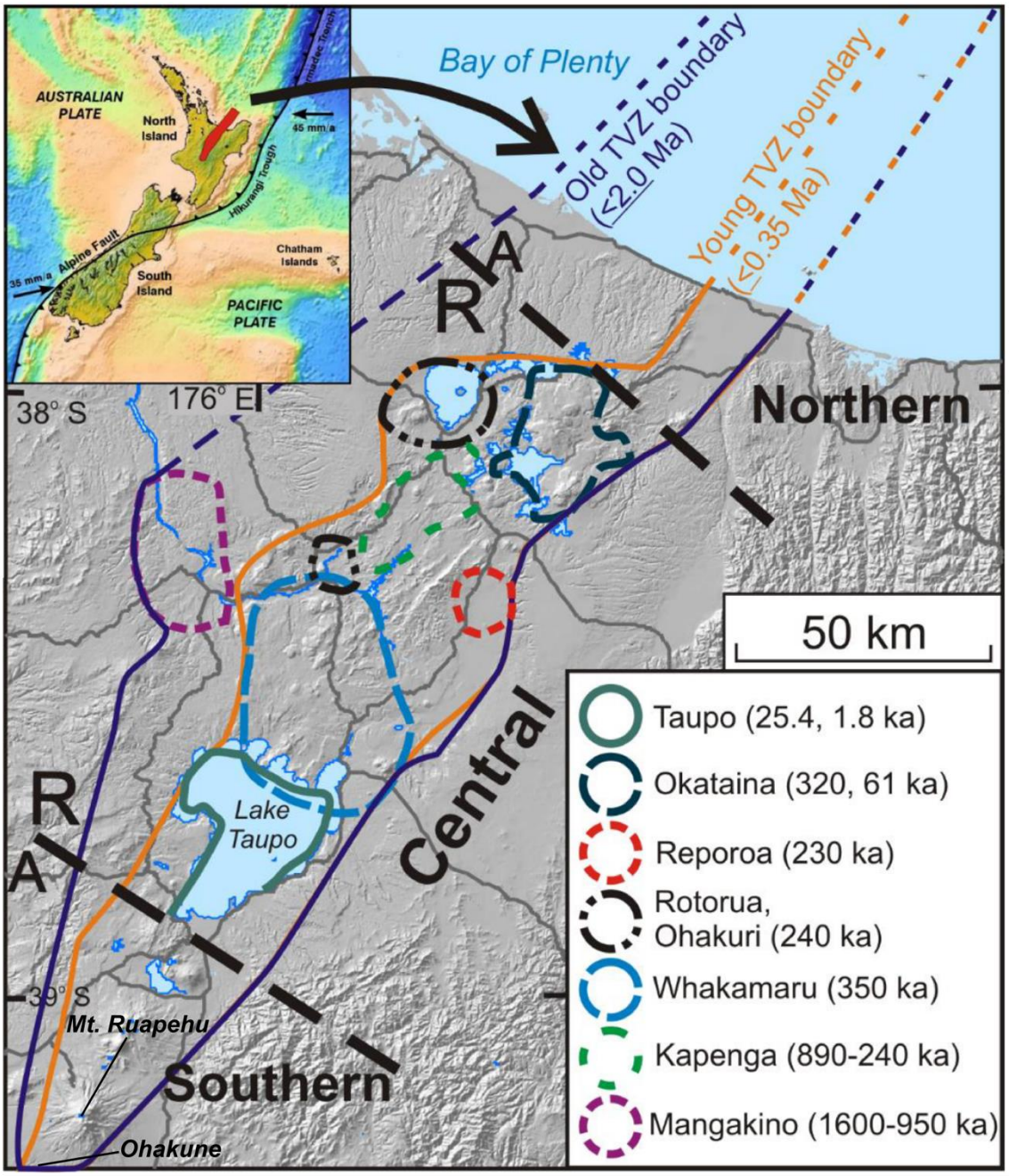

Figure 1. 6. Summary map of the Taupō Volcanic Zone (TVZ) and its compositional segmentation (A = andesite dominated; R = rhyolite dominated, central TVZ). The central TVZ is characterised by eight volcanic centres where large-scale rhyolitic volcanism has occurred; approximate ages of caldera forming eruptions from each centre are included. Boundaries defining the old and young TVZ enclose the vent sites and active caldera margins inferred to be active from 1.6 to 0.34 Ma and 0.34 Ma to present, respectively (Wilson et al., 1995). Modified from Wilson et al. (2009).

The TVZ is regionally segmented with regards to the composition of volcanic products (Figure 1.6). Although >90 % of the magma erupted in the region is rhyolitic, silicic magmatism is confined to a 125 x 60 km central segment characterised by large caldera-related rhyolitic centres (Wilson et al., 1995). To the north and south are 'normal' arc segments characterised by composite cones of andesite to dacite

composition, but with magma production rates roughly an order of magnitude less than in the central section (Wilson et al., 2009). This longitudinal segmentation of dominant magma type erupted in the TVZ reflects different magmatic plumbing systems, primarily due to variations in the thermal flux (Charlier et al., 2005; Price et al., 2005; Rowland et al., 2010).

The central TVZ has favourable conditions for formation and eruption of rhyolitic magma such as high heat flow, thin crust, active extension, high mantle-derived magma flux (Hochstein 1995; Houghton et al., 1995; Price et al., 2005; Wilson and Rowland, 2016). The fluxes of magma and heat transported by geothermal fluids are too low in both the northern and southern segments of the TVZ to allow the production of voluminous rhyolite magma (Bibby et al., 1995; Wilson et al., 1995, 2009; Price et al., 2005).

The central silicic region hosts eight Quaternary rhyolite volcanic centres, of which Taupō volcano is the most southern (Figure 1.6). Throughout the lifetime of rhyolitic volcanism in the TVZ (>1.8 Ma: Eastwood et al., 2013; Chambefort et al., 2014) at least 25 inferred caldera-forming eruptions have occurred in the central TVZ (Houghton et al., 1995; Wilson et al., 2009). Since 61 ka the central TVZ has erupted an estimated total of 782 km^3 of magma, with ~82 vol% represented by three rhyolitic caldera-forming eruptions from the two most productive individual rhyolite volcanoes in the world, Taupō and Okataina (Crisp 1984; Wilson, 1993; Wilson et al., 2009).

1.5.2 Magmatic compositional variations

Despite the central TVZ erupting predominantly rhyolite magma, the region has also erupted a compositional range of magmas from basalt through to dacite[1] (Figure 1.7: Graham et al., 1995). During the lifetime of the modern central TVZ (<61 ka), 68 distinct eruptions have been recognised: three rhyolitic caldera-forming events, 54 other rhyolitic, eight dacitic to rhyodacitic, and three basaltic (Wilson et al., 2009).

[1] Here I follow Ewart (1982) in the SiO_2 definitions for basalt, andesite, dacite, and rhyolite (at 53, 63, and 69% respectively).

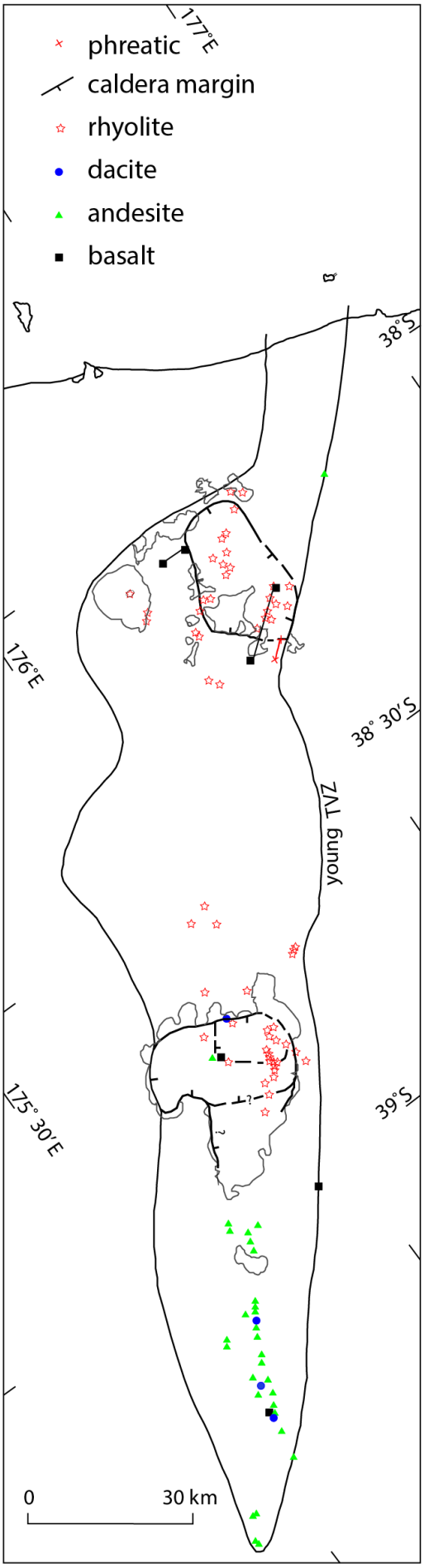

Figure 1. 7. Map showing known and inferred vent sites and calderas of the TVZ active in the past 65 ka (several eruptions have been omitted due to lack of information, see Wilson et al., 1995 for further detail). A compositional range from basalt to rhyolite is represented. Modified from Wilson et al. (1995).

All known surface basaltic activity in the TVZ is represented by relatively small, monogenetic events, with the largest individual event (Tarawera 1886 CE, c. 1 km^3) still at least an order of magnitude smaller than the largest andesitic and dacitic eruptions, and 2 to 3 orders of magnitude smaller than the largest rhyolitic eruptions (Wilson et al., 1995). However the fact that mafic compositions occur at the surface is unusual among rhyolitic systems. Typically, crustal density structure (especially below felsic magma systems) restrict basaltic magma to a stalled existence at the base of the crust (Hildreth 1981; Hildreth 2004; Hildreth and Wilson, 2007; Rowland et al., 2010).

Rhyolite makes up the overwhelming majority of erupted material in the central TVZ, and is produced mostly through pyroclastic eruptions, with lesser volumes of effusive dome-building events. The largest pyroclastic events are generally associated with ignimbrite formation and caldera collapse, and as such leave the greatest impact upon the geologic record (Wilson et al., 1995). However several of the rhyolitic centres within the TVZ display a wide range of eruptive volumes and styles, often coupled with intra-eruption time breaks and remarkably short time periods between events (Wilson, 1993, 2001; Nairn, 2002; Barker et al., 2016; Cooper et al., 2017). TVZ rhyolite eruptions span a considerable range in size (<0.01 km^3 to >1500 km^3) and are not distributed evenly through time; temporal variations in magma supply and tectonic rifting-related processes are thought to lead to clustering of events (Houghton et al., 1995; Gravley et al., 2007, 2016; Rowland et al., 2010; Allan et al., 2012).

1.5.3 Taupō volcanic zone crystal mush reservoirs

The presence of crystal mush zones beneath the TVZ has been inferred through multiple studies across a range of disciplines. Bibby et al. (1995) estimated the hydrothermal energy output of the central TVZ to be 4.2 GW, equivalent to four times the heat flow represented by the average rhyolitic magma eruption rate over the last 60 kyr. On the basis that this represents a steady-state situation, a significant reservoir of magma must therefore reside in the middle crust in order to continually supply the TVZ's highly active 23 geothermal systems with heat, volatiles, and chemicals (Bibby et al., 1995; Wilson and Rowland, 2016). Harrison and White (2004) produced a

seismogenic model that incorporated a zone of high Poisson's ratio 15 to 30 beneath the TVZ. This anomalous region was interpreted by the authors to represent a large reservoir of mafic material with associated partial melt that fractionates and assimilates crustal material before ascending into the upper crust. Further geophysical investigations suggest the presence of low shear velocities and high electrical conductivities at comparable depths (Heise et al., 2010; Behr et al., 2011).

Petrologic studies across the central TVZ (with a focus on Okataina and Taupō volcanic centres) have shown the presence of shallower silicic mush systems through crystal-specific investigations, with zircon model-age spectra and crystal textures providing the bulk of the evidence (Charlier et al., 2005; Wilson et al., 2006; Wilson and Charlier, 2009; Charlier and Wilson, 2010; Deering et al., 2011; Storm et al., 2011, 2012; Shane et al., 2012; Allan et al., 2013, 2017; Bégué et al.,2014; Barker et al., 2015; Graeter et al., 2015; Rubin et al., 2016).

Long-lived crystal mush reservoirs are the core of the complex magmatic networks that underlie the rhyolite-dominated calderas throughout the central TVZ (Figure 1.8). The mush zones beneath the active Taupō and Okataina calderas are thought to begin at depths as shallow as 4 km in places (Liu et al., 2006; Shane et al., 2008a), and in the case of Taupō, apparent pressures of amphibole crystallisation (using the calibration of Ridolfi et al., 2010) suggest the mush region extends down to at least 12 km depth (Allan et al., 2017). Prior geophysical studies extend the intermediate-silicic extent of the system down to approximately 16 km depth, with the mafic roots inferred to reach another ~15 km deeper (Harrison and White, 2004, 2006; Stratford and Stern, 2004, 2006).

The crystal-dominated mush zones of the Taupō and Okataina systems are inferred to be produced by the mixing and assimilation of mafic magmas with crustal material, along with significant levels of crystal fractionation (Charlier et al., 2005, 2008; Shane et al., 2008b; Wilson and Charlier, 2009; Deering et al., 2011; Allan et al., 2013, 2017; Cole et al., 2014; Barker et al., 2015). These mush reservoirs are inferred to be zoned with respect to composition, temperature, and crystallinity, which has been shown through various crystal-specific studies at Taupō (Allan et al., 2013, 2017; Barker et al.,

2015). The zonation of large silicic magma systems is often thought to translate to the melt-dominant body, inferred from the deposits of some large silicic eruptions that reflect an inversion of compositional zoning in the melt-dominant body (e.g. the Bishop Tuff: Hildreth and Wilson, 2007). However, examples of unzoned eruptive deposits produced by large silicic eruptions occur in the TVZ (e.g. Oruanui ignimbrite: Wilson, et al., 2006), suggesting that either zonation is not inherent to the development of melt-dominant magma bodies, or that the zonation can be destroyed by processes prior to or during eruption (Dunbar et al., 1989b; Charlier et al., 2005; Wilson et al., 2006; Allan et al., 2017).

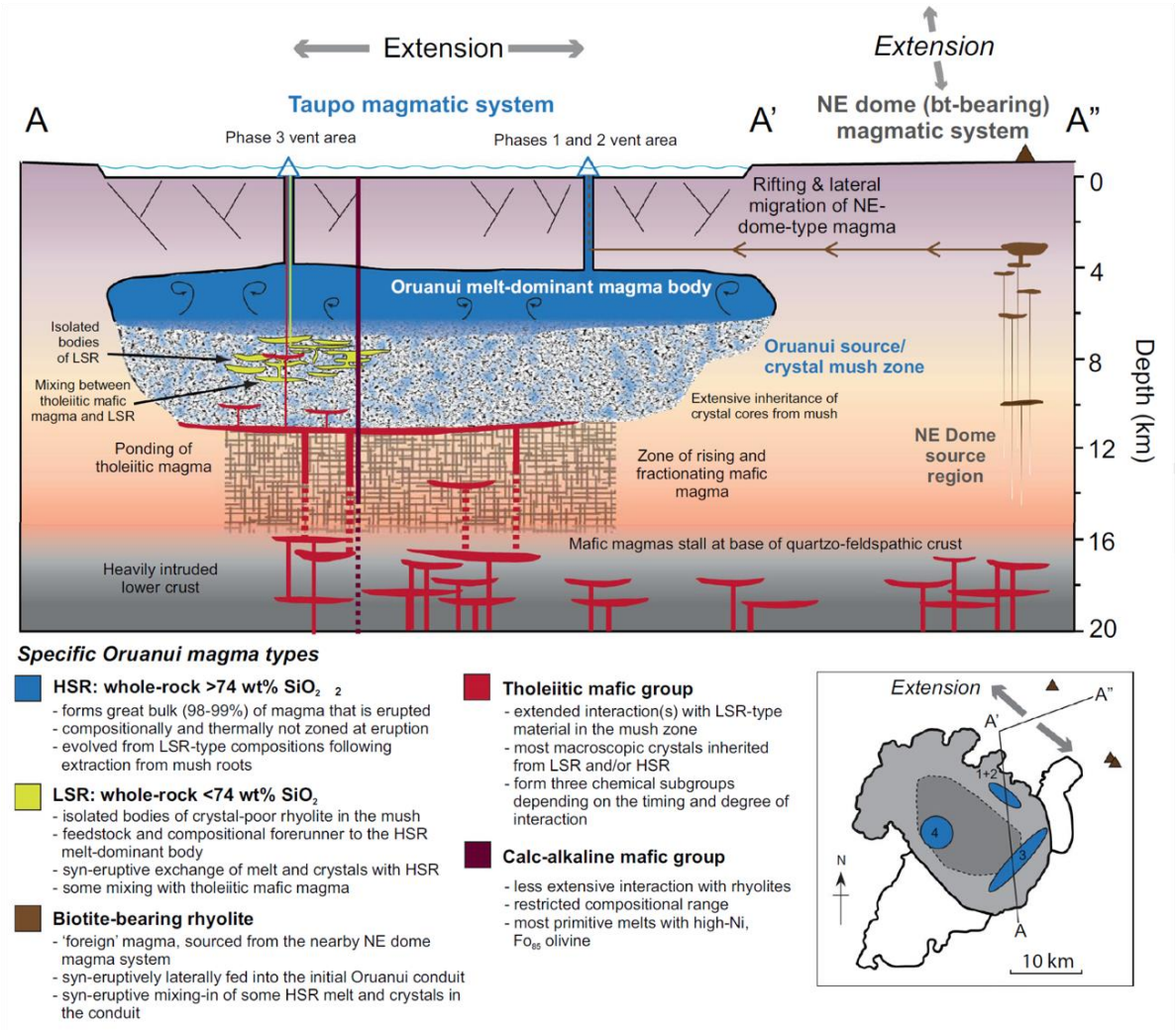

Figure 1. 8. Schematic scaled cross section displaying the magmatic system and mush zone beneath Taupō volcano, and the sources, depths, and pathways for the variety of magma components involved in the eruption. Sourced from Allan et al. (2017).

1.6 Taupō volcano

1.6.1 The Oruanui supereruption

The 25.4 ka Oruanui eruption of Taupō Volcano is the world's youngest supereruption, ejecting an estimated magma volume of 530 km^3 (Wilson, 2001). Producing 320 km^3 of pyroclastic density current deposits, 420 km^3 of primary intracaldera material, and 430 km^3 of fall deposits, it is the largest known phreatomagmatic eruption globally (Wilson, 2001). Rapid chilling, extensive fragmentation, extremely wide dispersal of fine grained fall deposits, and the creation of a large, non-welded ignimbrite suggest that there was extensive interaction with a proto Lake Taupō (Self and Sparks, 1978; Self, 1983; Wilson, 2001; Van Eaton et al., 2012; Van Eaton and Wilson, 2013). The magma erupted is characterised by moderate to high-silica rhyolite, with 3 to 13 wt% crystals. Greater than 99 vol% of the eruptive products are rhyolitic, with a mafic component comprising the remaining ~1 vol% (Wilson et al., 2006; Allan et al., 2017; Rooyakkers et al., 2018). The eruption has been divided into ten phases, with time gaps of hours to months separating some of them (Wilson, 2001).

During the Oruanui eruption both low- and high-silica rhyolite (LSR <74 wt% SiO_2< HSR respectively) magmas were erupted. LSR is inferred to represent tapping of interstitial magma direct from the upper regions of the mush zone during evacuation of the shallower melt-dominant body, which in turn is inferred to have formed through the accumulation of interstitial mush magma that evolved to produce the HSR (Figure 1.8: Wilson et al., 2006; Allan et al., 2013, 2017). The volumetrically dominant high silica magma (>98 vol%) contains a crystal cargo made up of plagioclase + quartz + orthopyroxene + hornblende + magnetite + ilmenite, with apatite and zircon as accessory minerals (Wilson et al., 2006; Allan et al., 2017). Two distinct juvenile mafic magmas are also present within Oruanui eruptive deposits; a tholeiitic group, and an olivine-bearing calc-alkaline group (Wilson et al., 2006). The olivine crystals in the calc-alkaline group host large melt inclusions which represent very primitive parental melt compositions of 46 to 51 wt% SiO_2 prior to interaction with the rhyolite magma system (Barker et al., manuscript in prep).

A study on the Oruanui eruptive deposits sampled pumice clasts from each of the eruption phases (after Wilson, 2001), and concluded that the magma was likely held in a homogeneous, actively convecting magma body immediately prior to evacuation (Wilson et al., 2006). The authors reported that although there are notable variations in composition, temperature, and crystallinity of the erupted rhyolite, these changes do not occur systematically with stratigraphic height (i.e. the magma body was thoroughly mixed: Figure 1.9).

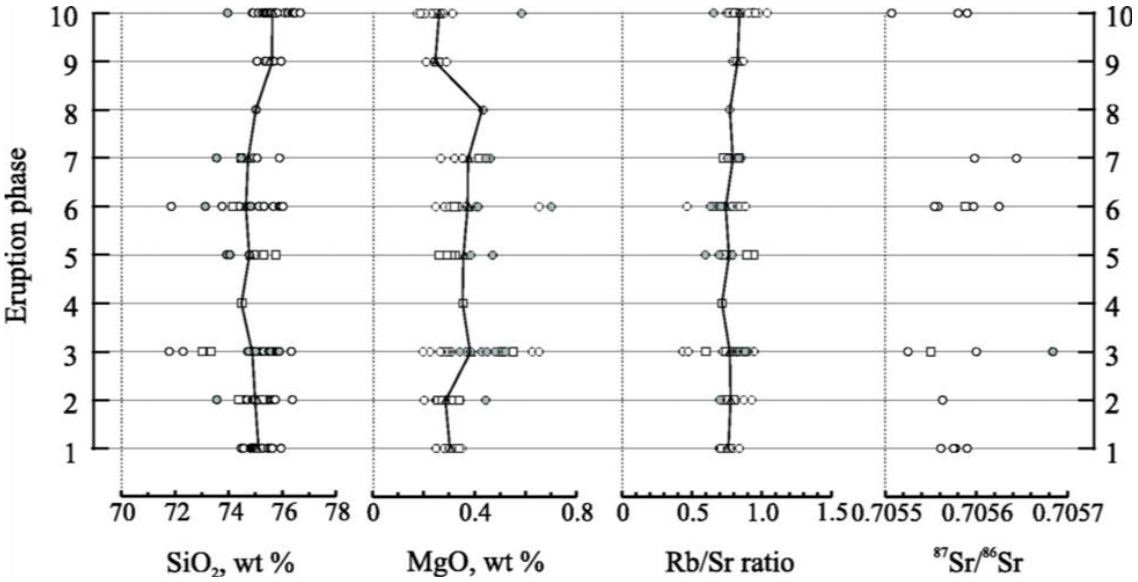

Figure 1. 9. Selected analytical data versus stratigraphic height for single (open circles) and multiple (open squares) rhyolite clasts from Oruanui deposits. Filled circles/squares represent high-Mg clasts, and filled triangles (connected by lines) display the mean of each set of analyses at each eruption phase. Sourced from Wilson et al. (2006).

In an effort to explain the lack of chemical zoning within the magma body, Wilson et al. (2006) invoked direct mafic injection to the base of the shallow magma body to provide the necessary energy to convectively stir and homogenise the melt. However the authors did comment on geochemical evidence which suggested that vigorous rhyolite convection must have occurred prior to mafic injection (Liu et al., 2006; Wilson and Charlier, 2009). Subsequent petrologic research has revealed that the majority of interaction between the mafic magma and the more evolved magma occurred in a medium-yield strength transition zone between the crystal-dominated mush and melt-dominated body, where the mafic magma could disaggregate into a range of different sized blebs (Figure 1.10: Allan et al., 2013, 2017; Rooyakkers et al., 2018). The mafic magmas may have added some energy directly to the melt-dominant rhyolite magma

body, but wholesale convective mixing was already well established when the magmas were mingled.

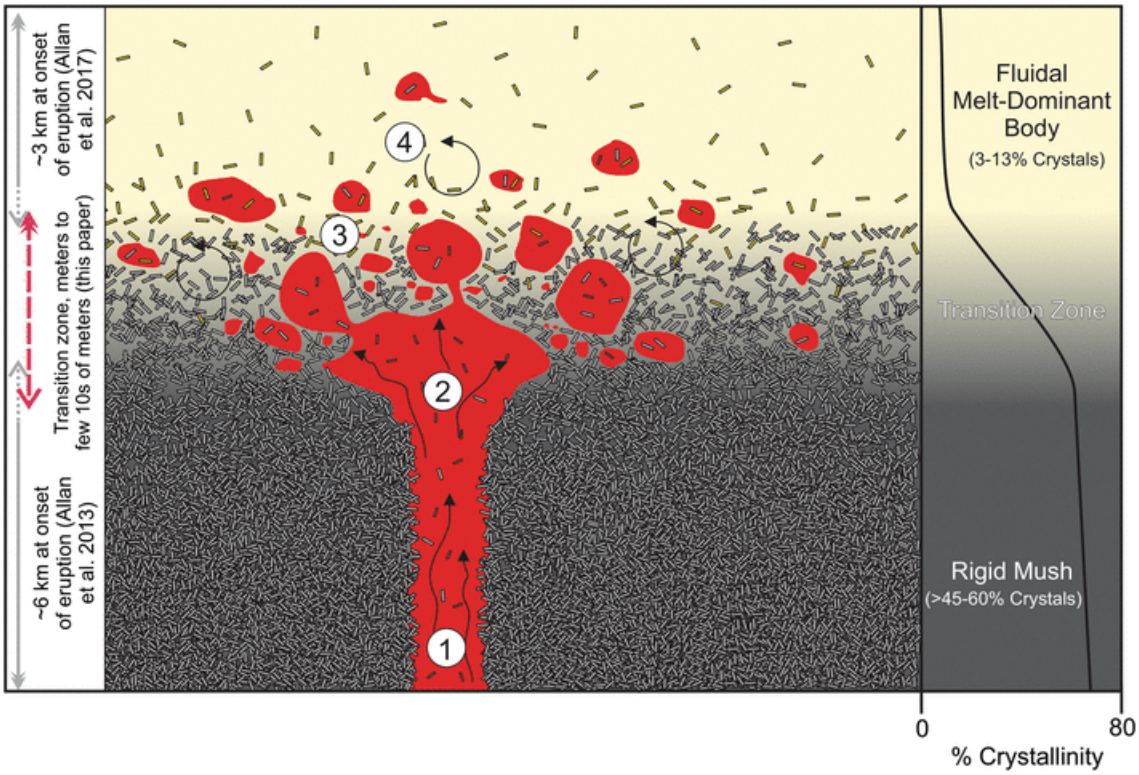

Figure 1. 10. Schematic figure illustrating the nature of mafic and felsic interaction during assembly of the Oruanui magma body. 1) Mafic magma ascends through the rigid mush via diking-related processes. 2) The yield-strength drops rapidly with decreasing crystallinity as the mush transitions into rhyolite magma, and mechanical break-up of the injecting mafic magma occurs. 3) Varying sizes of mafic blebs quench/crystallise rapidly upon injection into the cooler rhyolite magma. 4) Vigorous convection circulates the mafic blebs throughout the magma chamber. Sourced from Rooyakkers et al. (2018).

The exceptional thermal output of the central TVZ leads to the inference that there are large volumes of mafic magma continually supplying heat to the overlying silicic systems and geothermal systems, even in areas lacking recent volcanism. An estimate of the rate of mafic magma required to provide the geothermal heat flux around Taupō has been suggested at 0.32 m^3/s (Bibby et al., 1995; Charlier et al., 2005). However, the rate of mafic magma needed to produce the amount of rhyolite erupted from Taupō volcano over the past 65 kyr is thought to be closer to 1 m^3/s (Charlier et al., 2005). Although the parental mafic magma flux into the silicic system is likely to vary through time, periods of elevated mafic magma supply below Taupō volcano can lead to remobilisation of the crystal mush region, and the production of interstitial silicic melt (Barker et al., 2016). If tectonic processes allow, eruptible magma can be

withdrawn and accumulated from the remobilised mush in timescales on the order of centuries (Allan et al., 2013, 2017). The Oruanui melt-dominant body was assembled on rapid timescales (inferred magma accumulation rates exceeding 1 km^3 yr^{-1}; Allan et al., 2017) when compared with a similar-sized rhyolite eruption such as the Bishop Tuff (~4 km^3 kyr^{-1}: Hildreth and Wilson, 2007), leading to strong mixing within the Oruanui melt-dominant magma body. Plagioclase and orthopyroxene crystals from Oruanui pumices record significant cooling and crystallisation within parental melt-dominant body during its lifetime: their rims show decreases in respective anorthite and enstatite levels, indicative of an evolving host melt composition (Allan et al., 2017). Calculated as equivalent to a temperature drop of 40-50 °C, such a high rate of heat loss is inferred to have been the dominant reason for mixing and turbulence within the melt-dominant body (destroying any prior thermal and compositional zonation within the body). Thus the subsequent homogenisation was likely an inherent feature of the Oruanui melt assembly, and not entirely controlled by an external factor (e.g. mafic recharge).

1.6.1.1 Inherited cores

Studies of orthopyroxene and plagioclase crystal populations from Oruanui rhyolite by Allan et al. (2013, 2017), following earlier work by Charlier et al. (2008), led to the proposal of a significant decompression event that affected the majority of crystals during accumulation of the shallow melt-dominant magma body from HSR magma compositions. The cores/interiors of 90 % of orthopyroxene crystals display textural features indicative of disequilibrium: partial dissolution and occasional resorption of the crystal interiors, followed by crystallisation of new rims at shallower crustal levels (Figure 1.11). Disequilibrium textures (e.g. notable resorption and sieve textures) were also observed in 90 % of plagioclase interiors with subsequent growth rims, which suggests a similar dissolution – re-growth history (Charlier et al., 2008; Allan et al., 2017). Allan et al. (2017) proposed that the orthopyroxene and plagioclase crystals experienced the same decompression event, and inferred that they shared a common magmatic history. The model pressures of accompanying amphibole crystallisation (using the calibration of Ridolfi et al., 2010) placed the crystal cores at pressures

between 140 to 270 MPa, and the re-growth rims at pressures between 90 to 120 MPa (Allan et al., 2013; 2017). These pressure estimates correlate with orthopyroxene enstatite and Al contents, where higher enstatite contents are inferred to represent orthopyroxene growth from hotter, less evolved melts, and Al contents are inferred to increase with pressure (depth) in the magmatic system (Allan et al., 2017). The outermost orthopyroxene rim compositions exhibit a tight clustering at ~46 mol% enstatite and ~2000 ppm Al, whereas the cores exhibit a positive relationship between enstatite and Al contents which range from ~46 to ~64 mol% and ~1000 to ~9000 ppm, respectively (Figure 1.12). Thus the crystal cores are inferred to have grown in the magmatic mush zone at greater depths than the re-growth rims, which crystallised in the shallower, melt-dominant magma body.

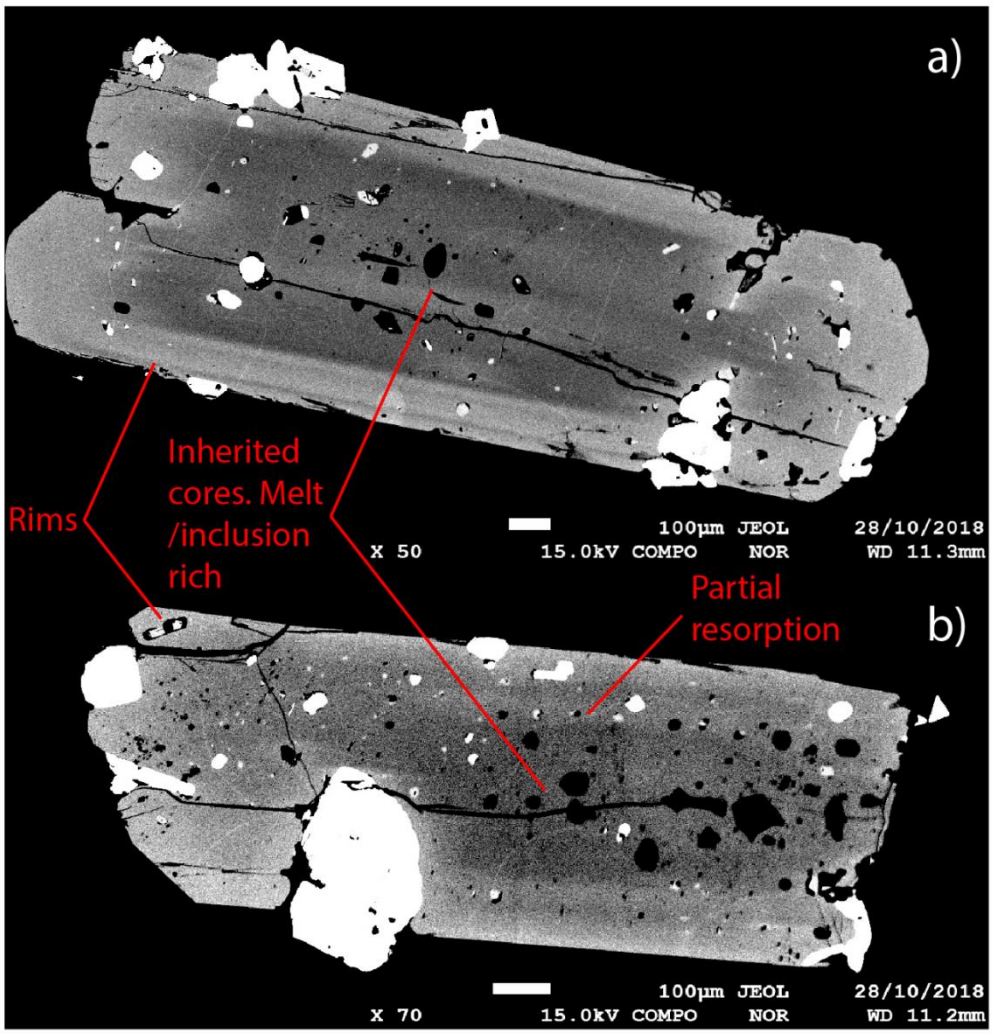

Figure 1. 11. Examples of zonation in the inherited cores of orthopyroxene, rich in melt and mineral inclusions, in samples **a)** P2367 and **b)** P2374, the details of which are in Table 2.1.

The range of model crystallisation pressures from amphibole cores suggests that batches of melt plus crystals were tapped from a range of differing pressures throughout the crystal mush zone during accumulation of the shallow magma body (Allan et al., 2017). However in the decades to centuries prior to eruption energetic convection of the melt-dominant body homogenised the melt-dominant magma body (Allan et al., 2017). Thus the crystal core compositions in any Oruanui pumice clast have the potential to cover the whole compositional range published for that respective mineral, no matter which eruptive phase or vent location the clast came from (Figure 1.13: Allan et al., 2017). The apatite and melt inclusions hosted within the cores of orthopyroxene crystals of the Oruanui eruptives should exhibit a range of compositions, reflecting melt compositions with which they last equilibrated from various levels within the magmatic system with which they last equilibrated. Analysis of melt and apatite inclusions hosted in the inherited orthopyroxene cores may thus provide insights into volatile behaviours throughout the crystal mush zone. Further comparison of this range in mush zone-sourced compositions with the more evolved groundmass glass and microphenocryst apatite crystals from the shallow magma body may in turn allow the establishment of a magmatic volatile pathway from the base of the mush zone up through and into the immediately pre-eruptive conditions of the melt-dominant magma body.

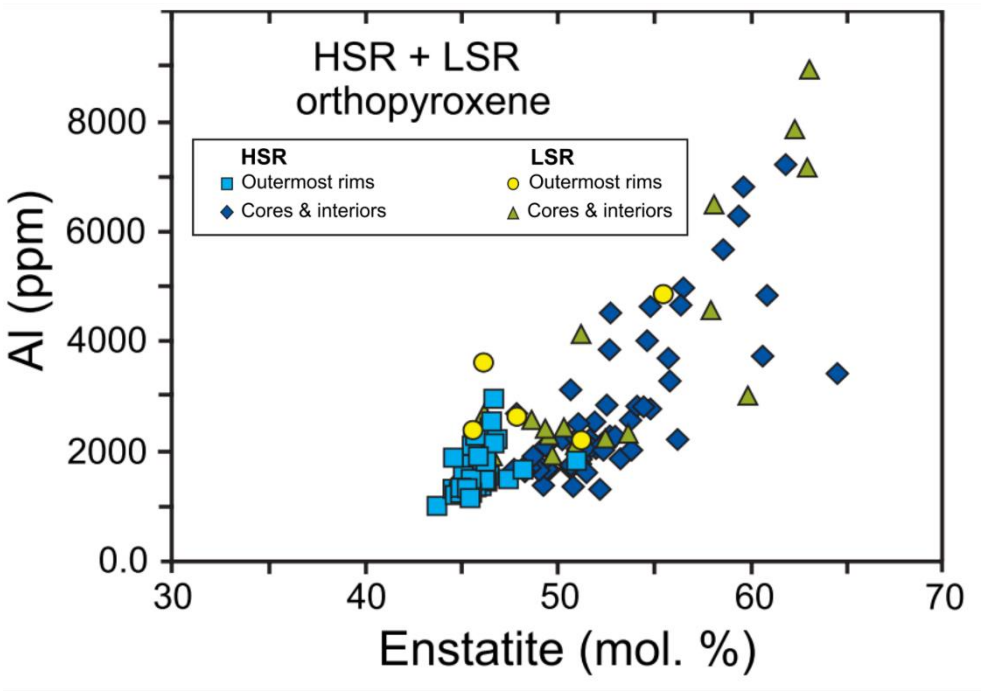

Figure 1. 12. Enstatite (mol%) versus Al (ppm) for the outermost rims and cores/interiors for orthopyroxene from high-silica rhyolite (HSR) and low-silica rhyolite (LSR) pumice clasts. Modified from Allan et al. (2017).

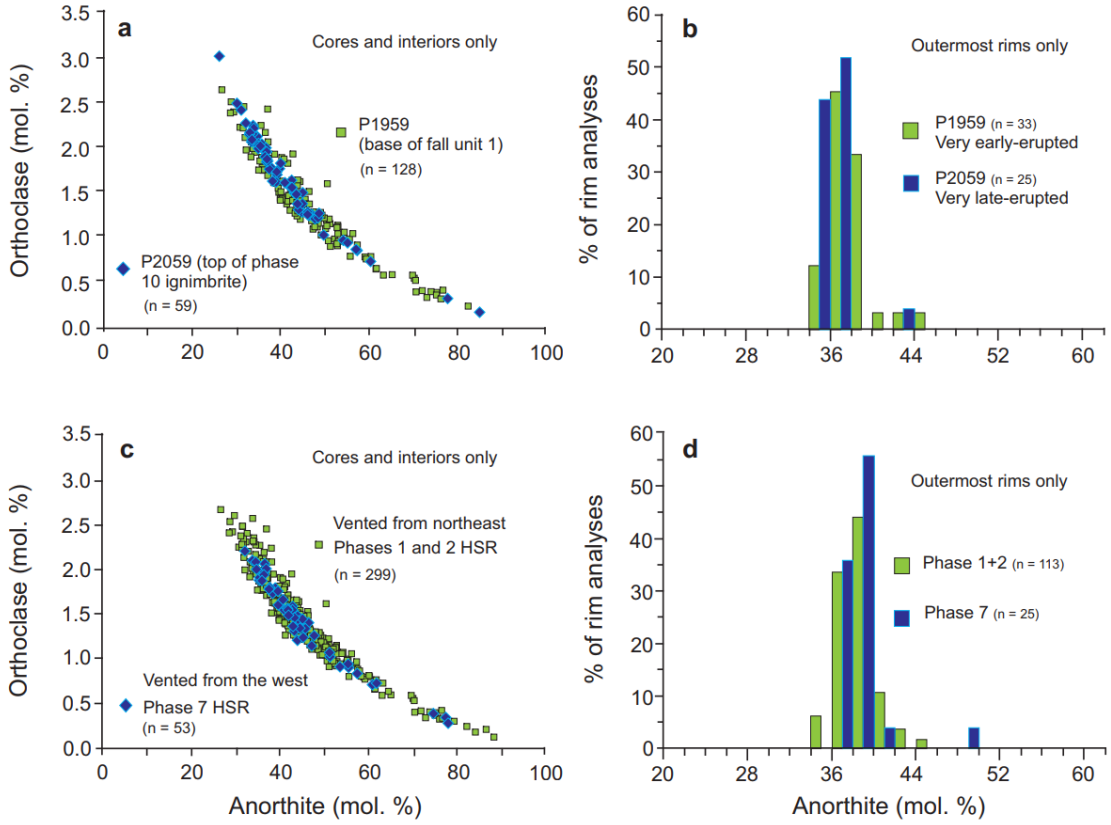

Figure 1. 13. Comparisons of high-silica rhyolite (HSR) plagioclase compositions between early- versus late-erupted clasts in **a** and **b**, and between clasts erupted from inferred geographically separate vent locations in **c** and **d**. Graphs **b** and **d** show data for the outermost crystal rims only. Sourced from Allan et al. (2017).

1.7 Post-Oruanui eruptions

Geochemical studies of the post-Oruanui eruptive units demonstrate that a significant reorganisation of the magmatic system beneath Taupō Volcano occurred following the Oruanui supereruption (Sutton et al., 2000; Charlier et al., 2010; Gelman et al., 2013; Barker et al., 2014, 2015). A new silicic system formed after collapse of the caldera, with intense modification of the magmatic root zone through the influx of hot mafic magmas (Barker et al., 2015). Five thousand years after the Oruanui event, Taupō produced 3 small dacitic units over the space of 3 ka (labelled Ψ, Ω, and A: Wilson, 1993; Barker et al., 2015). From about 12 ka onwards, Taupō erupted the first of 25 rhyolitic units (labelled B → Z), which have been grouped into three geochemically-related subgroups: SG1, SG2, SG3 (Figure 1.14b: Sutton et al., 1995, 2000; Barker et al.,

2015). Vent locations for all four post-Oruanui subgroups overlap with the inferred Oruanui structural caldera (Figure 1.14a).

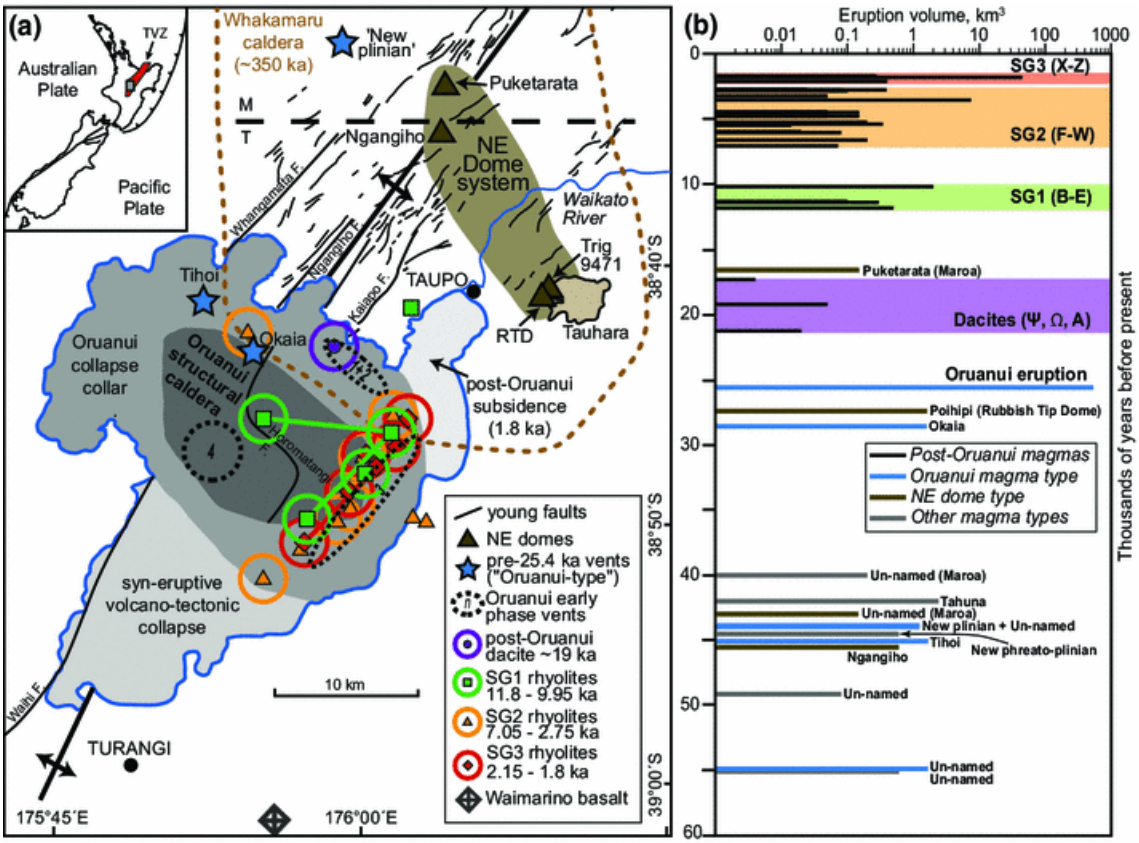

Figure 1. 14. An overview of Taupō caldera and the surrounding structural features, with inferred vent sites for the post-Oruanui eruptions added (circles represent implied uncertainty of vent locations). **b)** Eruption volume for eruptions from the Taupō-Maroa area over the past 60 thousand years. Eruption volumes represent the dense rock equivalent. Sourced from Barker et al. (2015).

The dacite units Ψ and Ω, the rhyolite units C, S, and subunit Y6 (i.e., one example from each subgroup) were re-analysed for this study. Despite wholesale reorganisation of the magma system after the Oruanui eruption the fundamental processes governing volatile transport in principle should not change. Barker et al. (2015) showed that crystals in the early dacites commonly displayed heavily resorbed interiors with mottled cores overgrown by normally zoned rims. The high enstatite and Al compositions of the orthopyroxene cores (~En_{47} to En_{65}, 1000-7000 ppm Al) relative to the rims (~En_{44} to En_{48}, Al 1000 to 3000 ppm) are taken as indicative of an origin deeper within the mush system at higher temperatures (Allan et al., 2017). The later rhyolites also display compositional zoning in the orthopyroxene, albeit less pronounced and to a lesser extent (Barker et al., 2015). Orthopyroxenes from Unit C are often normally zoned, but not as prominently as the dacite units. Orthopyroxenes

from Unit S can display minor normal zoning, but to an even lesser extent than that for Unit C. Subunit Y6 orthopyroxenes typically display reverse zoning, with very few normally zoned crystals. In addition to melt inclusions and apatite, small sulfide inclusions have been documented within the post-Oruanui dacite units. Suspected to be pyrrhotite, these sulfide inclusions were also targeted for EPMA analysis in this study to confirm their composition.

1.8 Previous TVZ volatile analyses

All attempts to measure sulfur in quartz- or plagioclase-hosted melt inclusions by electron microprobe analysis (EPMA) in Taupō volcano rhyolites (as well as early studies analysing orthopyroxene melt inclusions via ion microprobe) have returned values below detection limits (Dunbar et al., 1989a; Dunbar and Kyle, 1993; Bégué et al 2015a, 2015b). Low sulfur is not exclusive to Taupō volcano rhyolites: quartz-(±plagioclase-) hosted melt inclusion data from rhyolite magmas across the central TVZ all return statistically insignificant values (Johnson et al., 2011; Bégué et al., 2015a, 2015b). However none of these studies specifically targeted inclusions hosted in the inherited cores.

Past studies of Cl and F abundances in quartz- and plagioclase-hosted melt inclusions from Taupō volcano have produced values above detection limits, albeit with scatter. Generally Cl and F plot between 0.2 to 0.3 wt% and 200 to 600 ppm respectively at SiO_2 levels between 77 to 79 wt%, when the analysis is calculated volatile-free and normalised to 100 % (Dunbar et al., 1989a; Hervig et al., 1989; Dunbar and Kyle, 1993; Bégué et al; 2015a, 2015b, 2017). In addition, several studies have suggested that there are two suites of rhyolitic melt produced in the TVZ (Deering et al., 2008, 2010), which can be differentiated by their halogen compositions (Figure 1.15: Bégué et al., 2015b).

The behaviour of both H_2O and CO_2 have been well documented in the upper, quartz-saturated region of TVZ magma systems for both pre- and syn-eruptive processes (Liu et al., 2006; Johnson et al., 2011; Bégué et al., 2015b; Myers et al., 2018, 2019). In

addition, plagioclase-hosted melt inclusions were analysed in the post-Oruanui eruptive units, but were inferred to have leaked during decompression and thus represent minimum volatile contents (Barker et al., 2015). Significantly, it is inferred that Oruanui and Okataina Volcanic Centre melts were saturated with a H_2O-dominated vapour phase during quartz-crystallisation (Liu et al., 2006; Johnson et al., 2011). This conclusion was reinforced through the relationship between CO_2 and Sr contents of Oruanui melt inclusions, in which CO_2 broadly decreases with decreasing Sr (Wilson et al., 2012).

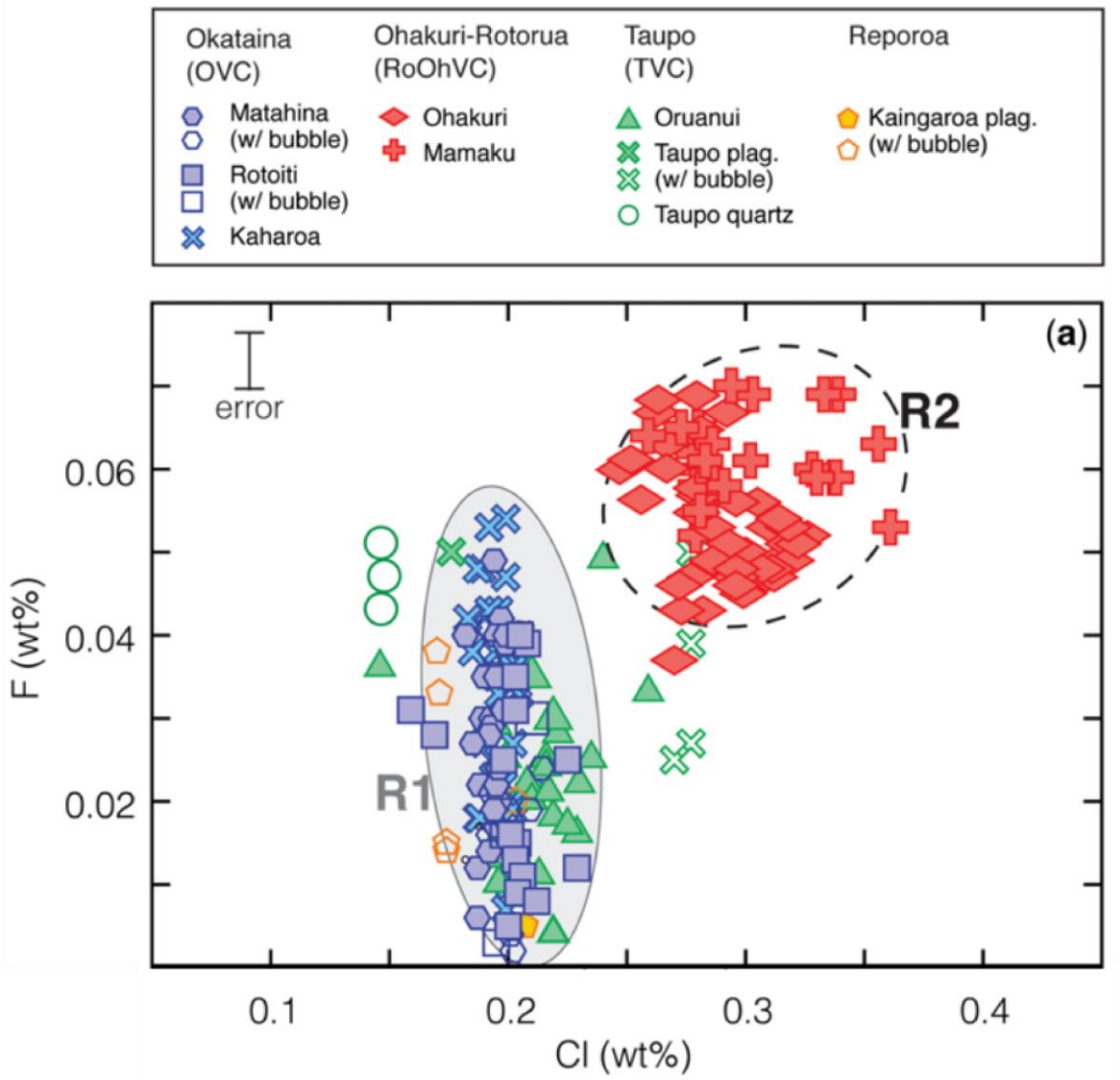

Figure 1. 15. Fluorine (wt%) versus chlorine (wt%) of quartz- and plagioclase-hosted melt inclusions for a selection of TVZ rhyolite eruptives. Modified from Bégué et al. (2015b).

In addition to these studies directly analysing the volatile contents of TVZ melt inclusions, Charlier et al. (2012) were able to infer syn-eruptive volatile processes in the Oruanui eruption through diffusion gradients of lithium in feldspar and quartz. The authors concluded that the ~50 % increase in the lithium concentrations of the crystal rims relative to the cores was due to a change in partitioning behaviour controlled by the unmixing of an aqueous vapour phase into low-density vapour and high-density liquid phases at 22 MPa.

At the time of writing no studies investigating the volatile contents of either crystal-hosted inclusion or microphenocryst apatites of the TVZ have been published.

1.9 Melt volatile evolution

In this section I consider the controls on the behaviour of the three studied elements, sulfur, chlorine, and fluorine, within silicate melts. The terms sulfur-, chlorine-, and fluorine-solubility are used to describe the summed solubilities of each of the dominant respective volatile species in the melt. At melt concentrations below their respective solubilities in a hydrous silicate melt, volatile components will partition between the melt phase ± aqueous fluid phase ± mineral phase(s), at ratios that can be calculated and expressed as individual partitioning coefficients (e.g. $D_X^{fluid/melt}=Y$, where *X* is the volatile component, and *Y* is the coefficient that represents partitioning between fluid and melt). Further, if a volatile component reaches its maximum solubility and saturates within a melt, a volatile-rich fluid phase may directly exsolve (Webster, 2004). The type, composition, and number of fluid phases present within a magmatic system can change throughout the evolution and depressurisation of a given magma composition. Under magmatic conditions, fluid phases are typically one of the following: a H_2O-dominated aqueous vapour phase; an electrolyte-bearing, H_2O-bearing hypersaline liquid (e.g. brine), variably enriched in dissolved solids (Si^{4+}, Al^{3+}, Na^+, K^+, Ca^{2+}, $Fe^{2,3+}$, Mg^{2+}, metals, SO_4^{2-},Cl^-, HS^-); or a non-volatile molten sulfide (e.g. pyrrhotite: Webster and Botcharnikov, 2011). In addition to these possible fluid phases, several minerals common to magmatic systems can exert a control over the volatile contents of the melt. Apatite and amphibole are two such phases, but they are

expected to have more of an effect on fluorine over sulfur and chlorine, due to the relative preference of F to remain in the melt and mineral phases.

In the case study here, Taupō is a hydrous magmatic system, with estimated water contents of ~3 wt% for the primitive basaltic melts that feed the system (Simon Barker, pers. comm, 2019), and 4.5 to 6.5 wt% for Oruanui and post-Oruanui dacitic-rhyolitic magmas (Liu et al., 2006; Allan et al., 2013; Barker et al., 2015; Myers et al., 2019). These studies have inferred that an aqueous vapour phase typically exsolves in Taupō silicic magmas, and thus will exert a significant control over melt volatile abundances at some stage in the evolution of these magmas. The point along the evolutionary pathways that this fluid phase starts exsolving within the Taupō system is not well constrained, but analysing the volatile contents of the deepest inherited orthopyroxene cores may provide some insight. It is also possible that volatile-dominated fluid phases contribute to the volatile pathway below Taupō volcano. Pyrrhotite is hosted as inclusions in orthopyroxene cores of the post-Oruanui dacite units (Gelman et al., 2013; Barker et al., 2015), and it is possible a sulfur-rich phase (e.g. anhydrite or sulfide melt) was saturated prior to pyrrhotite crystallisation. Melt inclusion-focused studies of subduction zone silicic systems have proposed that the onset of magnetite crystallisation may lead to thoroughly depleted sulfur values, through a rapid decrease in the fO_2 (i.e. the magnetite crisis: Sun et al., 2004; Jenner et al., 2010). The exsolution of a Cl-rich hypersaline brine has also been suggested to occur in the system below the Rotorua and Ohakuri calderas (Bégué et al., 2017). The exsolution of these volatile-rich fluid phases would heavily fractionate the volatile contents of the melt (Carroll and Rutherford, 1985, 1987; Luhr, 1990; Clemente et al., 2004; Webster, 2004; Jugo et al., 2005a; Jugo 2009; Jenner et al., 2010). The use of relevant fluid-melt partitioning models (e.g. sulfur: Scaillet et al., 1998; Keppler, 2010; Binder et al., 2018: chlorine: Kravchuk and Keppler, 1994; Signorelli and Carroll, 2000; Webster et al., 2009; Doherty et al., 2014: fluorine: Webster, 1990; Webster and Holloway, 1990) may allow estimates of the concentrations of S, Cl, and F present in any exsolving fluid phases, and increase our understanding of volatile transport within the magmatic system below Taupō volcano.

In addition to fluid phases, eruptive deposits from Taupō volcano also contain mineral phases that can accommodate S, Cl, and F. Apatite is ubiquitous throughout Taupō volcano deposits, albeit in trace amounts, and amphibole is present in the Oruanui and some post-Oruanui eruptive deposits (Wilson et al. 2006; Barker et al., 2015). The ubiquity of apatite in magmatic systems and its ability to incorporate weight percent amounts of Cl and F (and trace amounts of S) make it especially useful in partitioning coefficient models (e.g. Candela, 1986; Piccoli and Candela, 2002; Parat and Holtz, 2004; Mathez and Webster, 2005; Webster et al., 2009, 2017; Doherty et al., 2014; Scott et al., 2015; Stock et al., 2018). The volatile, major, or trace element contents of apatite from Taupō volcano or elsewhere in the TVZ have yet to be investigated. Many studies report on its occurrence as an accessory mineral throughout the TVZ, hosted within a range of rock compositions from andesite to rhyolite (e.g. Patterson and Graham, 1988; Beresford et al., 2000; Sutton et al., 2000; Price et al., 2005; Liu et al., 2006; Wilson et al., 2006; Barker et al., 2015). The potential of apatite as a geochemical tracer is well established (e.g. Ayers and Watson, 1993; Piccoli and Candela, 1994, 2002; Sha and Chappell, 1999; Belousova et al., 2001, 2002), but has yet to be explored in a TVZ context. Data from EPMA analysis were considered reliable, until Stormer et al. (1993) documented that crystal orientation drastically affected X-ray counts for F (and to a lesser extent, Cl) analyses. However recent studies have presented improved analytical techniques that allow for dependable analysis of apatite by EPMA (Goldoff et al., 2012; Stock et al., 2015; Zhang et al., 2016).

1.9.1 Excess sulfur in silicic eruptive events

Eruptions of large silicic magma systems tend to epitomise a phenomenon known as the excess sulfur problem, in which considerably more sulfur is ejected into the atmosphere during an eruptive event than the amount estimated through petrologic investigations (e.g. Mount Pinatubo: Westrich and Gerlach, 1992). Possible explanations for the sulfur deficiency in petrologic estimates of silicic eruptions include sulfur released through the breakdown of sulfur rich phases, sulfur degassing from non-erupted magma, and the presence of a sulfur-rich fluid phase that exsolved from the magma at depth (Scaillet et al., 1998, and references therein). Additionally, large

caldera-forming silicic eruptions may release the sulfur sequestered in a hydrothermal envelope around the magma body. Although no record of the sulfur released from the Oruanui eruption has been observed, the 232 CE Taupō eruption (Hogg et al., 2012) has been identified in ice core records from both hemispheres (Sigl et al., 2013). However, when the 232 Taupō eruption is compared with the 40 largest eruptions of the past 2.5 kyr (of which the it is the second largest in terms of magma volume at ~35 km3: Barker et al., 2015), the amount of sulfur released is only slightly above average (Sigl et al., 2015). If the previously published below detection limit analyses of sulfur in quartz- and plagioclase-hosted melt inclusions from Taupō volcano are representative of the magma at depth, then sources of sulfur other than that contained in the melt have to be considered to produce the minor, but identifiable ice core sulfur peaks. The four most likely sources of sulfur that could potentially be released during a silicic caldera-forming event such as the 232 CE Taupō eruption are: (1) a fluid phase coexisting at depth with the magma prior to eruption; (2) the breakdown of sulfur-rich crystalline phases (e.g. pyrrhotite or anhydrite); (3) sulfur sequestered in a hydrothermal envelope surrounding the magma body; and (4) the intrusion of relatively sulfur-rich mafic magmas. Knowledge on the surficial flux of sulfur near volcanic centres may help to identify the influence of each of these suggested potential sources, but sulfur emissions are poorly constrained in the central TVZ. However, one estimate for the H_2S flux at the Rotokawa geothermal system just north-east of Taupō caldera has been estimated at ~50 tonnes/day (Bloomberg et al., 2014). Although this may be indicative of a magmatic source supplying sulfur to the system, the value is estimated from CO_2 data and has yet to be supported with direct measurements. Without reliable data on the rates of surficial sulfur degassing, it is hard to constrain the total flux throughout Taupō magmatic system. To this end, recording the sulfur content of melt inclusions originating from deep within the magma system may provide insight into the most likely source of sulfur associated with the Taupō magma system.

2. Methodology

2.1 Samples studied

Three low-silica rhyolite (LSR) and seven high-silica rhyolite (HSR) clasts from the ignimbrite deposited during phase ten of the Oruanui eruption (Wilson, 2001) were sampled for this study. The clasts were sampled from multiple localities (Table 2.1). Five post-Oruanui units were also analysed; two dacite and three rhyolite (Table 2.1). These units were sampled and crystal mounts prepared by Barker et al. (2015), but were re-analysed here with a focus on S, Cl, and F. In addition to the silicic clasts, basaltic-andesite olivines with abundant melt inclusions already prepared and analysed by EPMA and LA-ICP-MS by Barker et al. (manuscript in prep) were re-analysed by EPMA for sulfur, chlorine, and fluorine to compare with the dacites and rhyolites. These olivines originate from juvenile mafic enclaves collected from both the Oruanui and Waimahia (Unit S) eruptions, which are primarily andesitic composition (Figure 2.1). However the most primitive olivine crystals of these enclaves are inferred to host melt inclusions that represent the primitive mantle melt compositions that feed the silicic system. Analysing the volatile abundances of these primitive melts will provide end-member compositions to the complete magmatic volatile pathway that this thesis is aiming to infer.

2.2 Sample preparation

The porous nature of pumice facilitates water percolation after deposition. All pyroclasts sampled in this study were secondarily hydrated, but had clear glass and no traces of secondary hydrothermal alteration, leaching, or enrichment. However, several precautionary steps were taken in the sample preparation process in order to minimise contamination. Clast outer rims were trimmed with a diamond blade Bianco saw and discarded, removing any adhering organic material. The fresh inner cores of the samples were cut into rectangular billets with the approximate dimensions of 12 x 6 x 3 cm as an appropriate size for jaw crushing. The billets were then cleaned in

reverse osmosis water in an ultrasonic bath for at least 40 minutes to remove as much remnant foreign material as possible. The billets were then dried completely in a fan-forced oven at >80°C for at least 72 hours.

Table 2. 1. Summary and location of the samples prepared in this study, and by Barker et al. (2015) and Barker et al. (manuscript in prep).

Sample	Age (ka)	Volume (km^3)	Classification	Locality	GPS	
Oruanui					*NZMS*	
P1453	25.4	>1100	high-silica rhyolite	2730	2750400 E	6305300 N
P1592			high-silica rhyolite	2442	2781100 E	6278300 N
P2361			low-silica rhyolite	448	2769835 E	6245318 N
P2362			low-silica rhyolite	448	2769835 E	6245318 N
P2366			high-silica rhyolite	1533	2774116 E	6245306 N
P2367			high-silica rhyolite	1533	2774116 E	6245306 N
P2368			low-silica rhyolite	1511	2774873 E	6244781 N
P2369			high-silica rhyolite	1511	2774873 E	6244781 N
P2370			high-silica rhyolite	1511	2774873 E	6244781 N
P2374			high-silica rhyolite	1520	2775749 E	6245952 N
P560			basaltic-andesite	1514	2773623 E	6278510 N
P950			basaltic-andesite	2165	2773623 E	6278510 N
P2224	25.4	>1100	basaltic-andesite	unkown	2773623 E	6278510 N
Post-Oruanui					*NZTM*	
P2163	20.5	0.05	ψ dacite	914	2770364 E	6274100 N
P2112	18.8	0.1	Ω dacite	2358	2770779 E	6274112 N
P2142	11.4	0.75	C SG1 rhyolite	2425	2776683 E	6253370 N
P2201	3.6	16.9	S SG2 rhyolite	3066	2782880 E	6259551 N
P2288	1.8	1.5	Y6 SG3 rhyolite	2554	unknown	

Localities refer to the site for the deposits where each sample was found after Wilson (2001).
SG1/2/3 refer to post-Oruanui rhyolite subgroups after Barker et al. (2015).

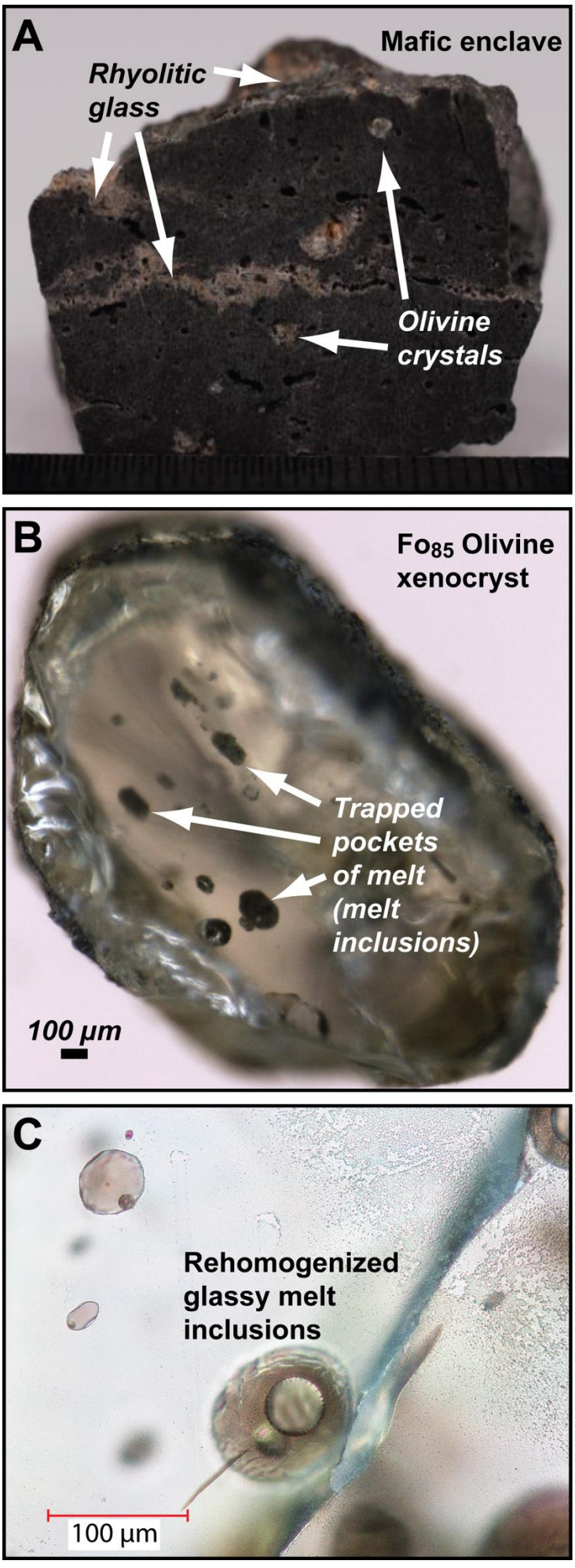

Figure 2. 1. Photos of a representative mafic sample from Taupō volcano illustrating the context of the olivine-hosted melt inclusions analysed in this study showing (**A**) a juvenile mafic enclave hosting olivine crystals with adhering and ingested rhyolitic pumice glass, (**B**) high-Mg olivine crystal hosting multiple large but partially crystalline melt inclusions and (**C**) rehomogenised glassy melt inclusions with a 35 µm laser pit from trace element analysis. Sourced from Barker et al. (manuscript in prep).

2.3 Crystal separation

Once the material for crushing was dry, at least 200 g of each sample was selected for crushing in a Rocklabs Boyd crusher. Before and after each sample was passed through the crusher, the machine was carefully cleaned with an industrial vacuum cleaner and compressed air, and then wiped with ethanol. These steps are to ensure the removal of any residual foreign material that may have not been cleaned during previous use of the crusher. The pumice samples were initially crushed at 1-2 cm plate widths, and then crushed at incrementally smaller plate widths, down to approximately 1-2 mm. In order to ensure that as many large crystals remained intact as possible, the crushed material was dry sieved after every pass through the machine. The sieve stack was constructed of 2, 1, and 0.5 mm sized sieves, leading to >2 mm, 1-2 mm, 0.5-1 mm, and <0.5 mm sized crystal fractions.

Crushed samples >2 mm were picked for loose crystals through the use of a binocular microscope with a polarizing lens attachment to aid in differentiating between the glass, and quartz and feldspar phenocrysts. Crushed samples 1-2 mm and 0.5-1 mm were density separated using water via a 2-stage process:

(1) Any material that floated in water was removed, as it was >99 % glass shards.

(2) The remaining denser material was then separated, using a standard 35 cm diameter plastic gold pan, into less-dense inclusion-bearing pumice, and a denser, crystal-rich residue.

Both products were then dried in the oven at >80°C for at least 72 hours. The crystal-rich dense residue was picked with fine tweezers under a binocular microscope (no polarising lens was required as the material was <1 % glass). Prior to picking, a magnet was run over the sample to pick up any magnetic phenocrysts; orthopyroxene crystals were typically studded with enough Fe-Ti oxide inclusions to enable magnetic differentiation. Crushed samples <0.5 mm were wet sieved at 250 µm and 125 µm size fractions, leading to 250-500 µm, 125-250 µm, and <125 µm size fractions. Samples were water density separated in a beaker at all size fractions to concentrate loose

crystals. Orthopyroxene was removed with a magnet. Free apatite crystals were density separated from the rest of the crystals with lithium heteropolytungstate (LST), which has a density of 2.9 g/mL, (apatite ≈ 3.19 g/cm^3, plagioclase ≈ 2.62 g/cm^3, quartz ≈ 2.65 g/cm^3).

2.4 Crystal mounting

Orthopyroxene and apatite crystals were mounted in epoxy resin rounds suitable for *in-situ* geochemical analytical techniques. Orthopyroxene crystals were selected from the 0.5-1 and 1.2 mm size fractions, and were chosen based on grain integrity (i.e. complete, non-fractured, euhedral grains). Apatite crystals were only selected for mounting if they had adhering glass selvedges (groundmass glass), which indicated that they were immersed in the melt in contrast to being trapped within phenocrysts. Apatite crystals were oriented with their c-axis perpendicular to the EPMA beam, after Goldoff et al. (2012). Orthopyroxene crystals were also analysed with their c-axis parallel to the probe beam, as the majority of apatite inclusions within orthopyroxene grew with their c-axes parallel to the c-axis of the host crystals. Once the epoxy resin had cured after at least 24 hours the mounted crystals were exposed by sanding with 800 to 2500 grit silicon carbide paper, and then polished with diamond suspension liquid (6 to 3 to 1 μm) on polishing laps to create appropriately smooth and flat surfaces of exposed crystal. Mounts were then carbon coated prior to major-element analysis by EPMA. The carbon coat was later removed prior to trace-element analysis by LA-ICP-MS.

2.5 *In-situ* major element techniques: Electron Probe Micro-Analysis (EPMA)

All major and volatile element analyses were conducted using a JEOL JXA-8230 electron probe micro-analyser (EPMA) at Victoria University of Wellington. The conditions under which analyses were run are different for each material, and are

specified briefly below. Appendix 2 details the exact EPMA procedures followed for each suite of analyses. Standardisation of elemental count rates and concentrations was accomplished using both natural and synthetic primary standards, and concentrations of 'unknown' secondary standards were calculated through the ZAF correction method. Table A1.1 provides data for the secondary standards routinely analysed. All EPMA data presented in this study are included as a spreadsheet in the electronic appendix.

2.5.1 Rhyolite glass

Melt inclusions hosted in normally zoned orthopyroxene cores were analysed, along with adhering groundmass glass (Figure 2.2b, e). During the programming of analytical points, care was taken not to leave the beam on over glass samples for too long to avoid liberating the volatile elements or causing losses of Na (Morgan and London, 1996). A correction was applied to the raw EPMA data to account for the fluorine-iron spectral peak interferences (section A2.6). Unless specified otherwise, the analytical conditions for glass analysis were 15 kV, 8 nA, 30 s peak and 15 s background, with a 10 µm circular beam. To minimise Na loss the peak search was skipped and count times were shorter at 10 s peak and 5 s background.

2.5.2 Basalt glass

Melt inclusions hosted in basaltic-andesite high-Mg olivine crystals were re-analysed for sulfur, chlorine, and fluorine contents (Figure 2.2a). For basaltic glass EPMA analysis the same procedure as that for analysing rhyolite glass was undertaken, but with a different suite of secondary standards.

2.5.3 Orthopyroxene

Orthopyroxene analyses were conducted in normally zoned cores immediately adjacent to already analysed melt inclusions (Figure 2.2b, e, f). The analytical conditions for the primary standards and the unknown samples were the same; 12 nA, 15 kV, spot beam, 30 s peak and 15 s background, default conditions, and a narrow peak search.

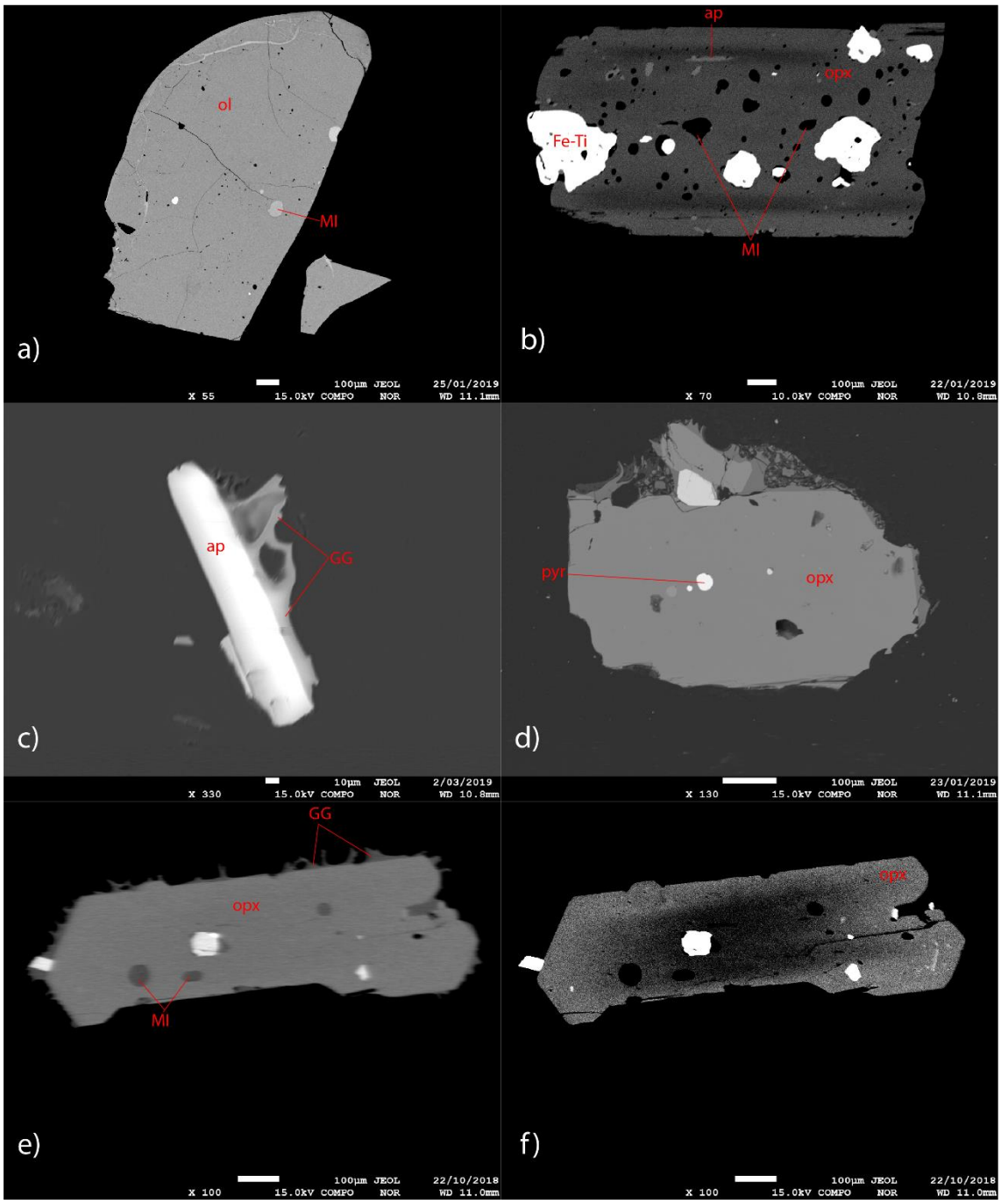

Figure 2. 2. Backscattered electron images of selected crystals. **a)** P950 Oruanui olivine with melt inclusion. **b)** P2368 Oruanui orthopyroxene with a zoned inherited core rich in melt inclusions, with additional Fe-Ti oxide and apatite inclusions. **c)** P1592 Oruanui free crystal apatite with adhering groundmass glass. **d)** Ω orthopyroxene with both a pyrrhotite and Fe-Ti inclusion. **e)** and **f)** Ω orthopyroxene with a zoned inherited core rich in inclusions, with adhering groundmass glass. Sample details in Table 2.1. ol = olivine, MI = melt inclusion, Fe-Ti = iron titanium oxide, opx = orthopyroxene, ap = apatite, GG = groundmass glass, pyr = pyrrhotite.

2.5.4 Apatite analysis procedure

Orthopyroxene-hosted and microphenocryst apatite crystals were analysed for major and volatile element contents (Figure 2.2b, c). During the programming of points to analyse, care was taken not to leave the beam on over samples for too long to avoid mobilising the volatile elements. The analytical conditions (besides peak search times) for the primary standards and the unknown crystals were the same; 4 nA, 10 kV, 10 µm beam, default conditions and a narrow peak search.

2.5.5 Sulfide analysis procedure

Sulfides hosted as inclusions within orthopyroxene cores were analysed for major elements (Figure 2.2d). The analytical conditions for the primary standards and the unknown crystals were the same; 60 nA, 15 kV, 1 µm beam, 30 s peak and 15 s background, default conditions and a narrow peak search (Liu et al., 2018).

2.5.6 Data reduction

Fluorine-corrected EPMA melt inclusion glass data were trimmed of any points whose totals did not fall within the range of 92 to 98 wt% total oxides. This range was chosen due to the large variation of H_2O in melt inclusions from Taupō volcano rhyolites (e.g. Dunbar et al., 1989a; Liu et al., 2006). Fluorine-corrected groundmass glass data were trimmed of any points whose totals fell outside 97 to 100 wt% total oxides. This range was chosen as groundmass glass data represents material quenched immediately prior to or during eruption from which any remaining volatile components are expected to have already exsolved, but pumiceous material is commonly secondarily hydrated. Apatite, orthopyroxene, and pyrrhotite raw EPMA data were trimmed of any points that fell outside ±1 wt% total oxides from the mode. Once trimmed, the analyses were normalised to 100 wt% for comparative purposes.

2.5.7 Error calculations

Error bars were calculated to 2 s.d. based on the secondary standards that were interspersed through each EPMA run. The errors for each standard used are presented in Table A1.1. The runs conducted on the EPMA in this study were analysed over several separate days, and thus with different conditions. As such, the error bars on the following volatile element graphs are drawn to represent the smallest, largest and average errors throughout the different analyses (the major element errors do not vary appreciably so only the average is displayed).

2.6 *In-situ* trace element techniques: Laser Ablation (LA) ICP-MS

All laser ablation ICP-MS analyses were conducted using a Resonetics S155-SE (193 nm) Eximer laser coupled to an Agilent 7900 ICP-MS at Victoria University of Wellington. Raw LA-ICP-MS data were processed with the Iolite software via an internal standard data reduction routine (Hellstrom et al., 2008). By adding EPMA-determined concentrations for a major element oxide (typically SiO_2 or CaO for silicate minerals/melts) into Iolite, the program can calculate by reference the trace element concentrations for the remaining elements (see Perkins and Pearce, 1995; Pearce et al., 1996 for further discussion). SiO_2 was used for internally standardisation of the rhyolite glass and orthopyroxene samples, whereas CaO was used for apatite samples. Primary and 'unknown' secondary standards were interspersed throughout the analysis runs every 10 points and were used to calibrate results and provide precision and accuracy estimates, respectively. Rhyolite glass NIST SRM612 was run as a primary standard and NIST SRM610 was run as a secondary standard for silicic glass and apatite, data for which are presented in Table A1.2. Tuning and optimisation of signal sensitivity and stability was achieved prior to sample analysis by rastering across the primary standards, and adjusting the flow of ultra-pure He gas. Rhyolite glass data were acquired over 30 s periods (with additional 60 s background) with 35 µm circular laser beam size pulsed at 10 hz. Apatite crystal data were acquired over 20 to 30 s periods (with additional 60 s background) with 35 µm laser beam sized pulsed at 10 hz.

All LA-ICP-MS data presented in this study are included as a spreadsheet in the electronic appendix.

3. Results

3.1 Major element data

Table 3.1 provides representative maximum and minimum values for orthopyroxene-hosted melt inclusion and groundmass glass analyses for each Taupō silicic sample to illustrate the range of compositions held within each individual clast, along with representative average analyses of olivine-hosted melt inclusions for the three Oruanui mafic samples. Due to the limited number of analyses on units Ψ, C, and S, and the compositional similarities between the dacite units and the rhyolite units, the post-Oruanui units have been compiled into two populations: post-Oruanui dacite (Ψ, Ω), and post-Oruanui rhyolite (C, S, Y6). For complete data sets see the electronic appendix.

3.1.1 Glass

Melt inclusion compositions from the post-Oruanui dacite and rhyolite, and Oruanui LSR and HSR span 69-73, 73-76, 74-78, and 75-78 wt% SiO_2 respectively, and groundmass glass compositions span 72-73, 74-77, 74-75, and 76-78 wt% SiO_2 respectively. Both the Oruanui and post-Oruanui data suites plot within the range of values previously published for glass separates or melt inclusions from the corresponding units (e.g. Sutton et al., 1995, 2000; Liu et al., 2006; Wilson et al., 2006; Allan et al., 2013, 2017; Barker et al., 2015; Myers et al., 2018, 2019). Plots of major oxides versus SiO_2 are displayed in Figure 3.1. Strong negative linear trends exist between SiO_2 and all major oxides with the exception of K_2O, which exhibits a flat trend through the post-Oruanui and Oruanui low-silica rhyolite (LSR) compositions, and increases with increasing SiO_2 Oruanui high-silica rhyolite (HSR). There is little difference between melt inclusion and groundmass glass compositions for post-Oruanui units, LSR, and HSR for all oxides with the exceptions of Al_2O_3 and FeO (and K_2O for Ou HSR), in which groundmass glass values are lower.

Table 3. 1. Representative minimum and maximum major oxide and volatile element analyses of Oruanui and post-Oruanui silicic melt inclusions (MI) and groundmass glass (GG), and average major oxide and volatile element analyses of Oruanui basaltic melt inclusions. Major oxides in wt%, volatile elements in ppm

	Sample		SiO_2		TiO_2		Al_2O_3		FeO		MnO		MgO		CaO		Na_2O		K_2O		Cr_2O_3		S		F		Cl	
			min	max	min	max	min	max	min	max	min	max	min	max	min	max	min	max	min	max	min	max	min	max	min	max	min	max
High silica rhyolite	P1453	*MI n* = 15	75.45	77.78	0.08	0.25	11.99	13.74	1.57	2.01	0.03	0.08	0.05	0.23	0.71	1.6	2.81	4.54	2.63	4.67	0	0.04	13	63	248	721	1613	2610
		GG n = 34	76.81	77.99	0.09	0.19	12.43	12.88	1.13	1.98	0.02	0.11	0.1	0.17	1	1.19	3.46	4.13	2.87	3.16	0	0.06	0	61	307	1212	1803	2549
	P1592	*MI n* = 8	75.11	77.87	0.09	0.25	11.97	13.6	1.22	1.89	0.02	0.08	0.05	0.16	0.8	1.29	3.13	4.17	2.6	4.16	0	0.02	20	51	406	779	1811	2859
		GG n = 2	77.36	77.79	0.12	0.13	12.42	12.57	1.18	1.41	0.02	0.06	0.1	0.12	1.01	1.01	3.74	3.84	3.17	3.36	0.01	0.01	20	25	565	706	2120	2402
	P2366	*MI n* = 13	76.86	78.22	0.11	0.14	12.08	12.76	1.16	1.64	0	0.09	0.09	0.28	0.8	1.07	2.87	3.94	3.29	4.78	0	0.03	0	65	263	781	1801	2187
		GG n = 29	77.44	78.08	0.08	0.13	12.29	12.62	1.13	1.48	0.02	0.1	0.08	0.15	0.96	1.08	3.64	3.96	3.08	3.37	0	0.05	0	49	349	854	1540	2579
	P2367	*MI n* = 16	75.21	77.93	0.09	0.24	12.09	13.92	1.46	2.14	0.02	0.07	0.07	0.15	0.68	1.33	3.26	4.03	2.84	4.12	0	0.03	20	50	371	594	2031	2500
		GG n = 25	76.96	77.75	0.08	0.14	12.3	12.81	1.26	1.8	0	0.09	0.1	0.16	1.02	1.14	3.5	4	2.84	3.25	0	0.04	0	50	448	773	1814	2345
	P2369	*MI n* = 9	76.45	77.8	0.09	0.16	11.86	12.95	1.49	1.99	0.01	0.1	0.1	0.16	0.8	1.1	3.29	3.74	3.43	3.93	0	0.03	13	65	444	574	1882	2150
		GG n = 2	77.44	77.48	0.08	0.11	12.44	12.57	1.42	1.53	0.01	0.04	0.12	0.13	1.12	1.14	3.85	3.92	3.02	3.05	0	0	13	39	459	567	1982	2060
	P2370	*MI n* = 6	75.14	76.95	0.11	0.18	12.7	13.87	1.6	1.85	0.05	0.1	0.08	0.16	1.06	1.31	3.76	4.19	3.02	3.65	0	0.03	25	50	293	445	2009	2310
		GG n = 2	77.31	77.56	0.1	0.12	12.52	12.61	1.32	1.37	0.02	0.04	0.11	0.11	0.99	1.02	3.71	3.91	3.31	3.36	0	0.01	25	37	425	466	2008	2029
Low silica rhyolite	P2361	*MI n* = 29	74.16	76.75	0.17	0.27	12.49	13.83	1.99	2.79	0.06	0.16	0.04	0.28	1.11	1.71	3.81	4.16	2.6	2.95	0	0.04	37	116	346	847	1590	1952
		GG n = 10	74.51	75.04	0.23	0.27	13.33	13.65	1.98	2.46	0.07	0.12	0.24	0.27	1.42	1.54	4.32	4.6	2.73	3.01	0	0.01	36	95	519	626	1520	1861
	P2362	*MI n* = 36	74.09	76.87	0.21	0.26	11.45	13.41	1.64	4.89	0.04	0.21	0.02	1.61	1.31	1.54	3.64	4.38	2.36	2.87	0	0.02	25	91	360	950	1497	2027
		GG n = 12	74.65	75.19	0.23	0.28	13.09	13.39	2.24	2.7	0.05	0.13	0.21	0.28	1.37	1.55	4.12	4.57	2.61	2.97	0	0	12	62	575	714	1652	1901
	P2368	*MI n* = 19	74.72	76.11	0.2	0.26	13.01	13.66	2.02	2.44	0.05	0.11	0.05	0.25	1.4	1.59	3.86	4.34	2.7	2.97	0	0.05	37	141	713	920	1793	1956
		GG n = 1	74.73		0.25		13.59		2.17		0.11		0.24		1.49		4.21		2.93		0		24		958		1760	
Post-Oruanui	ψ	*MI n* = 5	71.54	72.43	0.46	0.58	14.16	14.81	2.81	3.05	0.05	0.09	0.52	0.62	2.3	2.5	3.87	4.01	2.54	2.81	0	0.01	86	112	720	864	1824	2359
	Ω	*MI n* = 21	69.57	73.27	0.41	0.58	13.91	15.97	2.66	3.78	0.06	0.12	0.44	0.76	2.08	3.54	3.57	4.22	1.89	3.1	0	0.04	49	111	606	787	1709	2474
		GG n = 8	72.16	73.21	0.41	0.58	13.9	14.19	2.65	3.02	0.06	0.1	0.38	0.54	2.15	2.48	3.83	4.14	2.67	2.85	0	0.02	12	83	521	723	1358	1849
	C	*MI n* = 5	74.27	75.9	0.15	0.21	13.31	14.12	1.68	2.28	0.03	0.08	0.13	0.2	1.37	1.87	3.34	3.78	3.1	3.65	0	0.01	38	90	632	717	1639	1933
		GG n = 3	75.62	76.4	0.16	0.17	12.97	13.38	1.74	1.78	0.02	0.07	0.15	0.19	1.38	1.51	3.88	4.13	2.95	3.17	0	0.02	36	85	682	741	1767	1827
	S	*MI n* = 2	74.36	75.7	0.15	0.22	13.21	13.94	2.18	2.53	0.07	0.08	0.18	0.23	1.36	1.46	3.79	3.98	2.92	3.08	0.01	0.02	37	75	630	638	1844	2074
		GG n = 2	75.98	76.01	0.18	0.18	13.07	13.26	1.87	1.99	0.06	0.07	0.16	0.17	1.3	1.3	3.9	4.09	2.91	2.99	0	0.01	25	36	544	624	1870	1888
	Y6	*MI n* = 25	73.68	76.63	0.18	0.25	12.74	14.21	2.02	2.83	0.06	0.15	0.03	0.29	1.29	1.69	3.71	4.29	2.63	3.05	0	0.04	25	112	399	707	1618	2178
		GG n = 54	74.6	75.53	0.21	0.29	13.29	13.72	1.76	2.59	0.04	0.16	0.19	0.3	1.4	1.61	3.79	4.66	2.52	3.01	0	0.06	0	62	505	1758	1669	3552
			ave		ave		ave		ave		ave		ave		ave		ave		ave		ave		ave		ave		ave	
Taupō mafic	P950	*MI n* = 5	48.29		0.57		14.78		11.01		0.16		13.38		9.85		1.5		0.16		0.03		1374		502		736	
	P2224	*MI n* = 5	49.71		0.73		15.15		10.5		0.17		10.91		10.26		1.87		0.36		0.01		1587		731		890	
	P560	*MI n* = 6	48.57		0.71		15.42		11.25		0.17		11.1		10.55		1.78		0.18		0.02		1260		551		777	

MI melt inclusion*, GG* groundmass glass*, min* minimum value, *max* maximum value, *ave* average value, *n* number of crystals analysed

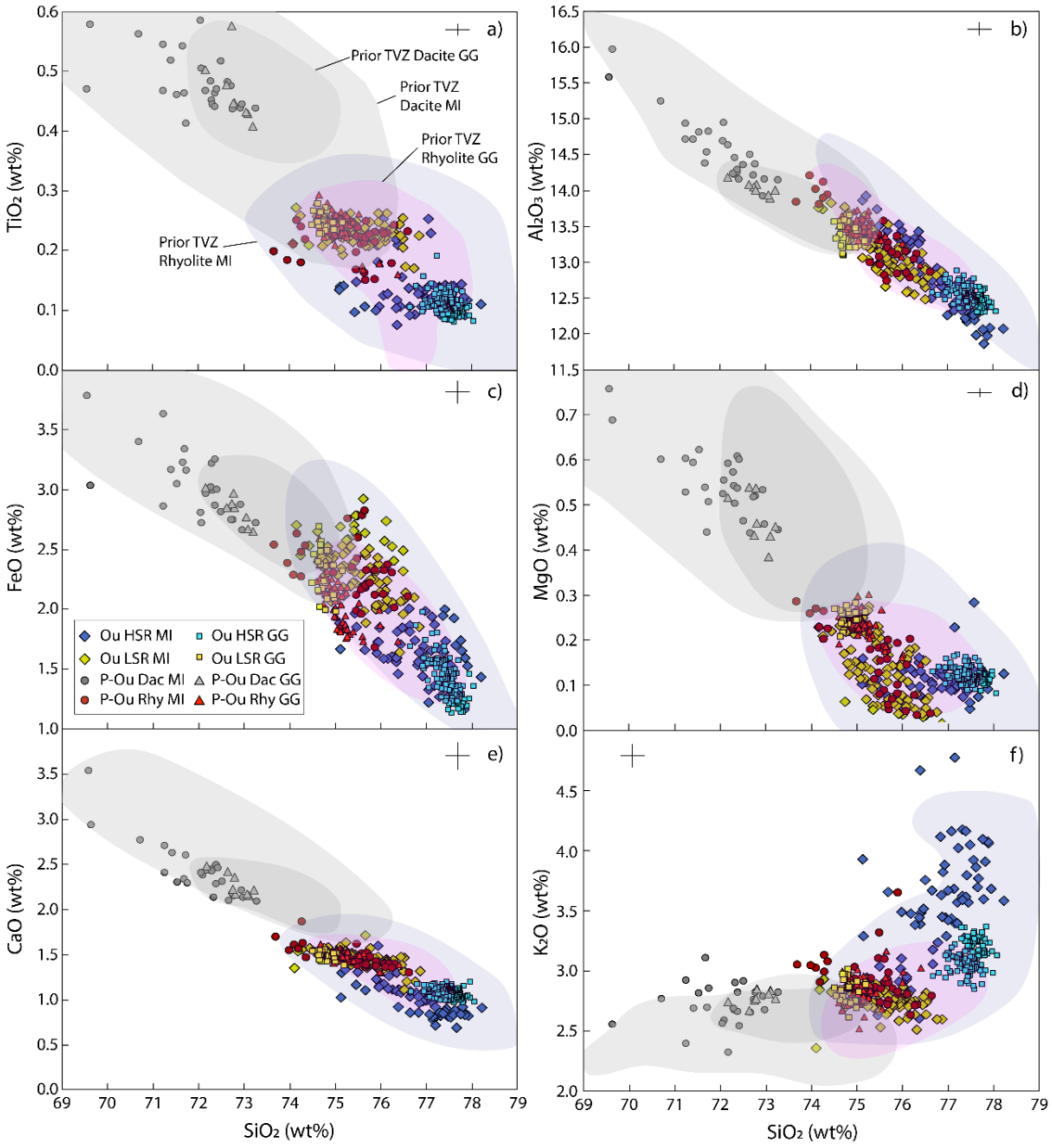

Figure 3. 1. Selected major element oxide (wt%) against SiO_2 (wt%) for orthopyroxene-hosted melt inclusions (MI) and groundmass glass (GG) from the Oruanui (Ou) eruption high and low-silica rhyolites (HSR and LSR respectively), post-Oruanui dacite units (P-Ou Dac), and post-Oruanui rhyolite (P-Ou Rhy). Previously published data from plagioclase and/or quartz and/or orthopyroxene-hosted inclusions are represented by coloured fields (purple = post-Oruanui SG3 rhyolite compositions; orange = Ou HSR), (Liu et al., 2006; Johnson et al., 2013; Bégué et al., 2014; Barker et al., 2015; Allan et al., 2017). Error bars represent the average 2 s.d. errors based on repeat analyses of VG-568.

3.1.2 Orthopyroxene

Major element compositions of the host orthopyroxene crystals were measured immediately adjacent to the hosted melt inclusions in the orthopyroxene cores for each eruption studied. The enstatite content (mol%) was calculated as 100*(Mg/Ca + Mg + ΣFe), and is presented for HSR and post-Oruanui dacite in Figure 3.2, and for post-Oruanui rhyolite in Figure 3.3. HSR compositions give a wide spread of enstatite content between 46 to 60 mol%, with prominent mode between 51 and 53 mol%. Dacite units give the highest enstatite contents, with the majority between 59 and 65 mol%. Post-Oruanui rhyolite display relatively lower enstatite contents, with all analyses between 45 and 52 mol%.

The SiO_2 content (wt%) of several analysed melt inclusions is graphed against the enstatite content (mol%) of the host orthopyroxene crystal immediately adjacent to the melt inclusions in Figure 3.4. SiO_2 values decrease with increasing enstatite values for all compositions analysed. In contrast, Al increases with increasing enstatite content (Figure 3.5).

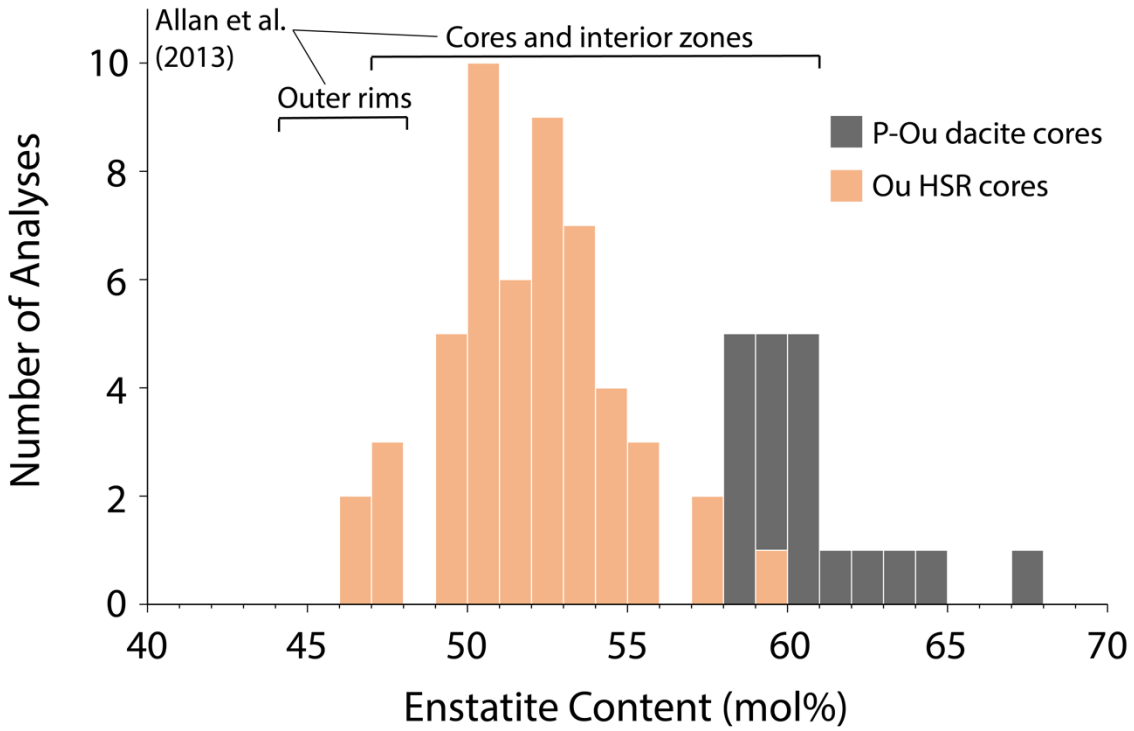

Figure 3. 2. Stacked histogram displaying the enstatite content (mol%) of orthopyroxene immediately adjacent to melt inclusions analysed in this study, from Oruanui high-silica rhyolite (Ou HSR) and post-Oruanui dacite (P-Ou dacite). The general fields of the outer rims, and the cores and interior zones from Allan et al. (2013) are denoted to display the difference between them.

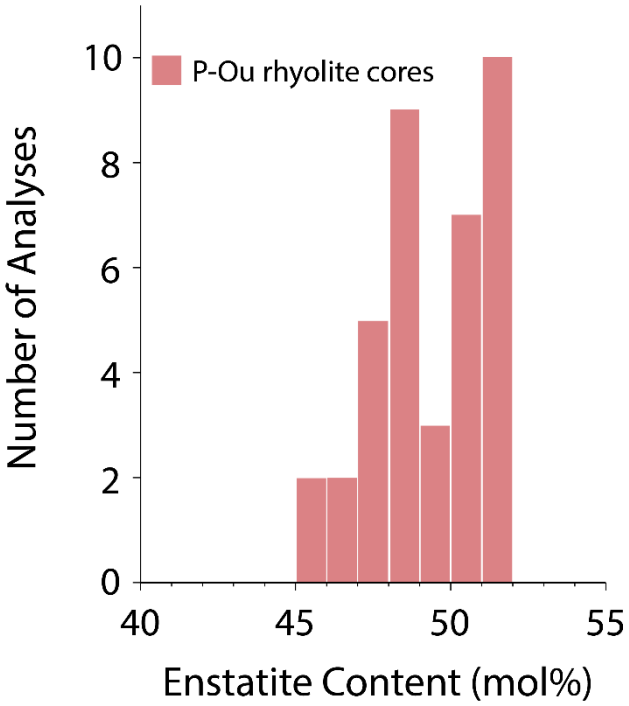

Figure 3. 3. Stacked histogram displaying the enstatite content (mol%) of orthopyroxene immediately adjacent to melt inclusions analysed in this study from post-Oruanui rhyolite (P-Ou rhyolite cores).

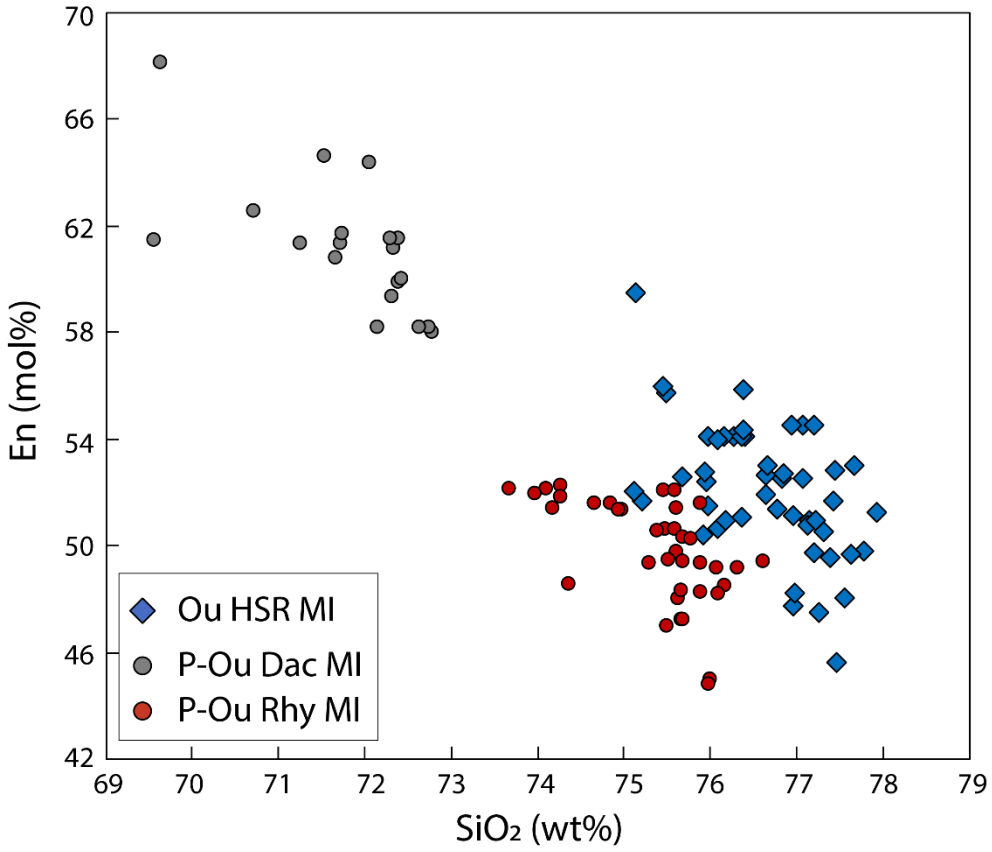

Figure 3. 4. SiO_2 (wt%) of melt inclusions versus the enstatite content (mol%) of orthopyroxene host crystals immediately adjacent to the melt inclusions, for Oruanui high-silica rhyolite (Ou HSR), and post-Oruanui dacite and rhyolite (P-Ou Dac and P-Ou Rhy respectively).

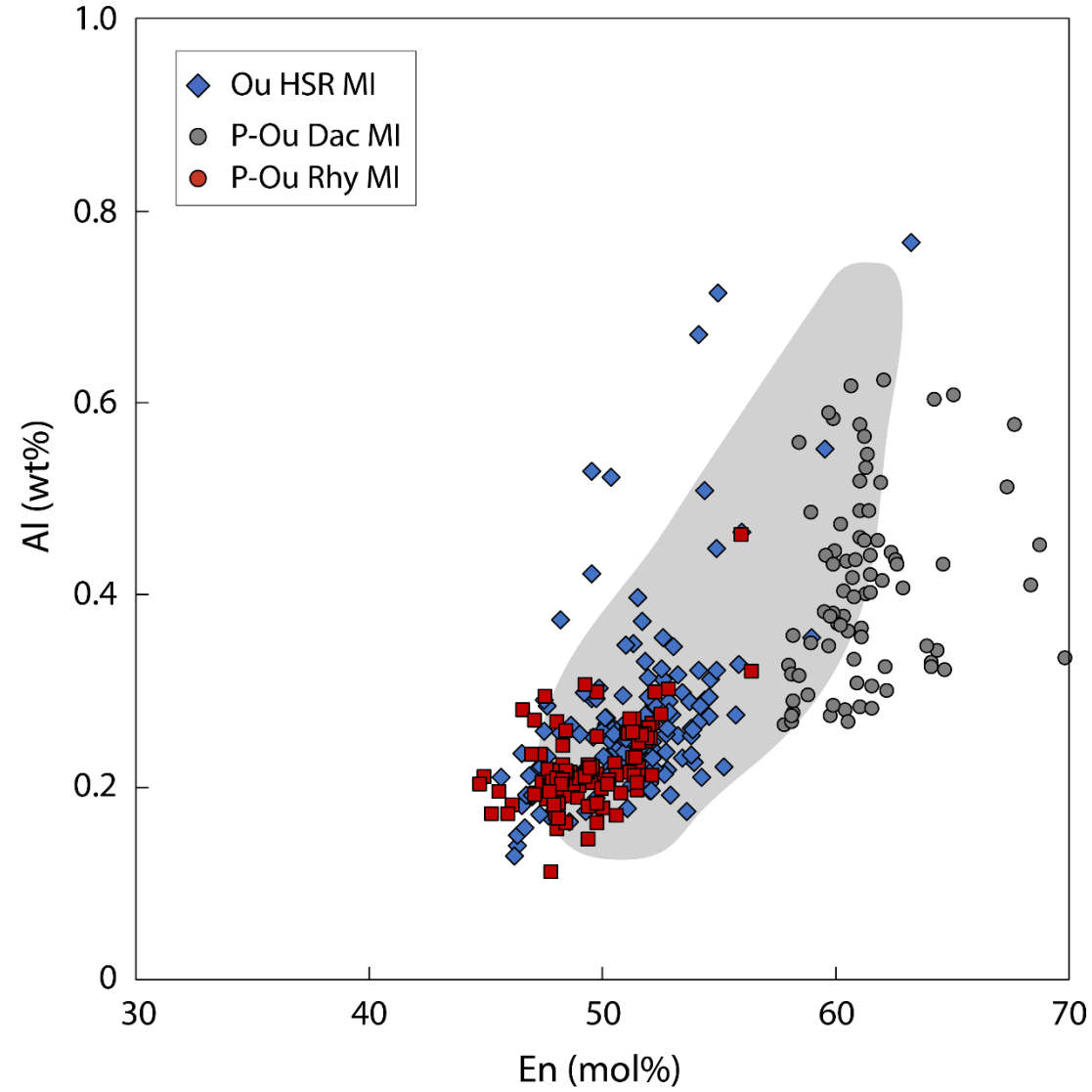

Figure 3. 5. Enstatite content (mol%) versus Al (wt%) for orthopyroxene cores from Oruanui high-silica rhyolite (Ou HSR), and post-Oruanui dacite and rhyolite (P-Ou Dac and P-Ou Rhy respectively). Data from Allan et al. (2017) is denoted with a grey field.

3.1.3 Oruanui high-silica rhyolite apatite

Relationships between F, Cl, P_2O_5, and CaO in Oruanui apatite crystals are plotted in Figure 3.6. F increases with decreasing P_2O_5, with the microphenocryst population having higher F and lower P_2O_5 than the inclusion population. In contrast, Cl decreases with decreasing P_2O_5, with the inclusion population having higher Cl than the microphenocryst population. Cl/F decreases with P_2O_5 between the inclusion population to the microphenocryst population, and then appears to plateau. Two distinct trends are observed when CaO is graphed against P_2O_5, with CaO exhibiting a

similar range in values between the inclusion and microphenocryst apatite. At a given P_2O_5 value, the inclusions have higher CaO. The majority of SO_3 values were below detection limits (~600 ppm) for all apatite analyses, and there were no identifiable trends for the few values greater than ~600 ppm.

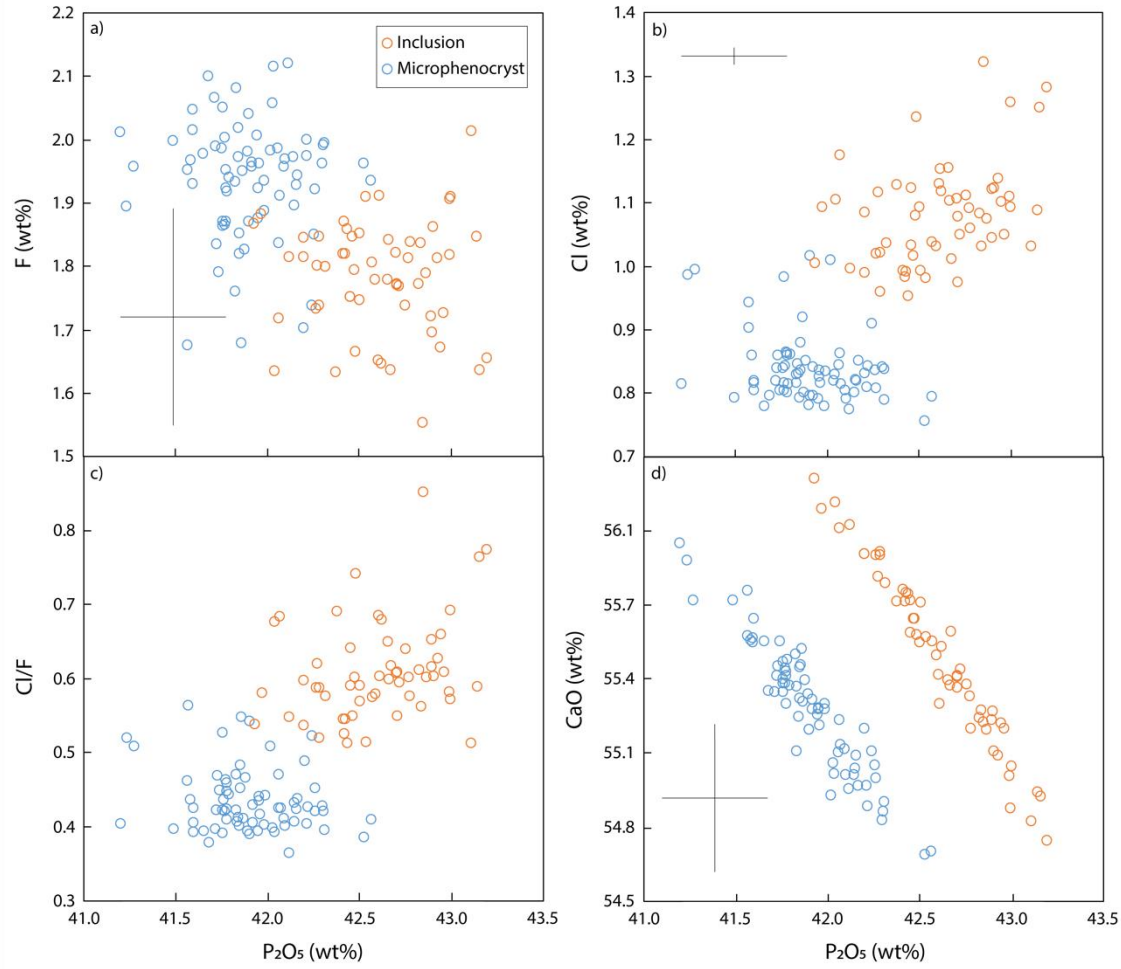

Figure 3. 6. a) F (wt%), **b)** Cl (wt%), **c)** Cl/F **d)** CaO (wt%) versus P_2O_5 (wt%), for orthopyroxene-hosted apatite and microphenocryst apatite crystals from Oruanui rhyolite. Error bars represent average 2 s.d. based on repeat analyses of Durango apatite.

3.1.4 Post-Oruanui dacite-hosted pyrrhotite

Due to the limited number of samples and the small size (<25 µm) of pyrrhotite inclusions in dacite units Ψ and Ω, only five successful analyses were conducted in this study (Figure 3.7). The pyrrhotite chemical formula is $Fe_{1-x}S$, where $0<x<0.2$ and the ratio expressed in moles. The acquired data points cluster at relatively constant Fe (mol) and more variable S (mol) values within the range that defines pyrrhotite.

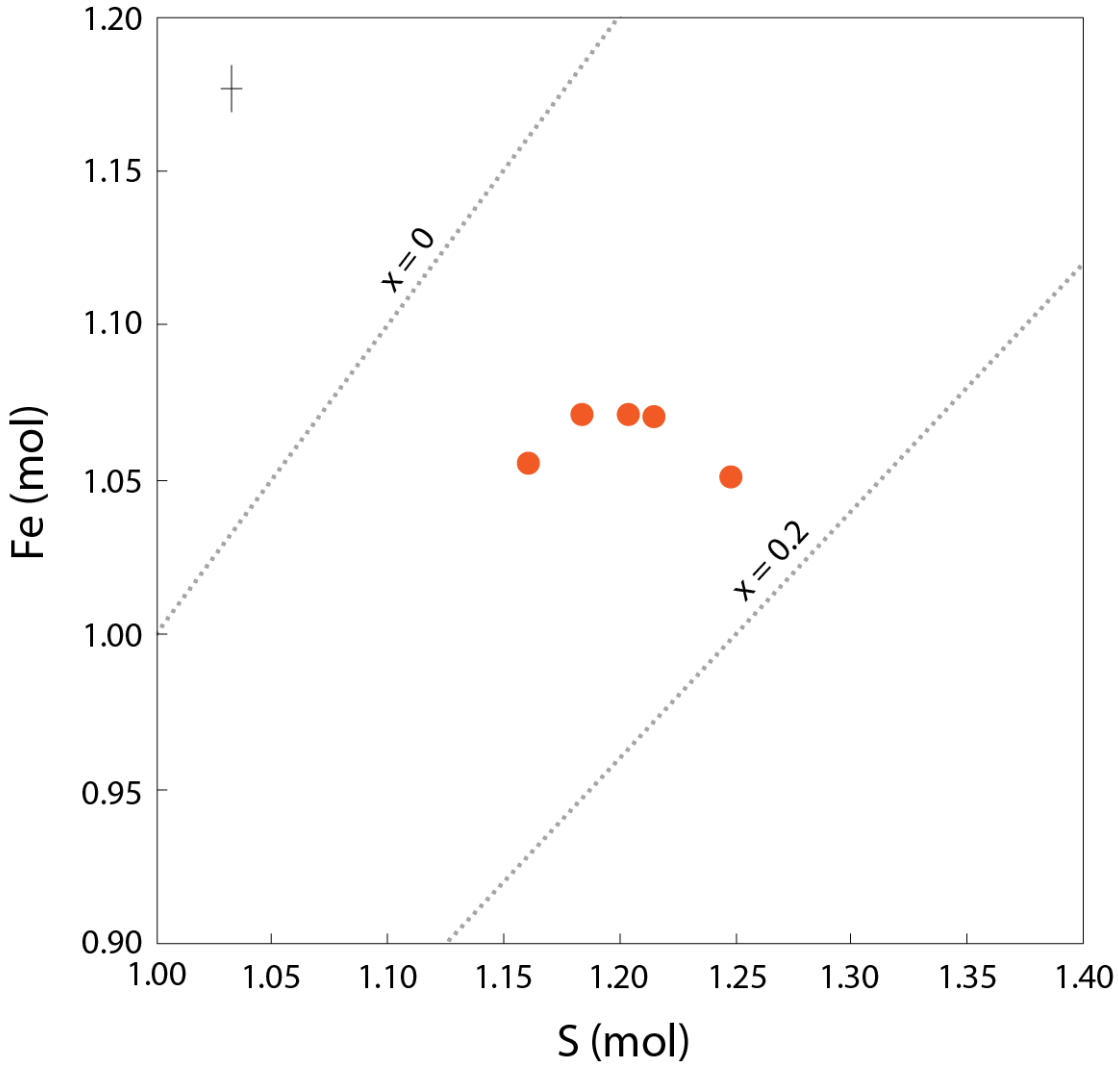

Figure 3. 7. Fe (mol) vs S (mol) for orthopyroxene-hosted pyrrhotite inclusions from units Ψ and Ω. Dotted grey lines indicate the range of acceptable *X* values for pyrrhotites chemical formula $Fe_{1-x}S$. The error bar represents the average 2 s.d. based on repeated analyses of Elba Pyrite.

3.2 Volatile element data

Plots of sulfur, chlorine, and fluorine versus SiO_2 are displayed for basalt, dacite, and rhyolite melt compositions in Figure 3.8. Sulfur and fluorine increase strongly with increasing SiO_2 in the basalt olivine-hosted melt inclusions, whereas chlorine increases weakly (~900-1900 ppm, ~200-800 ppm, and ~500-900 ppm, respectively) as SiO_2 increases from ~45-50 wt%.

▼ **Figure 3. 8.** Sulfur, chlorine, and fluorine versus SiO_2 for olivine-hosted basaltic melt inclusions (MI) compared with the Oruanui eruption high- and low-silica rhyolites, and the post-Oruanui dacites and rhyolites (symbols as previously described in Fig. 3.1). Two populations of data in the sulfur and chlorine basaltic melt compositions (Oruanui, Unit S) are provided by Barker et al. (manuscript in prep). Fluorine detection limits for the basaltic melt analyses and the dacitic to rhyolitic analyses are denoted with small-dashed and large-dashed black lines respectively. Error bars represent the average 2 s.d. errors for the basaltic compositions based on repeat analyses of VG-A99 (S and Cl) and IO (F).

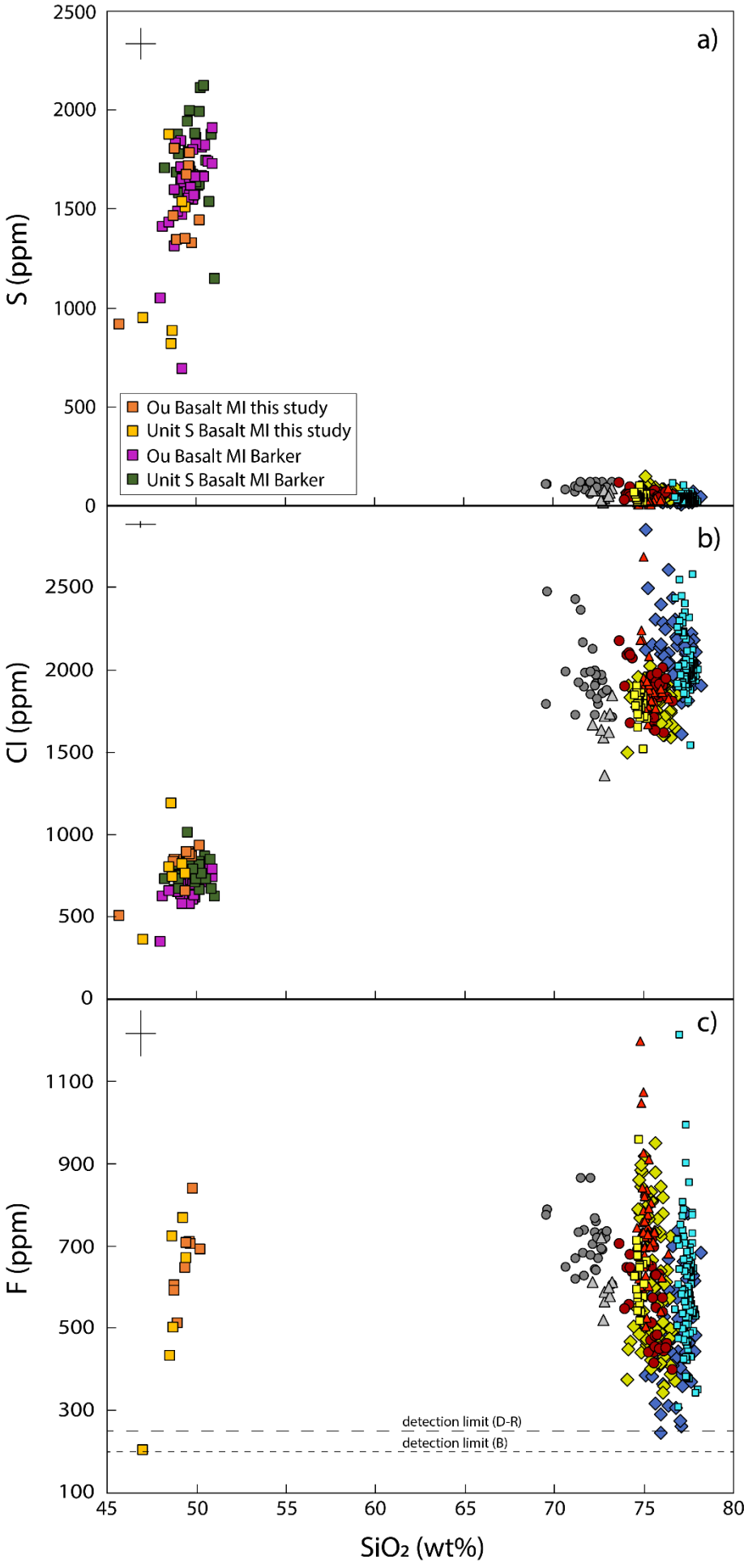
a)
b)
c)
S (ppm)
Cl (ppm)
F (ppm)
SiO2 (wt%)
Ou Basalt MI this study
Unit S Basalt MI this study
Ou Basalt MI Barker
Unit S Basalt MI Barker
detection limit (D-R)
detection limit (B)
2500
2000
1500
1000
500
0
1100
900
700
500
300
100
45
50
55
60
65
70
75
80

Plots of sulfur, fluorine, and chlorine versus SiO_2 are displayed for dacite and rhyolite melt compositions in Figure 3.9. When compared with the olivine-hosted basalt melt inclusions, the groundmass glasses and melt inclusions in the orthopyroxene-hosted dacite-rhyolite melt inclusions have markedly lower sulfur concentrations. Sulfur is below 150 ppm, with 97 % of analyses being 100 ppm or less (Figure 3.9a). There is a slight decrease in sulfur as SiO_2 increases between the dacite and rhyolite compositions. Sulfur in the dacite units decreases as SiO_2 increases. For all other compositions sulfur remains relatively constant with increasing SiO_2. Although not apparent on the figures due to a clustering effect, the average sulfur groundmass glass (GG) contents are lower than the melt inclusions (MI) for every compositional population analysed. There is a decrease in sulfur between LSR and HSR compositions.

Chlorine decreases as SiO_2 increases for all compositional populations (Figure 3.9b). There is an increase in chlorine between LSR melt inclusions and the HSR melt inclusions. Dacite and HSR compositions have lower chlorine contents (and higher SiO_2) in the groundmass glass populations relative to the melt inclusion populations, but there is little difference between the groundmass glass and melt inclusion compositions for subunit Y6 and LSR samples, with the exception of a single Y6 groundmass glass outlier at ~2700 ppm. There is a small population of HSR groundmass glass with elevated chlorine levels.

Fluorine decreases with increasing SiO_2 for LSR, and post-Oruanui dacite and rhyolite melt inclusions (Figure 3.9c). In contrast, fluorine in HSR melt inclusions increases with increasing SiO_2 and there is a population of LSR melt inclusions with elevated fluorine. The dacite compositions have lower fluorine values in the groundmass glass relative to the melt inclusions. HSR, LSR, and post-Oruanui rhyolite have significant variation in their groundmass fluorine contents (306 to 1212 ppm, 519 to 958 ppm, and 504 to 1200 ppm, respectively) over a narrow range in SiO_2.

▼ **Figure 3. 9.** Sulfur, chlorine, and fluorine versus SiO_2 for orthopyroxene-hosted melt inclusions (MI) and groundmass glass (GG) from the Oruanui eruption high- and low-silica rhyolites (HSR and LSR, respectively), and the post-Oruanui dacites and rhyolites (P-Ou Dac and P-Ou Rhy, respectively). Previously published data from plagioclase and/or quartz and/or orthopyroxene-hosted inclusions are represented by coloured fields (purple = post-Oruanui subgroup 3 rhyolite compositions; orange = HSR: Dunbar et al., 1989a; Hervig et al., 1989; Dunbar and Kyle, 1993; Bégué et al; 2015a, 2015b, 2017). Error bars represent the maximum, average, and minimum 2 s.d. errors based on repeat analyses of VG-568 (S and Cl) and VG-A99 (F). Detection limits for S and F are denoted by dashed horizontal lines. The Cl detection limit is below the presented vertical axis values.

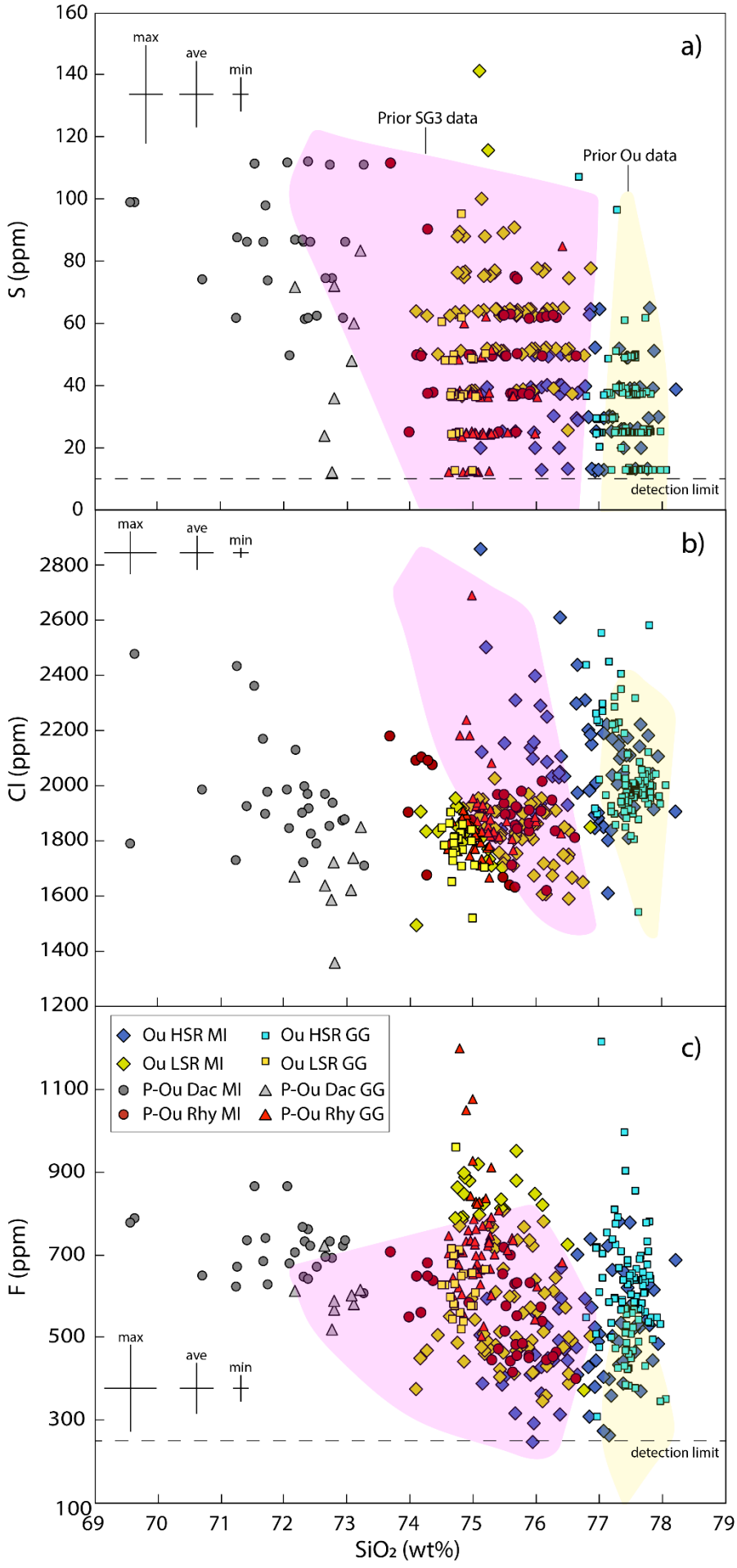
a)
b)
c)
max
ave
min
Prior SG3 data
Prior Ou data
detection limit
S (ppm)
Cl (ppm)
F (ppm)
SiO₂ (wt%)
Ou HSR MI
Ou LSR MI
P-Ou Dac MI
P-Ou Rhy MI
Ou HSR GG
Ou LSR GG
P-Ou Dac GG
P-Ou Rhy GG

2

3.3 Trace element data

3.3.1 Orthopyroxene-hosted melt inclusions

Selected trace elements strontium and yttrium, (Sr, Y) are graphed against sulfur, chlorine, and fluorine in Figure 3.10 for LSR and HSR, and post-Oruanui dacite and rhyolite compositions, to show volatile behaviour with the crystallisation of specific minerals (Y content of amphibole increases with decreasing depth, and Sr content of plagioclase decreases with decreasing depth: Allan et al., 2017). Of the post-Oruanui rhyolite compositions analysed here, only Unit C contains amphibole (Barker et al., 2015), and as such it has been labelled in the Y plots. Due to size limitations of melt inclusions, few data points were successfully recorded for each eruptive unit by LA-ICP-MS. Only one datum for the post-Oruanui dacite compositions was measured, and it is included for reference, but not included in the description or discussion. Sulfur decreases with decreasing Sr and Y for all compositional populations analysed. Chlorine decreases with Y for the post-Oruanui rhyolite apart from Unit C (the amphibole-bearing unit). Chlorine decreases from Oruanui HSR to LSR, while Y increases, highlighting the changing behaviour of these volatiles with amphibole crystallisation. Fluorine is relatively stable with decreasing Y in the post-Oruanui rhyolites, with one outlier of lower fluorine content. Fluorine and Y both increase from Oruanui HSR to LSR.

3.3.2 Oruanui high-silica rhyolite apatite

Zirconium, lanthanum, and europium (Zr, La, Eu) are plotted against fluorine and chlorine for orthopyroxene-hosted and microphenocryst apatite in Figure 3.11, to show how volatile behaviour in apatite varies with the crystallisation of compatible and incompatible elements (Zr = compatible in zircon, Eu = compatible in plagioclase and apatite, La = incompatible). Zr and Eu increase between the orthopyroxene-hosted and microphenocryst apatite, with decreasing chlorine and increasing fluorine. La decreases between the orthopyroxene-hosted and microphenocryst apatite, with decreasing chlorine and increasing fluorine.

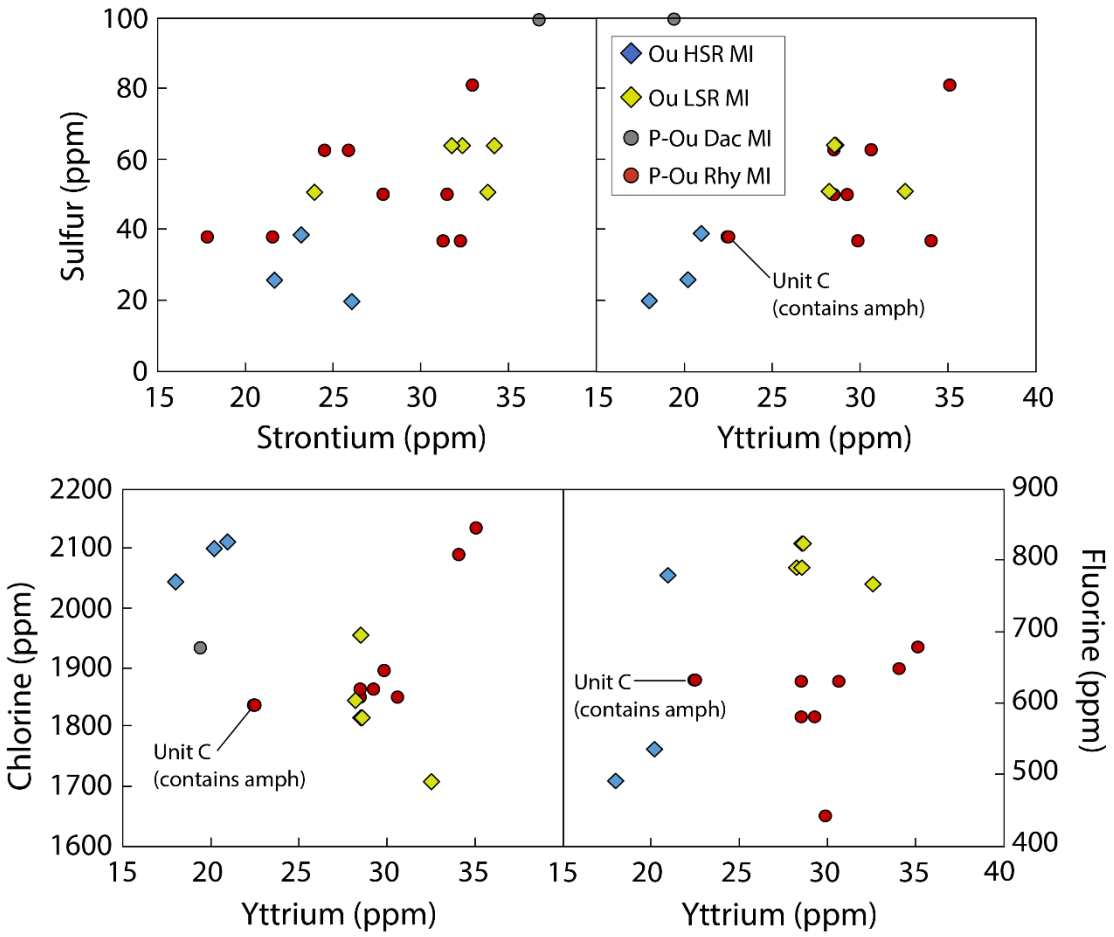

Figure 3. 10. Selected trace element (ppm) versus sulfur (ppm) and chlorine (ppm) plots for melt inclusions from Oruanui high- and low-silica rhyolite (Ou HSR MI and Ou LSR MI respectively), and post-Oruanui dacite and rhyolite compositions (P-Ou Dac and P-Ou Rhy respectively).

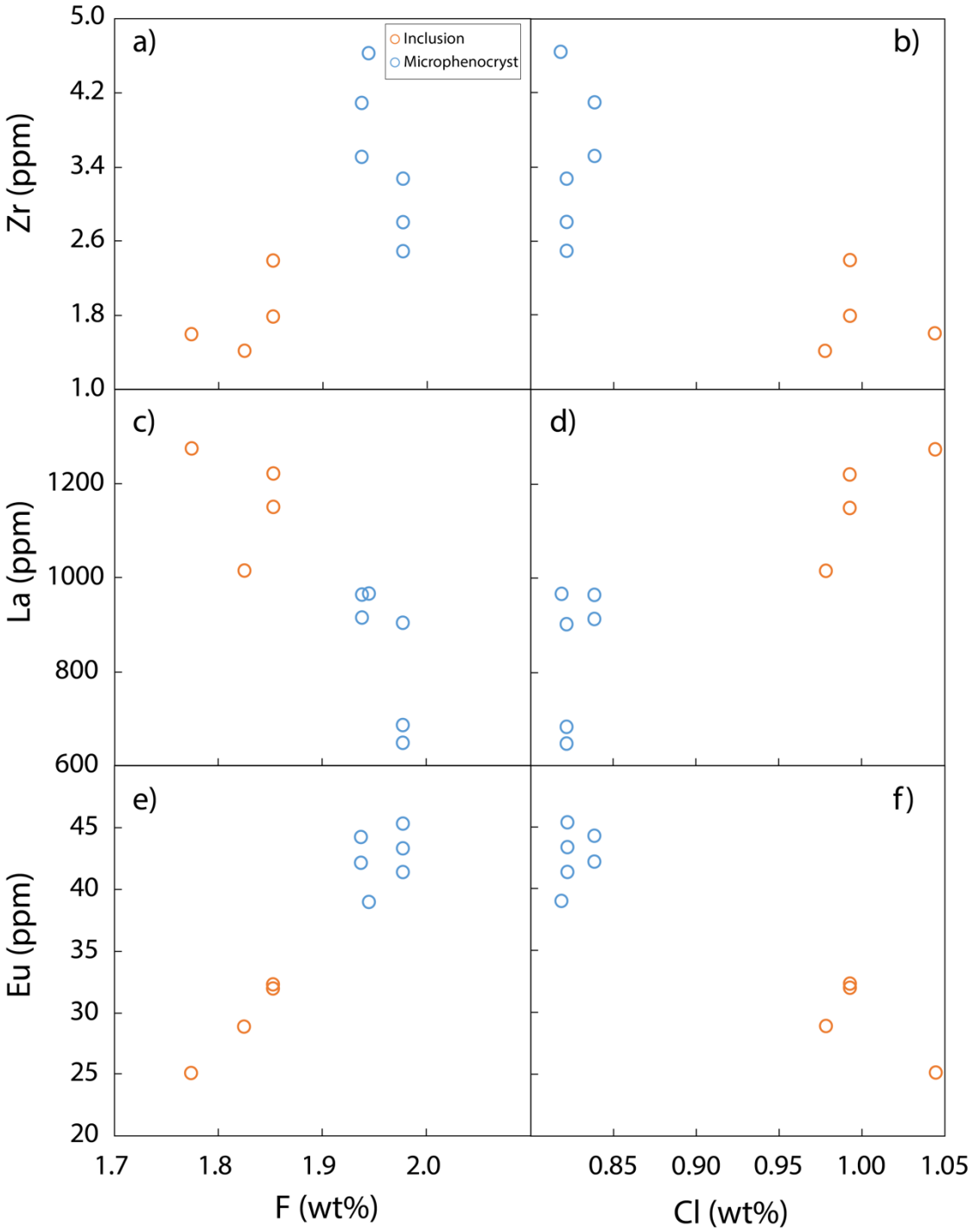

Figure 3. 11. Selected trace element (ppm) versus fluorine and chlorine (wt%) plots for orthopyroxene-hosted apatite inclusions and microphenocryst apatite.

4. Discussion

4.1 Introduction

Constraining the basalt and dacite to rhyolite end-member chemistries through a study of the melt inclusions in Taupō volcano eruptives has provided valuable insight into the end-member pre-eruptive melt compositions. The lack of compositionally intermediate melt inclusions means that it is challenging to directly infer the transportation pathway of volatiles from source magmas to surface. However, other lines of evidence from mineralogy and crystal chemistry are presented and discussed here to provide constraints around volatile budgets and pathways. Although this is the first study of TVZ eruptives to incorporate apatite chemistries, relative changes in composition at different depths (inferred from apatite either hosted in orthopyroxene or microphenocryst in groundmass glass) are useful in tracking the partitioning behaviours of sulfur, chlorine, and fluorine. Key questions that this discussion addresses are as follows:

1. Is it possible to precisely and accurately measure the volatile contents of deep magma using melt inclusions and apatite crystals hosted within the inherited cores of major mineral phases?
2. Do the volatile contents of the glass and apatite crystals vary significantly between materials inferred to be from the deeper crystal mush reservoir versus the shallower melt-dominant magma body?
3. What are the plausible physical processes by which volatiles are lost in Taupō volcano's magmatic system?
4. Is it possible to infer the volatile pathway(s) from the source mafic magmas to the surface despite the compositional gap in the available glass samples?

New analytical procedures using EPMA techniques have increased the precision and accuracy of volatile element analyses on small (20-100 μm) glass and crystal inclusions. The ubiquity of inherited cores in orthopyroxene (~90 %: Allan et al., 2013; 2017) and of melt and apatite inclusions in those cores, paired with the improved analytical

techniques, allow the questions outlined above to be further investigated. Expanded and new data sets presented in this thesis (Figures 3.6, 3.8, 3.9; electronic appendix) enable new interpretations on the behaviour and transport of S, Cl, and F. This chapter will discuss the behaviours of sulfur, chlorine, and fluorine in magmas, and then present an integrated model for the volatile transport pathway through the magmatic system beneath Taupō volcano.

4.2 Key inferences from previous textural and petrologic studies

4.2.1 Inherited cores and groundmass glass

The tight clustering of Oruanui orthopyroxene outer rims at lower enstatite (~46 mol%) and Al (~2000 ppm) contents relative to the wide range of higher enstatite contents (~46 to ~64 mol%) and Al (~1000 to 9000 ppm) exhibited by orthopyroxene cores and interiors signifies their different magmatic origins (Figure 3.2: Allan et al., 2013, 2017). Higher enstatite contents are inferred to represent crystal origins in hotter, less evolved melts, and the total-Al geobarometer of Ridolfi et al. (2010), (where higher Al is broadly interpreted as higher pressures: Wood and Banno, 1973), gives maximum apparent crystallisation pressures of >250 MPa for accompanying amphibole crystallisation (Allan et al., 2017). The close match between the enstatite data presented here and that from Allan et al. (2013) supports the assumption that the melt inclusions targeted in this study are hosted in these inherited cores (Figure 3.2). The negative linear correlation between the melt inclusion SiO_2 contents and the enstatite contents of immediately adjacent orthopyroxene host material suggests that the analysed melt inclusions represent less evolved melt than that held in the pre-eruptive melt-dominant magma body (Figure 3.4). For the purposes of discussion it is thus inferred that the lowest SiO_2 values of the Oruanui melt inclusion population represent the deeper, lesser evolved region of the mush zone, and that the highest SiO_2 inclusions represent the shallowest regions of the mush zone, bordering on the transition to the melt-dominant body. The spread of corresponding host enstatite values between these two inferred end-member compositions therefore represents a population of inherited cores that are inferred to have originated from a variety of

depths within the compositionally stratified mush region. In contrast, the groundmass glass has been inferred to represent the syn-eruptive composition of the melt quenched during evacuation of the melt-dominant magma body (Wilson et al., 2006; Allan et al., 2017). Using all of this information Allan et al. (2017) constructed a schematic cross section of the crust beneath Taupō prior to the Oruanui eruption. Here I reproduce this figure (Figure 4.1) and supplement it with the new information presented in Chapter 3. Information from the post-Oruanui dacite compositions and the Oruanui and post-Oruanui mafic compositions are also included within the figure to show spatial relationships. It is important to note that the post-Oruanui dacites are thought to represent the first magmas erupted from a newly formed, overall less-evolved silicic mush system relative to the Oruanui (Barker et al., 2015).

The Oruanui HSR and post-Oruanui dacite units were targeted for analysis in this study due to their high percentages of inherited cores in major crystalline phases, as noted by previous studies (Charlier et al., 2008; Allan et al., 2013, 2017; Barker et al., 2015). Of the other materials analysed, the post-Oruanui rhyolites have relatively few inherited cores (Figure 3.3). The Oruanui LSR crystals are inferred to have grown in the upper regions of the mush zone (Allan et al., 2017), and do not display the large range in inherited cores as exemplified by the HSR. Thus the following discussion on the deep mush beneath Taupō will focus on the results from the Oruanui HSR, and from the post-Oruanui dacite units.

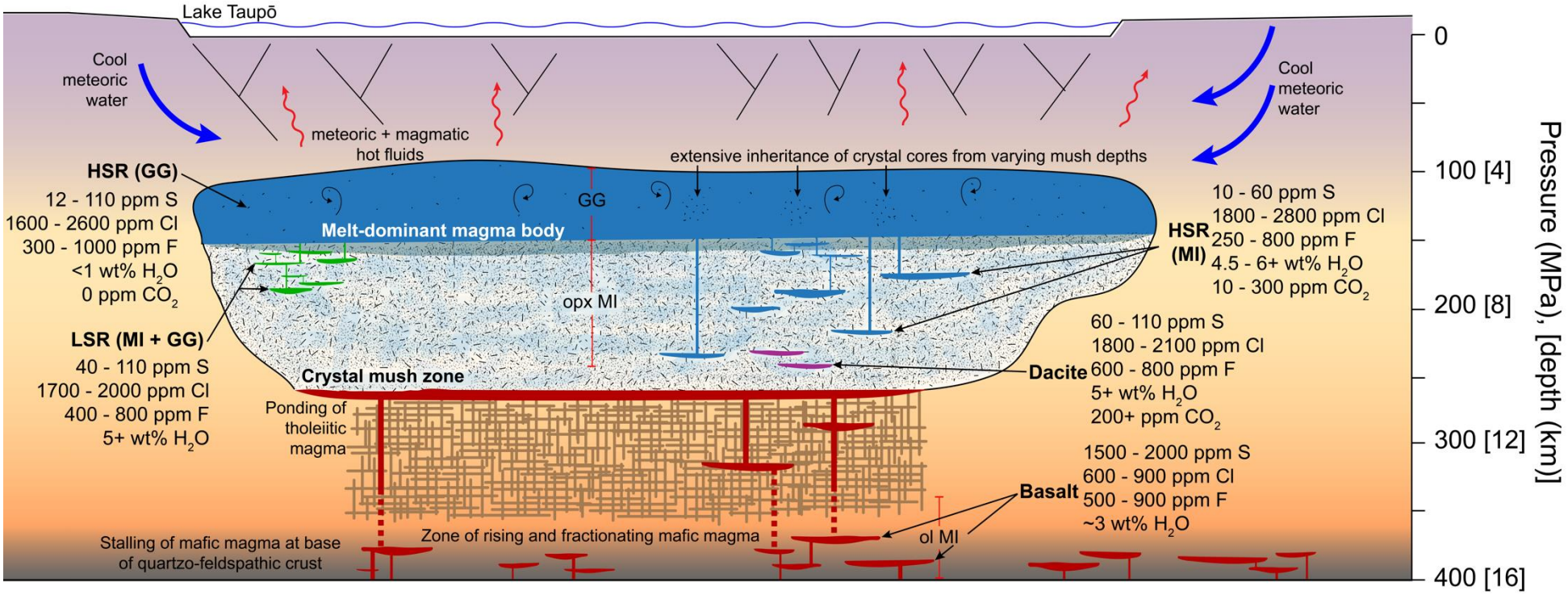

Figure 4. 1. A schematised scaled cross section through the pre-eruptive state of a large silicic magma body in the system beneath Taupō volcano after Allan et al. (2017), (inferred depths of the post-Oruanui dacite magmas are included), displaying the origins and relationships of the key eruptive units (and their inherited crystal cores) studied in this thesis. The values for sulfur, chlorine, and fluorine are detailed for each unit, along with H_2O and CO_2 for the Taupō mafic magmas (Simon Barker, pers. comm, 2019; this study), post-Oruanui dacite (Barker et al., 2015), Oruanui high-silica rhyolite (Liu et al., 2006; Allan et al., 2017; Myers et al., 2018, 2019). HSR = high-silica rhyolite, LSR = low-silica rhyolite, GG = groundmass glass, MI = melt inclusion, opx = orthopyroxene, ol = olivine.

4.2.3 Phosphorous as a proxy for melt evolution

The assumption that the orthopyroxene cores have an origin within the deeper magma system leads to the direct inference that the orthopyroxene-hosted apatites are also derived from the deeper mush region. In direct contrast, the microphenocryst apatite grew and/or equilibrated in the melt-dominant magma body. Apatite is the only phase in Taupō magmatic system to accommodate phosphorous in appreciable amounts, and the P_2O_5 contents of the apatites analysed in this study decrease between the orthopyroxene-hosted apatite inclusions and the microphenocryst apatite in the groundmass (Figure 3.6). It is thus inferred that decreasing P_2O_5 content in apatite crystals serves as a proxy for increasing melt evolution. A compilation of intermediate to rhyolitic whole-rock data from Taupō volcano shows a distinct enrichment-depletion trend for P_2O_5 versus SiO_2 (Figure 4.2). The hinge point at ~58 wt% SiO_2 is here inferred to represent the onset of apatite crystallisation, as apatite is present as both crystal-hosted inclusions and microphenocrysts throughout the silicic eruptive deposits of Taupō volcano (Hervig et al., 1989; Sutton et al., 1995, 2000; Wilson et al., 2006; Gelman et al., 2013; Barker et al., 2015). This inference is supported here by modelling perfect fractional crystallisation of Oruanui basaltic andesite from the Oruanui mafics to dacite (Figure 4.2). The post-Oruanui dacitic whole-rock compositions at maximum P_2O_5 (~0.7 wt%) can be linked with the post-Oruanui dacitic glass compositions by ~50 % fractional crystallisation, with ~3 wt% apatite as part of the total crystalline assemblage. This amount of apatite is reasonable given it is a common accessory phase in Taupō silicic eruptives.

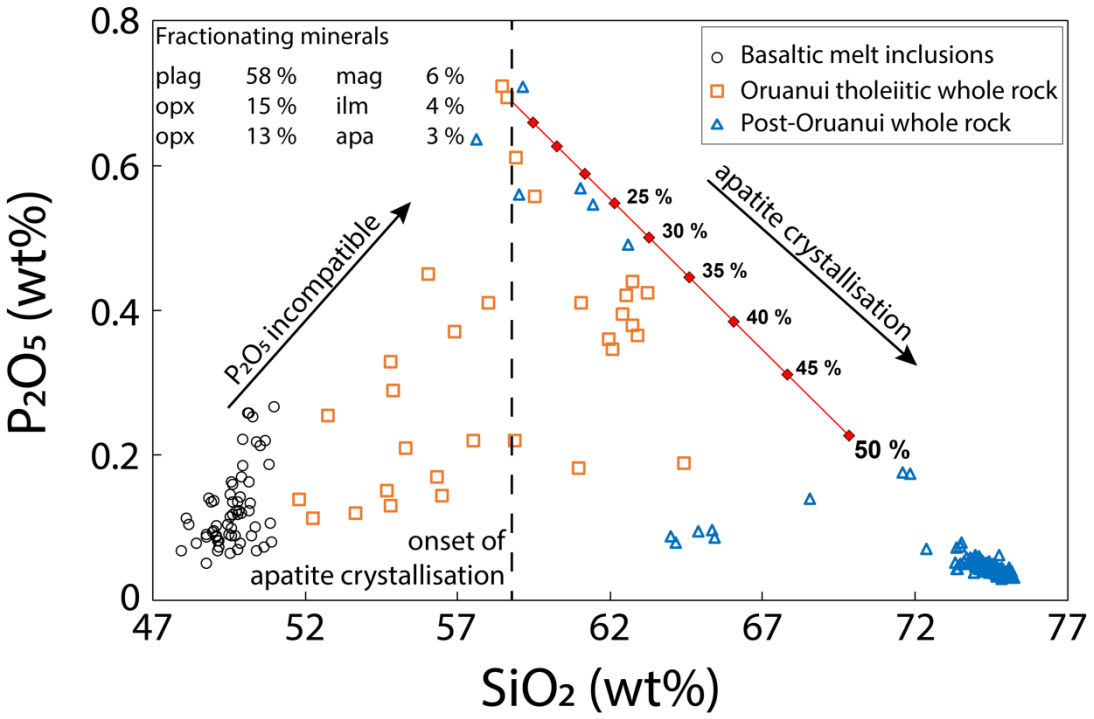

Figure 4. 2. SiO_2 (wt%) versus P_2O_5 (wt%) for Oruanui tholeiitic magma whole-rock (Wilson et al., 2006; Allan et al., 2017; Rooyakkers et al., 2018) and post-Oruanui dacite to rhyolite whole-rock (Barker et al., 2015), with Oruanui basaltic melt inclusions included for reference (Barker et al., manuscript in prep). Solid red arrow represents the potential evolution of Taupō magmas after the peak whole-rock P_2O_5 values of Oruanui tholeiitic magma with perfect, closed system fractional crystallisation increasing in 5 % increments, using the composition of minerals in post-Oruanui dacites with 58 % plagioclase (plag), 15 % orthopyroxene (opx), 13 % clinopyroxene (cpx), 6 % magnetite (mag), 4 % ilemenite (ilm), 3 % apatite (apa). Model performed using PETROMODELER program from Ersoy (2013) with mineral compositions and modal % modified from Barker et al. (2015). See text for discussion.

4.2.4 Vapour saturation

Previous studies on the quartz-hosted H_2O and CO_2 contents of eruptives from Taupō volcano indicate that the melts were saturated in an aqueous vapour phase during the crystallisation of quartz and plagioclase (e.g. Liu et al., 2006; Barker et al., 2015; Myers et al., 2018, 2019). The magmatic storage conditions for which this is inferred are 150 MPa and 800 ˚C, but the depths at which the vapour first exsolved have not been estimated (Allan et al., 2017). The behaviours of sulfur and chlorine in the melt compositions analysed in this study may provide added insight into the magmatic conditions at which the vapour phase may saturate.

4.3 Sulfur

There is a large disparity between the sulfur contents of the basaltic melt inclusions and the silicic melt inclusions analysed in this study (Figure 4.3). Sulfur initially increases with increasing SiO_2 in the basaltic melt compositions up to ~2000 ppm, but dacitic to rhyolitic melt compositions contain <200 ppm sulfur, close to or below the detection limits. This large drop in sulfur during magmatic differentiation is considered here to be due to several key controlling factors. (1) The fractional crystallisation-driven incompatibility of sulfur at basaltic melt compositions initially increases sulfur until it reaches saturation. (2) The crystallisation of a sulfide phase at intermediate compositions may reduce melt sulfur content. (3) The partitioning behaviour of sulfur between a saturated aqueous fluid phase and the silicic melt may also substantially decrease melt sulfur contents. These points are explored further below in the context of sulfur behaviour in magmas and specifically for the compositions observed in the magmatic system beneath Taupō.

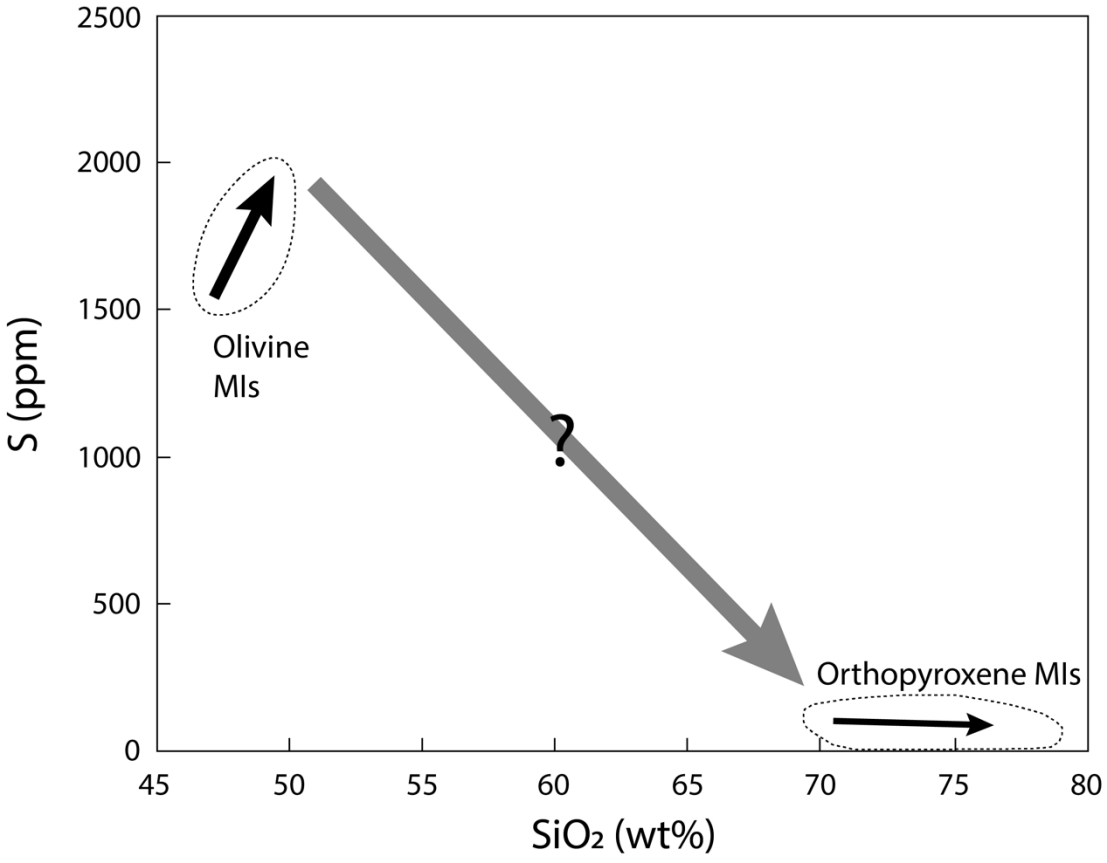

Figure 4. 3. The observed relationships (black arrows) between sulfur (ppm) and SiO_2 (wt%) for the olivine and orthopyroxene melt inclusion (MIs) compositions analysed in this study (general fields delineated by dotted black lines). The grey arrow represents the simplest trend between the end-member compositions.

4.3.1 Magmatic conditions controlling sulfur saturation

The increase in sulfur with relatively constant increasing SiO_2 is inferred to be mainly a function of early stage fractional crystallisation, where sulfur acts as an incompatible element. Melt sulfur concentration is subsequently driven higher through the removal of mafic minerals that do not incorporate sulfur, such as olivine, pyroxene, and plagioclase. However the fact that the sulfur contents of the melt can reach such relatively high values (1000 to 2000 ppm) could also be due to several other factors. The oxygen fugacity (fO_2) and associated oxidation state of a magma exert the strongest control upon the sulfur speciation and content required to saturate a melt (i.e. solubility: Clemente et al., 2004; Behrens and Gaillard, 2006; Baker and Moretti, 2011; Webster and Botcharnikov, 2011). Published models and partitioning coefficients derived from a wide range of experimental and natural data all agree that melt sulfur solubility increases considerably as the fO_2 of a magma increases through the transition from a reduced system (sulfide, S^{2-}, is dominant sulfur ion) to an oxidised system (sulfate, SO_4^{2-}, is dominant sulfur ion: Carroll and Rutherford, 1985, 1987; Jugo et al., 2005b; Zajacz et al., 2012). Typically, this transition occurs near the nickel-nickel oxide (NNO) mineral redox buffer (Webster and Botcharnikov, 2011, and references therein). In addition to the fO_2, temperature and magma composition have both been shown to impose controls on sulfur solubility as a hydrous silicate melt evolves. With increasing melt polymerisation and decreasing temperatures (i.e. a typical magmatic pathway for an ascending magma), the maximum sulfur content required to saturate a silicate melt decreases (Fincham and Richardson, 1954; Wendlandt, 1982; Liu et al., 2007).

The model temperatures and fO_2 of Taupō magmas have been estimated from Fe-Ti oxide pairs (Figure 4.4: Barker et al., 2015; Allan et al., 2017). Relative to the more felsic magmas, the mafic magmas have higher pressures and temperatures (~800 to 900 ˚C and 150 to 250 MPa versus ~1100 ˚C and >300 MPa respectively: Barker et al., 2015; Allan et al., 2017; Simon Barker, pers. comm, 2019), are more oxidised (NNO to NNO + 0.8 versus NNO + 1 respectively: Barker et al., 2015; Allan et al., 2017), and have lower degrees of melt polymerisation (69 to 77 wt% SiO_2 versus ~49 wt% SiO_2 respectively: Table 3.1). Thus it is inferred that the basaltic melt compositions analysed

in this study require a significantly higher sulfur content to saturate the melt relative to the dacitic-rhyolitic melt compositions. The continual sulfur enrichment trend (without any breaks in slope that might indicate sulfide/sulfate growth or fluid phase exsolution) for the basaltic melt compositions suggests that they have yet to reach saturation within the window of SiO_2 contents analysed. This inference is supported by the relatively low H_2O contents of the olivine-hosted melt (average ~3 wt%), and the lack of either sulfide or sulfate phases in the mafic magmas (Rooyakkers et at., 2018; Simon Barker, pers. comm, 2019).

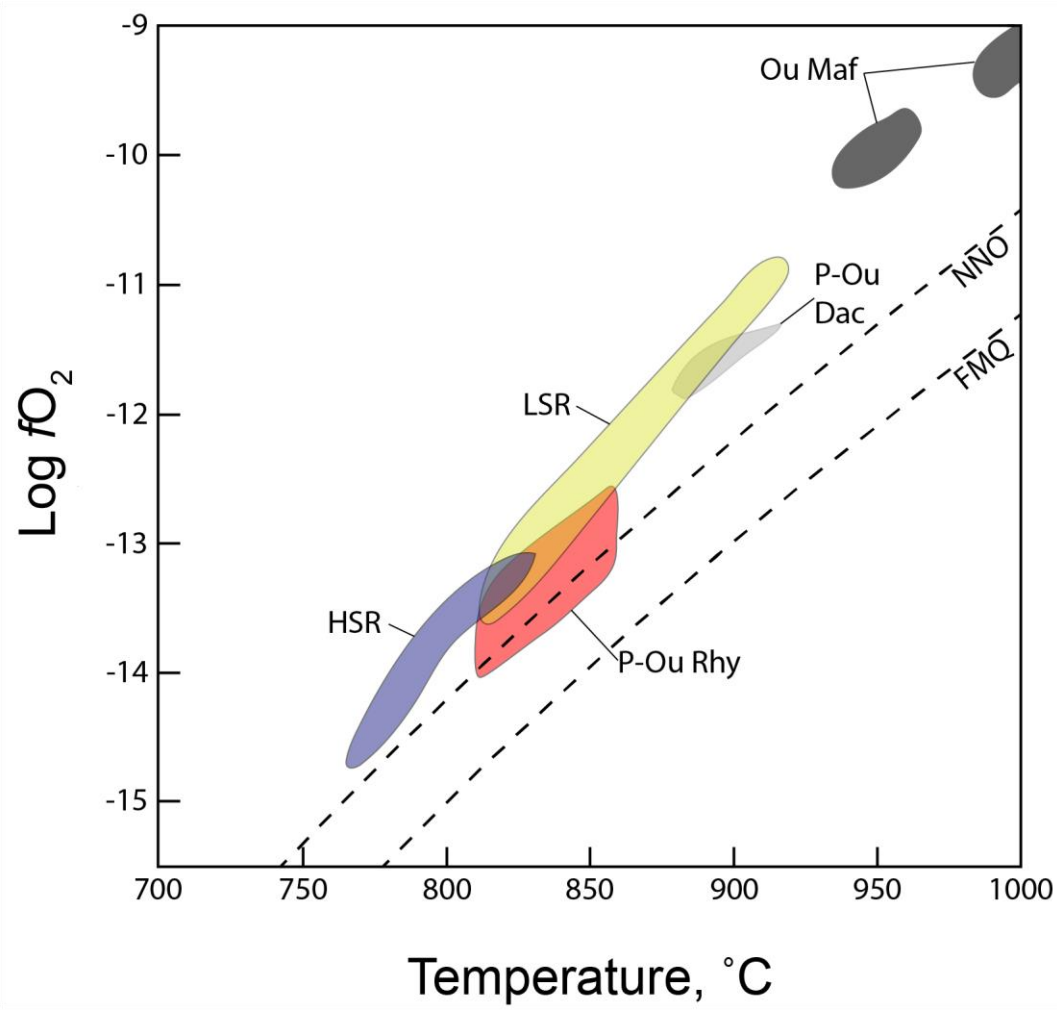

Figure 4. 4. Log fO_2 versus temperature (°C) as calculated by Fe-Ti oxide pairs for Taupō volcano magmas: Oruanui high- and low-silica rhyolite, and more mafic fields (HSR, LSR, Ou Maf respectively: Allan et al., 2017), and post-Oruanui dacite and rhyolite fields (P-Ou Dac and P-Ou Rhy respectively: Barker et al., 2015). Dashed lines labelled NNO and FMQ denote the respective nickel-nickel oxide and fayalite-magnetite-quartz mineral redox buffers.

4.3.2 Sulfide crystallisation

4.3.2.1 Effect of fO_2

The saturation of sulfur in a basaltic melt leads to the exsolution of a non-volatile sulfur-rich phase (SRP e.g. immiscible liquid, sulfate or sulfide: Webster and Botcharnikov, 2011, and references therein). Whether the sulfur is predominantly sulfate or sulfide is determined by the fO_2 of the magma. Although pyrrhotite (sulfide) is observed as inclusions in the post-Oruanui dacite orthopyroxene cores, Taupō basalts have higher oxygen fugacities relative to the silicic compositions (Figure 4.4), and as such are expected to have a higher sulfate/sulfide ratio than the dacites. Regardless of whether the SRP is predominantly sulfate or sulfide, the amount of SRP relative to the silicate melt increases both with decreasing melt sulfur solubility and with fractional crystallisation progresses, as the concentration of sulfur within the SRP is stoichiometrically fixed. If the sulfur is predominantly sulfate, the SRP is expected to be anhydrite ($CaSO_4$) directly crystallising from the melt (Carroll and Rutherford, 1985; Jugo et al., 2005a, 2005b, 2009). In contrast, if the sulfur is predominantly sulfide (and sufficient iron is available), the SRP can either be an immiscible sulfide liquid, or a crystallising sulfide phase (e.g. pyrrhotite: $Fe_{1-X}S$, where X is a stoichiometric coefficient from 0 to 0.2), (Carroll and Rutherford, 1985).

The most significant difference between anhydrite versus sulfide stability is the relative effect each mineral has on the sulfur solubility of a melt. Sulfide saturation depletes the melt ± fluid phase(s) sulfur contents to near minimum values by decreasing melt sulfur solubility considerably, whereas anhydrite crystallisation leads to a relatively high melt sulfur solubility (Carroll and Rutherford, 1985; Scaillet et al., 1998, Clemente et al., 2004; Keppler, 2010). This was shown by Clemente et al. (2004), who investigated the effects on FeO_T and fO_2 on the sulfur content of rhyolite melts at 200 MPa and 800-1000 °C. They found that under relatively reduced conditions (fO_2 <NNO+1, S^{2-} dominant) FeO_T indirectly had a strong effect over melt sulfur content through controlling pyrrhotite stability (Figure 4.5). Under reduced conditions and at FeO_T levels of ~0.5 wt% and below there was not enough iron to support complete crystallisation of pyrrhotite, and melt sulfur levels varied from below detection limits

to ~1800 ppm. However when FeO_T is greater than ~0.5 wt% there was sufficient iron for pyrrhotite crystallisation, which thoroughly depleted all experimental melts in sulfur to levels below 200 ppm, described by an asymptotic relationship (Figure 4.5). Importantly, nearly all experimental runs in which anhydrite was observed (those for which fO_2 > NNO+1) had higher sulfur contents than the runs in which pyrrhotite was stable. This observation is supported by several other studies (e.g. Carroll and Rutherford, 1985, 1987; Luhr, 1990; Jugo et al., 2005a). Superimposing the Taupō silicic melt FeO_T and S data presented in this thesis over that of Clemente et al. (2004) suggests that the Taupō silicic magmas follow the asymptotic relationship described for reduced conditions where there is enough FeO_T to support the saturation of a sulfide phase (Figure 4.5). Additionally, the lack of anhydrite, either as inclusions or phenocrysts, throughout the silicic eruptives from Taupō volcano suggests that the magmas are generally below the fO_2 threshold above which anhydrite is expected to be stable. This inference is supported by the fact that S^{6+} (sulfate) levels measured in Oruanui apatite crystals, whether orthopyroxene-hosted or microphenocrysts, were below detection limits. Sulfate is expected to partition in favour of apatite relative to melt at a ratio of >14 to 1 at relatively low melt sulfur contents in sulfate-dominant system (<1500 ppm: Parat and Holtz, 2005). Thus if the Oruanui magma was oxidised, apatite S^{6+} levels of >1000 ppm would be expected. However, pyrrhotite (sulfide) is only found at trace abundances as inclusions in the major crystalline phases of the relatively deep post-Oruanui dacites. This is likely due to the near detection limit melt sulfur contents, at which levels sulfur is not expected to saturate (Dunbar et al., 1989a; Dunbar and Kyle, 1993; Bégué et al 2015a, 2015b; this study). A possible explanation to the low sulfur content (and associated low pyrrhotite abundances) in silicic melts from Taupō is proposed to be the combined effect of pyrrhotite crystallisation and the exsolution of an aqueous fluid phase. Pyrrhotite crystallisation at intermediate magma compositions is expected to deplete melt sulfur contents to near detection limit values, and exsolution of an aqueous fluid soon after this initial depletion effectively buffers melt sulfur contents below the saturation threshold. This possibility is explored further in the following sections.

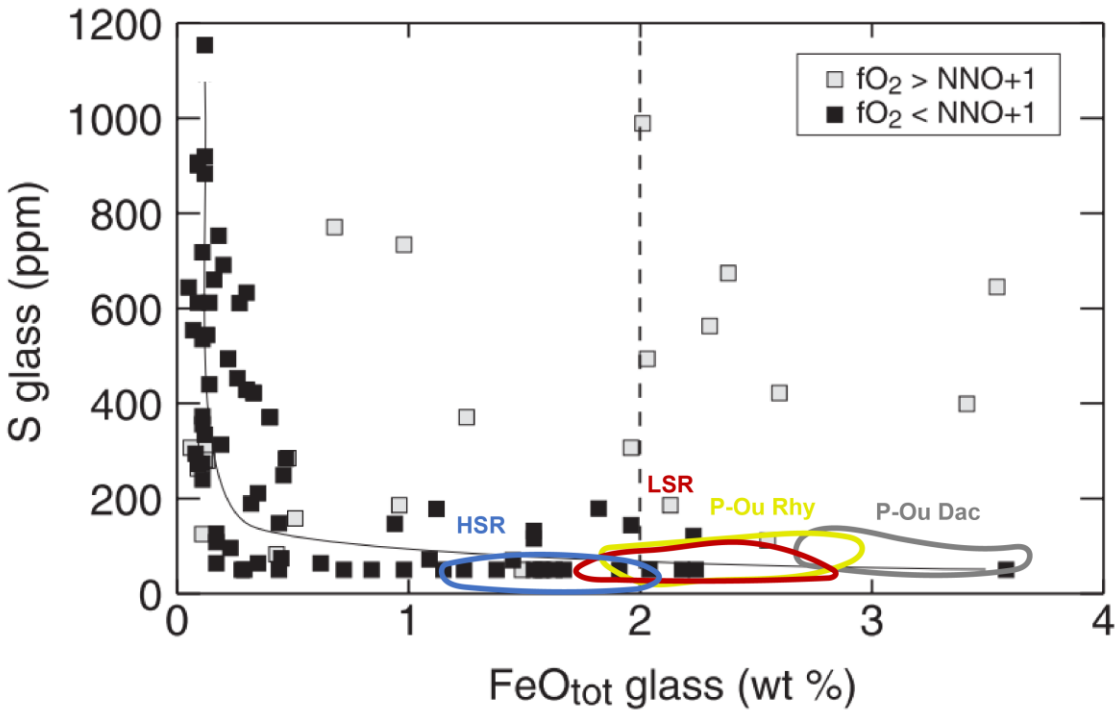

Figure 4. 5. The relationship between sulfur content (ppm) and FeO_T (wt%) of rhyolitic melt at 200 MPa, 800-1000 °C, under relatively reduced (fO_2 <NNO+1: grey squares) and relatively oxidised (fO_2 >NNO+1) conditions. Superimposed coloured lines denote the general compositional fields of Oruanui high- and low-silica rhyolite (HSR = dark blue and LSR = dark red respectively), and post-Oruanui dacite and rhyolite (P-Ou Dac = grey and P-Ou Rhy = yellow respectively). Original figure and data from Clemente et al. (2004).

4.3.2.2 Sulfide depletion event

The sulfur enrichment trend observed in the basaltic melt compositions analysed in this study is inferred to occur due to fractional crystallisation in the absence of an aqueous fluid phase and sulfide/anhydrite (section 4.3.1). There is a broad range in the sulfur content of olivine-hosted melt inclusions in arc basaltic magmas (900 to 7000 ppm: Wallace and Edmonds, 2011, and references therein), but the majority plot between 900 and 2500 ppm (Figure 4.6). This data suggests that the sulfur solubility of basaltic melts is typically ~2500 ppm sulfur content, just greater than the maximum observed sulfur contents of the Taupō basaltic melts (maximum ≈ 2100 ppm: Figure 3.8a). As the majority of arc mafic magmas that feed rhyolite systems have water contents too low for aqueous vapour saturation at deep crustal levels (e.g. Webster, 2004; Shishkina et al., 2010) the most likely cause of this upper limit is exsolution of non-volatile SRPs. Taking this fact into consideration, it is likely that the sulfur contents

of the most evolved (highest SiO_2) basaltic melts of Taupō are nearing saturation, after which a SRP will exsolve. No basaltic-andesitic magmas erupted from Taupō volcano contain sulfide inclusions, but textural studies of intermediate magmas have proposed that sulfide-rich phases are commonly converted to iron oxide minerals, most likely due to the pre-eruptive shallow degassing behaviour of sulfur (Larocque and Stimac, 2000; Wallace and Edmonds, 2011). Thus it is expected that the most likely sources of sulfide in Taupō silicic eruptive deposits will be relict inclusions in the major crystallising phases (e.g. pyrrhotite in the post-Oruanui dacite: Sutton et al., 2000; Gelman et al., 2013; Barker et al., 2015; this study).

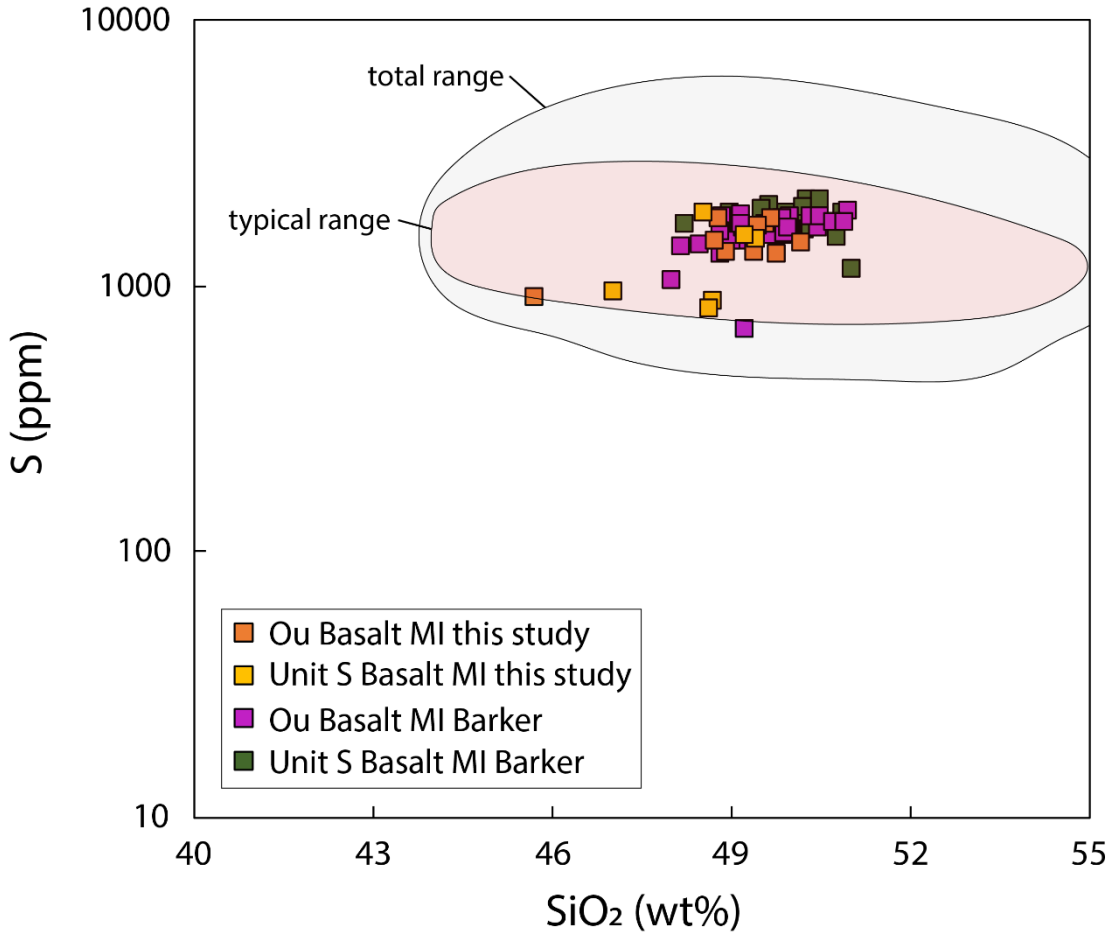

Figure 4. 6. Sulfur (ppm) versus SiO_2 (wt%) for the Taupō volcano olivine-hosted melt inclusions analysed in this study, with the general fields of global olivine-hosted basaltic melt inclusions from convergent margin. The fields are plotted from data sourced from the GeoRoc database. http://georoc.mpch-mainz.gwdg.de/georoc/

A possible explanation for the appearance of trace pyrrhotite in the dacite units is a phenomena often referred to as the magnetite crisis, a term that describes the

apparent correlation between the onset of magnetite crystallisation and a sudden decrease of sulfur and some chalcophile elements relative to increasing melt evolution (Cu, Au, Ag = decrease, Ni, Re, Pt = not affected: Jenner et al., 2010). It has been attributed to the exsolution of Cu-Au hydrosulfide complexes (e.g. Sun et al., 2004), but the fractionation of select chalcophile elements suggests that a sulfide phase crystallises instead (Jenner et al., 2010). The primary control on the saturation of a sulfide phase in both of these studies was inferred to be a decrease in fO_2, triggered by the reduction of Fe^{3+} to Fe^{2+} in the melt as a result of the onset of magnetite crystallisation. SO_4^{2-} was inferred to be the dominant form of sulfur prior to the onset of magnetite crystallisation in the mafic melts investigated by Jenner et al. (2010), the majority of which was converted to S^{2-} during magnetite crystallisation and subsequently sequestered into a crystalline sulfide phase. It is not possible to ascertain whether or not the basaltic-andesitic melt sulfur contents of Taupō volcano are predominantly sulfate or sulfide with the present available data. However, it is inferred that the mafic magmas of Taupō volcano have a higher sulfate/sulfide (SO_4^{2-}/S^{2-}) ratio than the more silicic magmas due to their higher fO_2 (Figure 4.4). Therefore it is suggested that magnetite crystallisation would convert any sulfate in the melt to sulfide, leading to sulfide crystallisation (i.e. pyrrhotite). Constraining whether the pyrrhotite sampled by the post-Oruanui dacites is stable across the whole range of intermediate compositions, or is only stable in specified areas of the system (e.g. magnetite crisis) is challenging, given the lack of melt inclusions representing intermediate compositions. However, whole-rock trends of select major oxides can be used to infer major compositional events which may have run on effects to sulfide growth.

The high compatibility of titanium in magnetite allows its use as a proxy for identifying the magnetite crisis. Initially incompatible in the fractionating crystalline assemblage of the mafic magmas analysed by Jenner et al. (2010), TiO_2 increases with decreasing Mg# (i.e. increasing SiO_2) up until a hinge point at the onset of magnetite crystallisation, after which TiO_2 decreases (~60 wt% SiO_2: Figure 4.7b). This distinct enrichment-depletion trend with increasing magma evolution is also displayed at similar SiO_2 contents (~57 wt% SiO_2) for whole-rock Taupō intermediate-silicic compositions (and the olivine-hosted melt inclusion data for reference: Figure 4.7a).

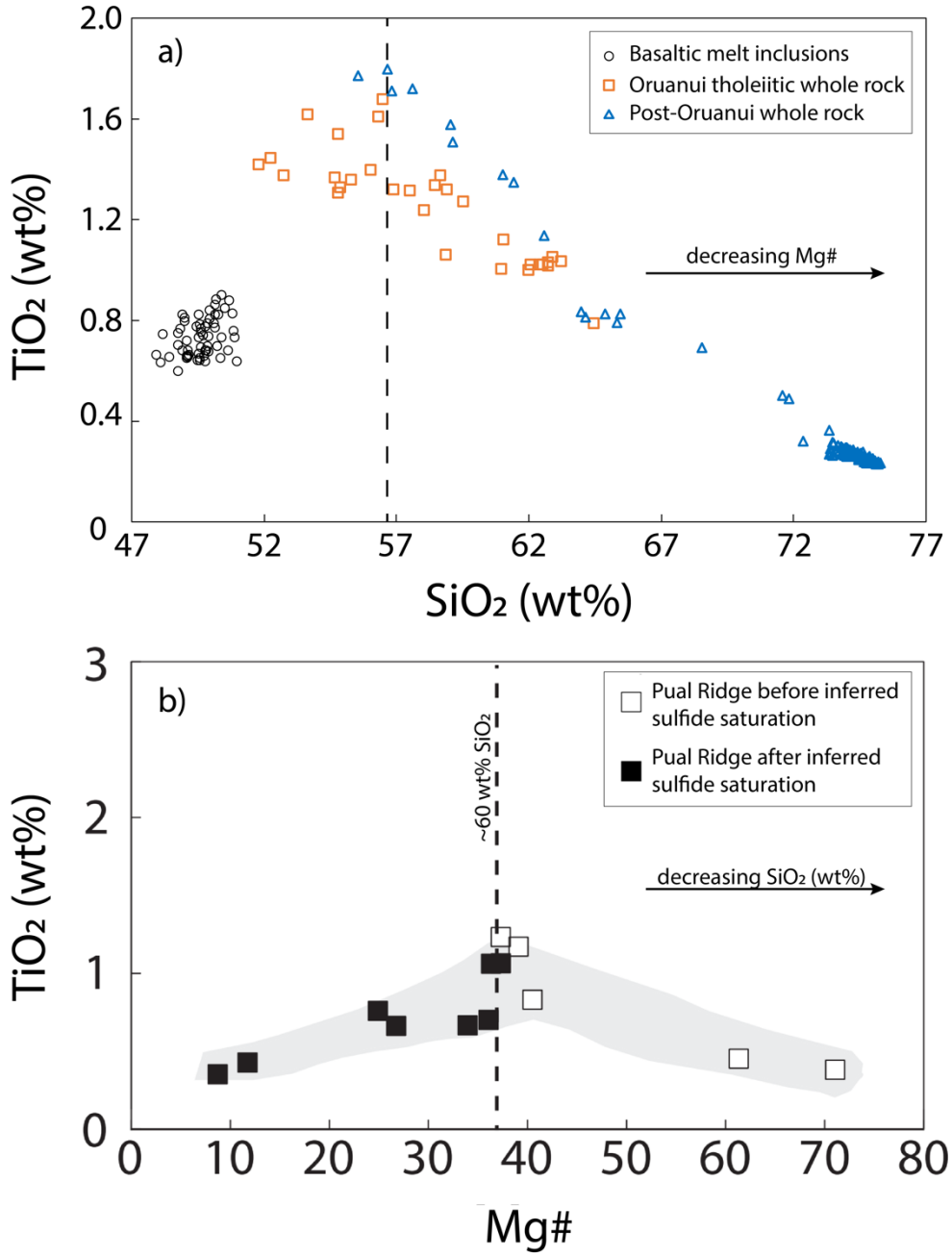

Figure 4. 7. TiO_2 (wt%) versus **a)** SiO_2 (wt%) for whole-rock data and melt inclusion data from Taupō volcano. Data acquired from Wilson et al. (2006), Barker et al. (2015), Simon Barker pers. comm. (2019), and **b)** Mg# for arc-like, relatively oxidised mantle-derived basalt to rhyolite magmas from the Pual Ridge and vicinity, Eastern Manus Basin, with the shaded region emphasizing the liquid line of descent. Dashed lines denote the inferred onset of magnetite crystallisation for each figure. Figure **b)** modified from Jenner et al. (2010).

The use of P_2O_5 as an alternative proxy for the magnetite crisis was also addressed in Jenner et al. (2010). The relationship between P_2O_5 and Mg# of their magmas is similar to that for TiO_2, characterised by a hinge point at ~60 wt% SiO_2 (Figure 4.8b). The Taupō magmas also display this trend, with the hinge occurring at whole-rock ~58 wt% SiO_2 (Figure 4.8a). Magnetite crystallisation appears to trigger apatite crystallisation as well as precipitating sulfides, and apatite has been shown to associate with magnetite

in igneous rocks (Jenner et al., 2010, and references therein). These major element whole-rock trends suggest that the Taupō magmas underwent the onset of magnetite crystallisation at similar stages in their magmatic histories. It is possible that magnetite crystallisation in the Taupō mafic magmas converted any remaining sulfate into sulfide, effectively raising the sulfide content of the melt to above that required for pyrrhotite crystallisation. The subsequent enhanced period of pyrrhotite crystallisation would then significantly deplete melt sulfur content (e.g. to less than 150 ppm: Figure 3.9a).

4.3.3 Saturation of an aqueous vapour phase

Sulfur has been shown to partition strongly into aqueous fluid phases from felsic melt at pressures of ~200 MPa and temperatures of ~800 °C, with recent experimentally determined fluid/melt partition coefficients ($D_S^{fluid/melt}$) varying from ~50 to 470 (e.g. Keppler, 2010; Binder et al., 2018). The strongest control over these partition coefficients is oxygen fugacity, with relatively oxidised melts exhibiting lower $D_S^{fluid/melt}$ values when compared with relatively reduced melts by nearly an order of magnitude at the same pressures and temperatures (Keppler, 2010; Binder et al., 2018). The relatively low (<150 ppm) sulfur contents of the dacite-rhyolite melt compositions (Figure 3.9a) together with the lack of sulfide in the eruptive deposits suggests that sulfur was below the saturation level of the melts. It is inferred that saturation of an aqueous vapour phase (section 4.4.2) kept melt sulfur contents below the threshold for sulfur saturation once pyrrhotite crystallisation had already thoroughly depleted the melt. The vapour is thought to have buffered the sulfur content of the melt at levels less than 150 ppm, inhibiting further pyrrhotite crystallisation. The melt sulfur contents relative to SiO_2 of the least evolved Oruanui high-silica rhyolite and post-Oruanui dacite unit melt inclusions suggests that an aqueous vapour phase had already exsolved prior to trapping of the melt within the orthopyroxene. The highest sulfur contents are present in the post-Oruanui dacite melt inclusions, which then decrease with increasing SiO_2 (Figure 3.9a). The rhyolite melt inclusion sulfur contents from Taupō are lower than those for the dacite (besides a few outliers from Oruanui low-silica rhyolite and post-Oruanui rhyolite), and display no trend with increasing SiO_2 (Figure 3.9a). It is proposed that the exsolution of an aqueous vapour phase was most

likely the main driver for sulfur to decrease from ~150 ppm to a minimum of <60 ppm, below which the sulfur content of the melt is buffered. Applying the partition coefficient of Keppler (2010) derived from a haplogranite ($D_S^{fluid/melt} \approx 50$) of similar major oxide composition to Taupō rhyolite ($SiO_2 \approx 75$ wt%, $Al_2O_3 \approx 11$ wt%, $Na_2O \approx 3.5$ wt%, $K_2O \approx 3.5$ wt%) run at fO_2 of NNO+0.5, 850 °C, and 200 MPa, gives an estimate of 2000 ppm sulfur in the HSR aqueous vapour phase at ~75 wt% SiO_2.

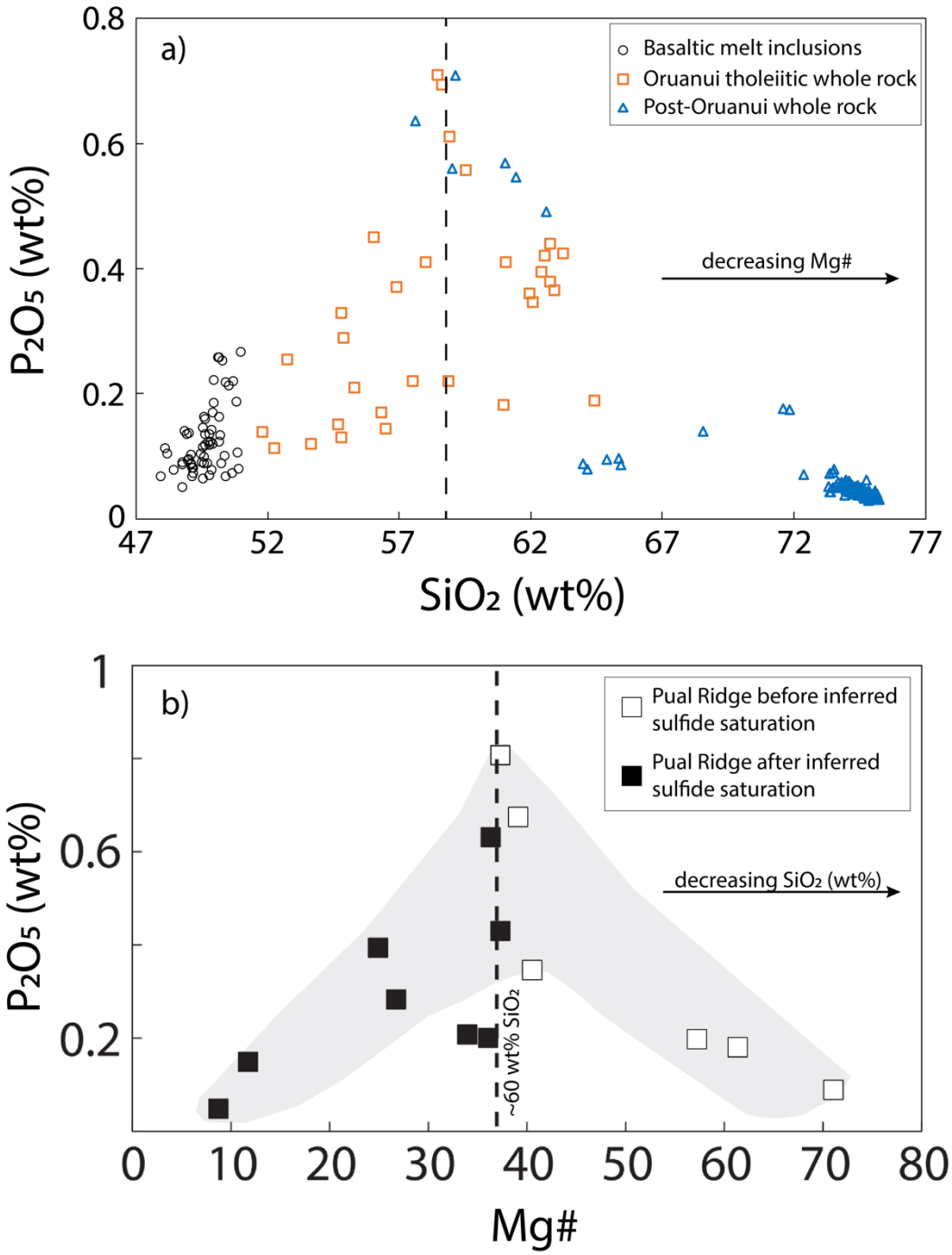

Figure 4. 8. P_2O_5 (wt%) versus **a)** SiO_2 (wt%) for whole-rock data and melt inclusion data from Taupō volcano. Data acquired from Wilson et al. (2006), Barker et al., (2015), Simon Barker pers. comm. (2019), and **b)** Mg# for arc-like, relatively oxidised mantle-derived basalt to rhyolite magmas from the Pual Ridge and vicinity, Eastern Manus Basin, with the shaded region emphasizing the liquid line of descent. Dashed lines denote the inferred onset of magnetite crystallisation for each figure. Figure **b)** modified from Jenner et al. (2010).

4.3.4 The excess sulfur problem

The 232 CE Taupō eruption is not thought to have released a significant amount of sulfur when compared with the largest eruptions of the past 2.5 kyr, despite being the second largest in terms of eruption volume (Sigl et al., 2015). However, the fact that the sulfur signal is identifiable in the ice cores at all contradicts the calculated sulfur emission estimated from melt sulfur content (post-Oruanui rhyolite: Figure 3.8a), which predicts the total sulfur released during the eruption to be <0.004 km^3 (assuming a nominal rhyolite density of 2.3 g/cm^3). Thus it is inferred that there was an excess source of sulfur, besides that held in the melt, that was released during the 232 CE eruption. Application of the sulfur fluid/melt partition coefficients derived from melt compositions and storage conditions similar to those inferred for Oruanui HSR (Keppler, 2010) gives a fluid sulfur concentration of 0.2 wt%. Although this value is orders of magnitude greater than the measured melt sulfur contents, it is still not thought to be significant enough to produce the observed sulfur signals as recorded in ice cores. However, caldera-forming events such as the 232 Taupō eruption significantly disrupt the surrounding country rock, with the potential to release any sulfur sequestered in the hydrothermal envelope around the magma body. Any possible contribution from this type of source is hard to constrain, though, due to the destruction of the hydrothermal envelope. Another possible source for the sulfur signal observed specifically in the 232 CE Taupō eruption, is the intrusion of relatively sulfur-rich mafic material into the overlying silicic system prior to eruption. It has been proposed that up to 5 km^3 of hot (~1100 ˚C) mafic magma was intruded into the mush system below the melt-dominant magma body, driving heating, and large-scale mobilisation of the magma (Barker et al., 2016). Assuming a nominal density of 2.5 g/cm^3 for the mafic magmas and sulfur levels of ~2000 ppm (assuming sulfur depletion had not already occurred: Figure 3.8a), this could supply the overlying silicic system with 0.025 km^3 of sulfur, and thus contribute to the resulting released sulfur flux.

4.3.5 Summary of sulfur transport below Taupō volcano

The inferred behaviour of sulfur with respect to SiO_2 through Taupō magma system is illustrated schematically in Figure 4.9. The high sulfur contents in the basaltic melt inclusions are due to the crystallisation of mafic minerals and the lack of a saturated magmatic fluid phase (e.g. vapour, non-volatile sulfide). Comparison with global sulfur contents of basaltic melt suggests that the basalt melts were near sulfur saturation, inferred to occur within a few weight percent of the highest SiO_2 value. Intersection of the melt sulfur values with the sulfur saturation curve results in the exsolution of a non-volatile sulfur-rich phase (SRP). Beyond this point the gradually decreasing sulfur solubility of the melt leads to an increasing amount of the SRP. Whole-rock SiO_2 contents of ~57 wt% (inferred to represent ~60 to ~65 wt% SiO_2 in the interstitial silicic melt based on minimum whole-rock and melt inclusions SiO_2 values for the post-Oruanui dacites) mark the onset of magnetite crystallisation, which is inferred to lower the fO_2 of the magma, convert the majority of sulfate present in the melt to sulfide, and to trigger a period of pyrrhotite crystallisation. Melt sulfur contents are inferred to be significantly reduced to <200 ppm, and then increase with increasing SiO_2 once pyrrhotite stops crystallising, as the melt is below the threshold for sulfur saturation. Melt sulfur contents may cross the sulfur saturation threshold again, precipitating small amounts of pyrrhotite, but soon after the magnetite crisis it is inferred that an aqueous vapour phase exsolves. Sulfur partitions between melt and aqueous vapour regardless of saturation level, and it is inferred that the presence of a vapour would buffer the sulfur at values below the saturation level of the melt (<150 ppm: Figure 3.9a), and thus inhibit any further sulfide precipitation.

Potential sources for the excess sulfur in the 232 CE caldera-forming Taupō eruption are proposed to be: (1) the sulfur held in an aqueous fluid phase saturated in the melt prior to eruption; (2) the destruction of the hydrothermal envelope surrounding the magma body and subsequent release of any sulfur held in the system; and (3) the addition of sulfur to the silicic magma body from intrusion of 5 km^3 of sulfur-rich mafic material prior to eruption. It is not possible to quantify the amount of sulfur released during the 232 CE eruption from the ice core records. However, the aqueous vapour sulfur contents required to make options one and two viable are most likely far higher

than those estimated here (~0.2 wt%). The flux of sulfur up through the silicic mush system from intruding mafic magmas is considered here to be the largest contributor to the observed sulfur signal. However this option is based on the assumption that any sulfur depletion event had not yet occurred within the intruding mafic magmas. Any potential effect from syn-eruptive degassing of sulfur is inferred to be minimal, due to the near detection limit sulfur contents of both the silicic melt inclusions and the groundmass glass.

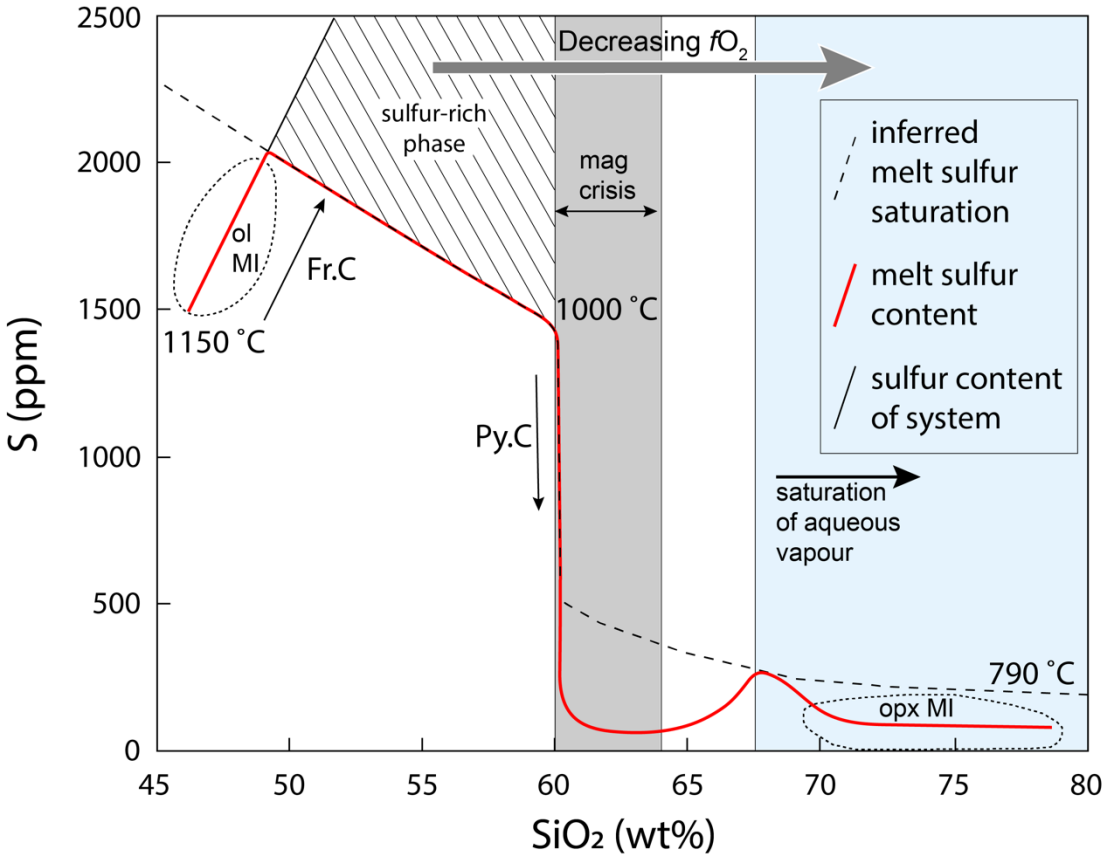

Figure 4. 9. The inferred pathway for sulfur in the melt (red line, ppm) relative to SiO_2 (wt%), between the end-member compositions analysed in this study (see Figure 3.8a for data points: dotted lines = olivine-hosted basaltic melt inclusions [ol MI], and orthopyroxene-hosted dacitic to rhyolitic melt inclusions [opx MI]). Thin black arrows represent the primary control on melt sulfur content at that stage (Fr.C = fractional crystallisation; Py.C = pyrrhotite crystallisation). The inferred curve for sulfur saturation in the melt is denoted by the dashed line. The solid black line illustrates the total sulfur content of the system, with the filled area beneath it (horizontal black lines) representing the increasing amount of sulfur-rich phase relative to the melt. The grey field denotes a potential range of melt SiO_2 content that the magnetite crisis (mag crisis) occurs within (whole-rock ~57 wt% SiO_2). The blue field denotes the saturation of an aqueous vapour phase in the melt. See text for discussion.

4.4 Chlorine

There is an apparent enrichment trend in measured chlorine values between the basaltic melt compositions and the more silicic melt compositions (Figure 4.10). The initial increase in chlorine at basaltic compositions and apparent continual increase across intermediate compositions with increasing SiO_2, and the decrease with increasing SiO_2 at each dacitic to rhyolitic compositional population, are here considered to be controlled by several key factors. In the deep mafic system beneath Taupō, the controlling factors on chlorine are thought to be: (1) the fractional crystallisation-driven incompatibility of chlorine; and (2) the high solubility (relative to typical melt chlorine contents) of chlorine in mafic melts. At silicic compositions, the most important effect is inferred to derive from the partitioning behaviour of chlorine between an exsolving aqueous vapour phase and the melt. These points are explored further below in the context of Taupō magmatic system, along with evaluating the role of apatite in constraining chlorine behaviour in the magmatic system.

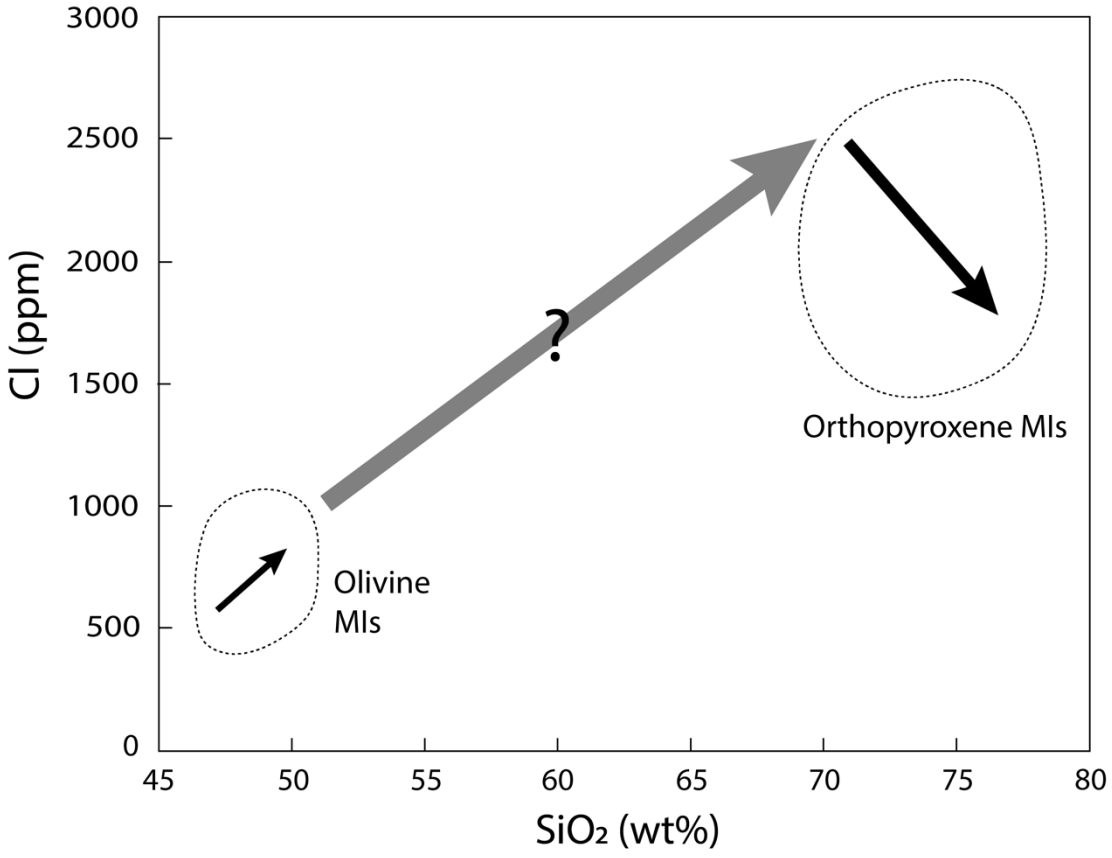

Figure 4. 10. The observed relationships (black arrows) between chlorine (ppm) and SiO_2 (wt%) for the olivine and orthopyroxene melt inclusion (MIs) compositions analysed in this study (general fields delineated by dashed black lines). The grey arrow represents the simplest trend between the end-member compositions.

4.4.1 Chlorine behaviour prior to vapour saturation

4.4.1.1 Chlorine solubility

The relationship between chlorine and H_2O is complicated in silicic magmatic systems, and typically displays non-ideal behaviour (Webster, 2004). Melt chlorine content is sensitive to H_2O at high melt H_2O contents (i.e. once an aqueous vapour phase has exsolved from the melt), but is insensitive at low melt H_2O contents (Webster, 2004). Thus prior to saturation of an aqueous vapour phase in a silicate melt, the water content will have little impact on the melt chlorine content. Instead, melt composition exerts the strongest control in a non-aqueous vapour saturated melt. As silicate melts cool and crystallise, chlorine, which is incompatible in nearly all magmatic minerals due to its large ionic radius (apatite being a notable exception), is expected to concentrate in the melt phase. Thus with crystal fractionation from mafic to felsic magma compositions, the melt will be enriched in chlorine. This behaviour is clearly outlined in a histogram of average chloride contents in melt inclusions of basaltic to rhyolitic compositions, compiled from global magmatic systems (Figure 4.11). The Taupō volcano basaltic and rhyolitic melt chlorine contents overlap with those observed in global magmas of similar composition.

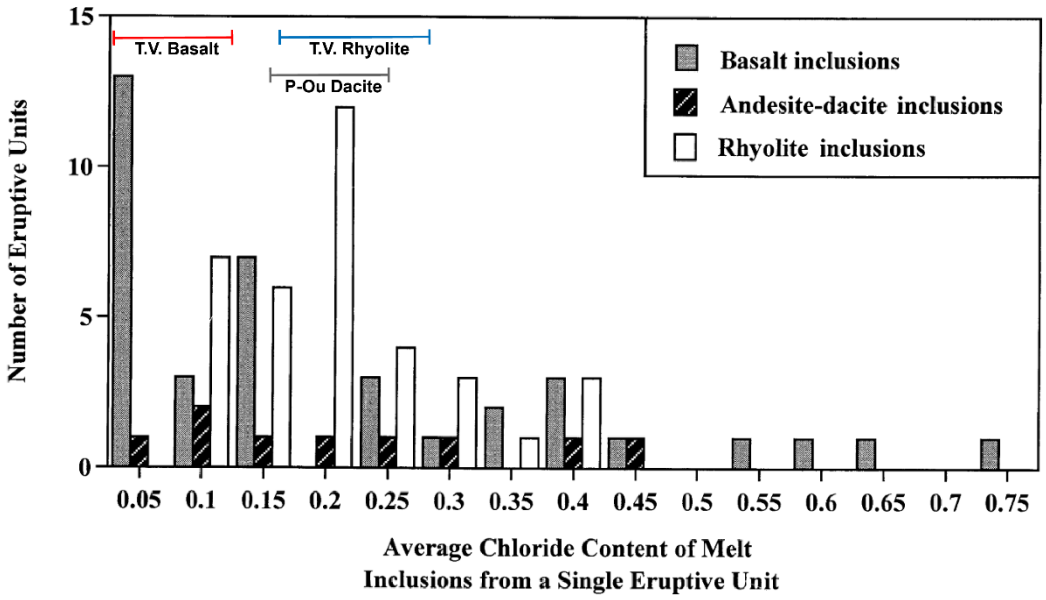

Figure 4. 11. A histogram of average melt inclusion chloride contents from a single eruptive event, in basaltic to rhyolitic melt compositions compiled from global magmatic systems. Capped, coloured lines denote general chlorine contents from Taupō volcano basalt (T.V. Basalt, red), post-Oruanui dacite (P-Ou Dacite, grey), and Taupō volcano rhyolite (T.V. Rhyolite, blue). Modified from Webster et al. (1999).

At basaltic compositions and storage conditions (~51 wt% SiO_2, 1105 °C, 200 MPa, and melt H_2O <5 wt%), experimentally derived data suggest that the saturation content of chlorine in the melt is ~2.7 wt% (Webster, 2004). This value decreases by an order of magnitude down to ~2700 ppm with increasing melt evolution through to rhyolitic compositions and shallower crustal conditions (~75 wt% SiO_2, 760 °C, 50 MPa, and melt H_2O <2.7 wt%: Webster, 2004). As the maximum amount of chloride that can be dissolved in the melt decreases, the chlorine content of a melt increases with fractional crystallisation and decompression. Therefore, in a typical magmatic system (prior to magmatic fluid saturation) chlorine is less likely to reach saturation and exsolve from the melt at less evolved compositions. Chlorine saturation is only expected to occur at evolved rhyolitic compositions, either because an aqueous vapour phase did not esolve, or by a chlorine-bearing aqueous fluid phase reaching the miscibility gap in the system NaCl-H_2O (Lowenstern, 2000).

The initial increase of chlorine in the basaltic melt inclusions can be attributed to the incompatible behaviour of chlorine with respect to the major rock-forming minerals in the Taupō system, and the fact that the chlorine saturation of the melt is likely to be at weight percent values. Plotting the general chlorine versus H_2O fields of the melts from Taupō volcano on Figure 4.12a and 4.12b shows that the Taupō magmas have a low Cl/H_2O value at basaltic compositions, and do not cross the chlorine saturation curve (i.e. melt plus hypersaline liquid curve) at dacitic to rhyolitic compositions. Thus the Taupō melts are inferred to not reach chlorine saturation at any stage during their magmatic evolution, and will increase in concentration in the melt until the saturation of an aqueous vapour phase.

4.4.1.2 Amphibole and apatite

The concentration of chlorine in the amphibole crystals of post-Oruanui rhyolites (units B, C, D, E) is ≤2000 ppm, less than that of the melt (Barker, 2014; this study). As amphibole typically only makes up <2 wt% of the crystal cargo of Taupō silicic eruptive deposits, it is inferred to have very little effect on melt chlorine abundances (Liu et al., 2006; Barker et al., 2015). However, yttrium (Y, where decreasing values are inferred to represent amphibole crystallisation) plotted against chlorine does reveal opposite

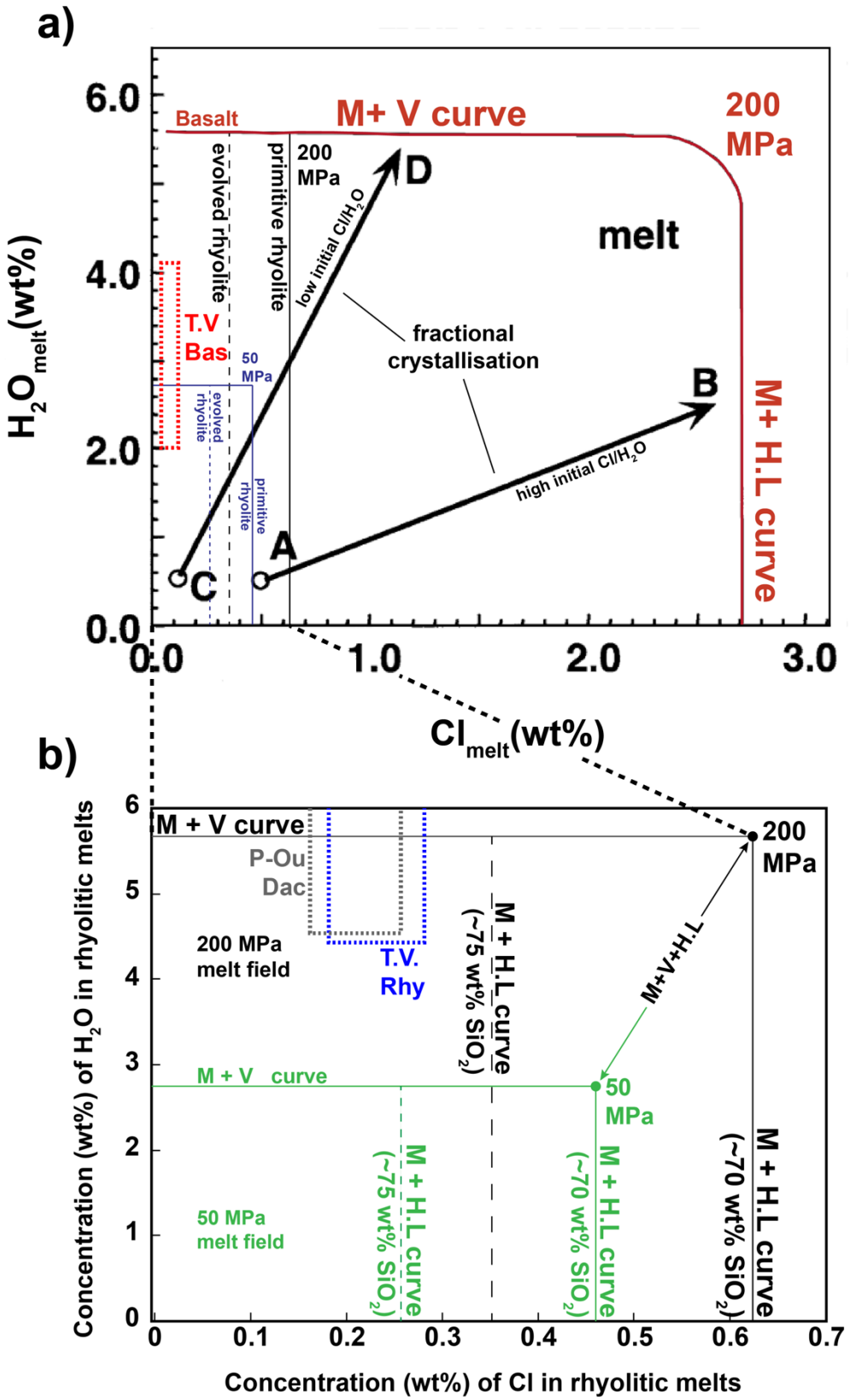
a)
6.0
4.0
2.0
0.0
0.0
1.0
2.0
3.0
H_2O_{melt}(wt%)
Cl_{melt}(wt%)
Basalt
M+ V curve
200 MPa
melt
M+ H.L curve
evolved rhyolite
primitive rhyolite
200 MPa
D
low initial Cl/H_2O
fractional crystallisation
high initial Cl/H_2O
B
A
C
T.V Bas
50 MPa
evolved rhyolite
primitive rhyolite
b)
Concentration (wt%) of H_2O in rhyolitic melts
Concentration (wt%) of Cl in rhyolitic melts
M + V curve
P-Ou Dac
T.V. Rhy
200 MPa melt field
M + H.L curve (~75 wt% SiO_2)
M+V+H.L
200 MPa
M + V curve
50 MPa
50 MPa melt field
M + H.L curve (~75 wt% SiO_2)
M + H.L curve (~70 wt% SiO_2)
M + H.L curve (~70 wt% SiO_2)

▲ **Figure 4. 12.** Experimentally- and naturally-derived curves describing the relationship between the solubilities of chlorine (wt%) and H_2O (wt%) in different silicate melt compositions at different pressures. **a)** the dark red curve (labelled with red text) is derived from basaltic compositions at 200 MPa and ~1105 °C. Arrow A→B illustrates how a melt with high initial Cl/H_2O can evolve to produce a hypersaline brine phase, and arrows C→D illustrate how a melt with low initial Cl/H_2O can evolve to produce a H_2O-rich vapour phase. The thin black and blue curves are plotted for reference, and are expanded and explained in **b**, as indicated by the external dashed lines. The Taupō volcano mafic compositional field is denoted by the dotted red box (T.V. Bas). **b)** The solid vertical lines represent a more primitive silicic composition (~70 wt% SiO_2) and the dashed vertical lines represent a more evolved silicic composition (~75 wt% SiO_2) at differing pressures and temperatures as labelled by the respective black and green labels. Melt composition has a negligible effect on H_2O solubility, so the solid horizontal lines represent both the more primitive and evolved felsic melts. The Taupō volcano felsic compositional fields are denoted by the dotted grey and blue lines (Post-Oruanui dacite and Taupō volcano rhyolite respectively). For both **a)** and **b)** vertical curves describe the melt (M) plus hypersaline liquid (H.L) stability fields, and horizontal curves describe the melt plus hydrous vapour (V) stability fields. **a)** Modified from Mathez and Webster (2005); **b)** modified from Webster et al. (2017).

trends between the amphibole-bearing and the amphibole-absent eruptives studied here (Figure 3.10). The decrease in chlorine with increasing Y in the amphibole-bearing units is contradictory to that expected, as amphibole breakdown (increasing Y) would be expected to release chlorine into the melt. This leads to the assumption that any effect of amphibole crystallisation is negated by a different process that exerts a stronger control over melt chlorine concentrations.

The concentration of chlorine in the Oruanui apatite analysed in this study varies from 0.8 to 1.5 wt% (Figure 3.6b). Apatite chlorine contents are an order of magnitude greater than the chlorine contents measured in the silicic melt. However the trace abundances of apatite are thought to limit the impact it can have on melt chlorine contents. Although apatite crystallisation is expected to decrease the rate of chlorine enrichment very slightly, it is inferred that apatite does not exert the strongest control over melt chlorine contents as it is a minor fractionating phase. These inferences are supported by estimating the amount of chlorine enrichment in the melt from mafic to silicic compositions. Perfect fractional crystallisation between basaltic and dacitic compositions (~65 % crystallisation: Simon Barker, pers. comm, 2019) without the influences of either apatite or amphibole predict chlorine contents of ~2300 ppm in the dacite melt. The chlorine contents measured in the dacitic melt inclusions and presented in this study exhibit a range from ~1800 to ~2400 ppm. Thus the effects of both apatite and amphibole are thought to be minimal.

4.4.2 Saturation of an aqueous vapour phase

Numerous studies investigating the partitioning of chlorine have concluded that chlorine is strongly partitioned into the fluid phase (if available) relative to the melt at all natural magmatic compositions (Baker and Alletti, 2012, and references therein). Partition coefficients (fluid/melt) vary from ~10 to ~350 (e.g. Kravchuk and Keppler, 1994; Signorelli and Carroll, 2000, and references therein; Webster et al., 2009; Doherty et al., 2014), with the highest coefficients typically occurring in cooler, lower pressure, silica-rich melts (i.e. dacite to rhyolite compositions). The primary control on whether an aqueous vapour phase or a hypersaline brine phase will exsolve is in the H_2O/Cl ratio of the melts (Webster, 2004). Plotting the inferred H_2O/Cl fields of melts from Taupō volcano on an experimentally determined chlorine versus H_2O curve supports the inference that the basaltic melts are not expected to exsolve either an aqueous vapour or a brine phase (Figure 4.12a), and that the silicic melts are expected to exsolve an aqueous vapour phase rather than a chlorine-rich brine (Figure 4.12b).

Estimating how deep an aqueous vapour phase may be saturated within the magmatic system below Taupō volcano is challenging. The quartz-hosted melt inclusion CO_2 values used by Liu et al. (2006) (maximum ≈ 300 ppm) are inferred to represent the top region of the crystal mush zone at which rhyolite compositions were evolved enough for quartz to crystallise (Allan et al., 2013, 2017). Plagioclase-hosted melt inclusion CO_2 values in dacite compositions recorded by Barker et al. (2015) were <50 ppm, inferred to reflect leakage during ascent and decompression. As CO_2 solubility is strongly correlated with pressure, melts stored at higher pressures are expected to have higher CO_2 levels (Lowenstern, 2000). The orthopyroxene core-hosted melt inclusions analysed in this study are inferred to have come from significantly deeper in the crystal mush system than the inferred pressure above which quartz is stable (140 to 250+ MPa versus 100 to 170 MPa: Liu et al., 2006; Allan et al., 2017). Thus the CO_2 contents of the melt hosted in the orthopyroxene cores should exceed the maximum reported values for the quartz-hosted melt. Applying this knowledge to the Oruanui HSR melt compositions inferred to represent the deep mush system, a depth of vapour saturation using the VolatileCalc 2.0 program (a revised version of VolatileCalc: Newman and Lowenstern, 2002), gives ~310 MPa for maximum inferred temperatures

and volatile contents (H_2O = 6.5 wt%, CO_2 = 400 ppm, T = 950 ˚C: Liu et al., 2006; Barker et al., 2015; Allan et al., 2017). Minimum inferred temperatures and volatile contents give a depth of vapour saturation at ~180 MPa (H_2O = 4.5 wt%, CO_2 = 300 ppm, T = 850 ˚C: Liu et al., 2006; Barker et al., 2015; Allan et al., 2017). The majority of HSR (and post-Oruanui dacite) melt inclusions analysed in this thesis are inferred to plot between these end-member vapour saturation pressure estimates, and as such it is reasonable to infer that a vapour phase may be saturated to pressures exceeding 250 MPa beneath Taupō volcano (Figure 4.13). It is important to note that Figure 4.13 is calibrated for a rhyolite at 800 ˚C, which is near the minimum model temperatures for the HSR in the shallow melt-dominant magma body (Allan et al., 2017). The deep mush-derived orthopyroxene cores are more likely to represent temperatures >900 ˚C, and higher temperatures lead to a greater depth of vapour saturation (Newman and Lowenstern, 2002).

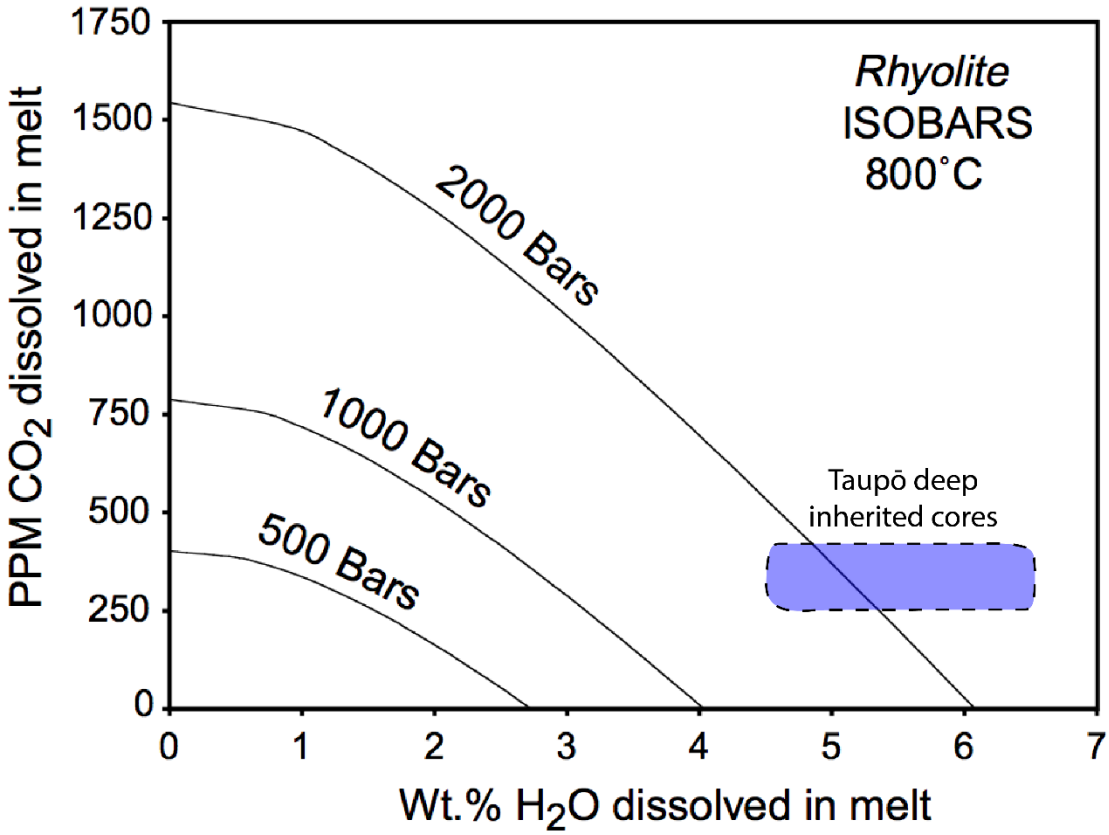

Figure 4. 13. Isobars plotted relative to H_2O (wt%) and CO_2 (ppm) contents dissolved in a melt, predicting the depth at which a H_2O=CO_2 vapour will exsolve at 800 ˚C, as determined by the program VolatileCalc (Newman and Lowenstern, 2002). The inferred range in volatile compositions for the deepest inherited crystal cores from silicic eruptive deposits of Taupō volcano is denoted by the blue field within the dashed black line, although the deep cores from Taupō magmas are inferred to have equilibrated at temperatures exceeding 900 ˚C (Barker et al., 2015; Allan et al., 2017). Volatile estimates are based off results published by Liu et al. (2006), Barker et al. (2015), Allan et al. (2017), Myers et al. (2018, 2019). Figure modified from Newman and Lowenstern (2002).

The decrease in chlorine with increasing $SiO_{2=}$ in both the Oruanui HSR and post-Oruanui dacite melt compositions of Taupō volcano is consistent with strong partitioning of chlorine into an aqueous vapour at a range of depths within the mush zone (Figure 3.9b). Although the sulfur concentrations exhibit for of a constant trend with increasing SiO_2, this is primarily inferred to represent the buffering of already-depleted sulfur values by an magmatic fluid phase (section 4.2.4). The vapour appears to have saturated prior to the least evolved melt inclusion SiO_2 contents of each compositional population. This is plausible given the estimated pressures of vapour saturation as calculated with VolatileCalc. If the constant decrease in chlorine is due to partitioning into a saturated vapour phase, then the behaviour of chlorine may be a useful indicator for the presence of a vapour phase at high pressures (>200 MPa) within a magma system for HSR and post-Oruanui dacite. The chlorine contents of the melt inclusions analysed here are inferred to be representative of the melt with which they last equilibrated with prior to entrapment, whereas CO_2 has a propensity to leak (e.g. Barker et al., 2015).

The shallowest regions of the Oruanui melt-dominant magma body are inferred to be in equilibrium with H_2O-CO_2 vapour at pressures and temperatures less than 150 MPa and 800 °C (Liu et al., 2006; Allan et al., 2017). These conditions are less than those required for the separation of an aqueous vapour phase into a discrete vapour phase and a discrete brine (e.g. Chou, 1987). However work by Charlier et al. (2012) suggests that the immiscibility curve was not reached until syn-eruptive decompression at 22 MPa during the evacuation of the Oruanui magma. Thus it is inferred that the only phase by which melt chlorine contents are fractionated by is an aqueous vapour phase. This inference is corroborated by application of a chlorine solubility model published by Webster et al. (2015) to the Taupō melt compositions. The model was derived from hydrothermal experiments on basaltic to rhyolitic systems, with pressures and temperatures varying from 0.1 to 700 MPa and 700 to 1250 °C, and as such the authors state it is applicable to a large range of natural magma compositions and conditions. Applying the model to the least and most evolved HSR melt compositions gives chlorine solubility maximum (CSM) estimates of 0.59 and 0.56 wt% respectively. These solubility levels are roughly double the recorded chlorine contents of the melts measured here and published by Dunbar et al. (1989a), Hervig et al. (1989), Dunbar

and Kyle (1993), and Bégué et al. (2015a, 2015b, 2017). Applying the model to the least and most evolved dacite melt compositions gives CSM estimates of 1.13 and 0.89 wt% respectively, again significantly higher than the recorded chlorine contents, which precludes the saturation of a chlorine-rich brine.

4.4.3 The role of apatite crystallisation

4.4.3.1 Broad changes in volatile behaviour

The maximum chlorine contents of apatite hosted in HSR orthopyroxene cores analysed in this study are ~1.3 wt% (Figure 3.6b). As apatite is only present at trace abundances in the eruptive deposits of Taupō volcano, it is unlikely to exert any significant control on the overall chlorine contents of the magma system. However the use of apatite in assessing changes in volatile behaviour throughout a magma system has been effectively demonstrated (e.g. Zhu and Sverjensky, 1991; Mathez and Webster, 2005; Webster et al., 2009, 2017; Doherty et al., 2014; Scott et al., 2015; Stock et al., 2018). One such example is to use the Cl/F ratio of apatite in identifying the type of magmatic fluid phase saturated in the melt. Decreasing Cl/F ratios have been proposed to indicate the saturation of an aqueous vapour phase with the magma, into which chlorine is strongly partitioned relative to melt, whereas fluorine prefers the melt (e.g. Candela, 1986). The Cl/F ratio in the Oruanui HSR apatites decrease from the orthopyroxene-hosted apatite to the microphenocryst apatite (Figure 3.6c). This could support the inference of a vapour phase saturated within the melt. However decreasing Cl/F ratios has also been attributed to a decrease in temperature (Piccoli and Candela, 2002).

Assessing whether or not magmatic fluid is escaping the system or not is another way in which apatite composition can be used to infer broad volatile processes. In a system with melt, apatite, and a saturated magmatic fluid, if the chlorine content of both apatite and the melt is decreasing with increasing magmatic evolution, it is inferred that the chlorine contents of the system as a whole are decreasing i.e. the fluid phase is exiting the system (Doherty et al., 2014). The chlorine content of both the Oruanui

apatite and HSR melt is shown to decrease with increasing SiO_2 content, which may suggest that the aqueous vapour phase was escaping from the mush system (Figure 3.6b; Figure 3.9b). The biggest proportion of the water discharged in the geothermal systems of the TVZ is meteoric in origin (Giggenbach, 1995). Maximum chlorine contents in waters in the TVZ geothermal wells are ~2500 ppm (Giggenbach, 1995), and studies have proposed that 6 to 20 vol% of the geochemical signature of geothermal fluids could be contributed by magmatic vapour (Giggenbach, 1995; Christenson et al., 2002; Bernal et al., 2014).

4.4.3.2 Estimating chlorine in magmatic fluids and melt

The use of apatite in estimating the chlorine contents of other magmatic phases, such as melt and magmatic vapour, has been demonstrated in many studies (e.g. Zhu and Sverjensky, 1991; Mathez and Webster, 2005; Webster et al., 2017; Doherty et al., 2014; Scott et al., 2015; Stock et al., 2018). One such examples is an experimental study published by Webster et al. (2009) investigating the partitioning of chlorine between apatite and melt under similar conditions to those inferred for Taupō magmas (dacitic to low-silica rhyolite compositions in equilibrium with a magmatic vapour phase, 200 MPa, 900 to 924 °C, and NNO to NNO+2.1). The authors reported apatite/melt partition coefficient ($D_{Cl}^{apatite/melt}$) values between 1 and 4.5, with the highest occurring with the most felsic melts. The least and most evolved HSR apatite analyses (inferred from P_2O_5 values: section 4.2.3) plot near the authors' data points for a rhyolite melt with a similar chlorine solubility maximum as estimated for the Oruanui magma in section 4.4.2 (CSM = 0.58: Figure 4.14). Application of their highest partition coefficient (4.5) to the both orthopyroxene-hosted and microphenocryst apatite gives slightly higher chlorine melt estimates than those measured for the melt inclusions, and slightly lower for the groundmass glass (Figure 4.15). These estimated melt chlorine values are in agreement with the measured chlorine melt contents for both the orthopyroxene-hosted and groundmass-derived analyses, albeit slightly too high and low respectively. This slight discrepancy has been observed in the original and subsequent studies (e.g. Webster et al., 2009; Scott et al., 2015). The most likely cause of the differences is that the experimental conditions from which the partition

coefficients were derived were set at 200 MPa, whereas the samples from the HSR are inferred to represent melt compositions from 90 to >250 MPa (Allan et al., 2017). The fact that the groundmass-derived estimates are higher than those measured in the melt, and that some of the orthopyroxene-hosted estimates (deepest pressures) are greater than those measured in the melt suggests that there is an influence from the differing pressures.

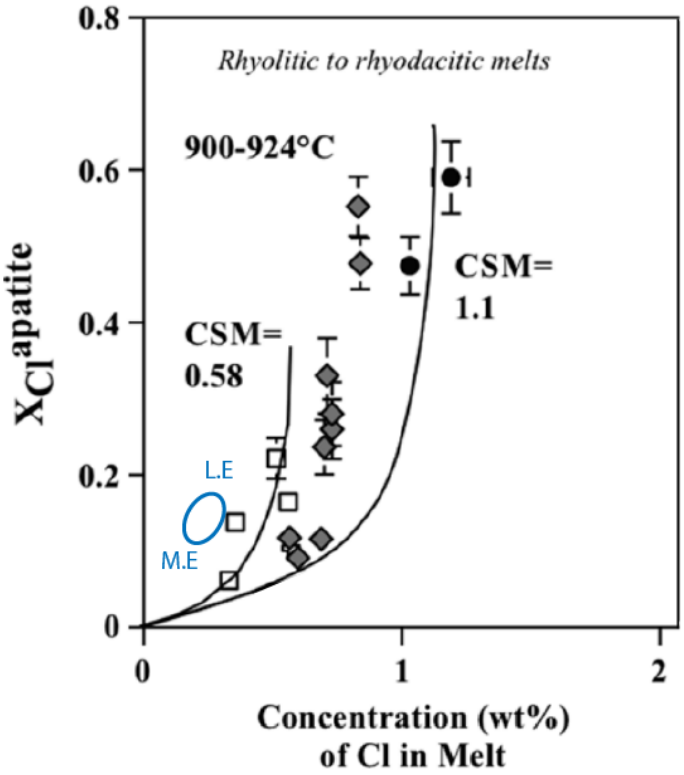

Figure 4. 14. Plot showing the relationship between chlorine in apatite (mol fraction) versus chlorine in rhyolitic and rhyodacitic melts (wt%), with respective chlorine solubility maximums (CSM) of 0.58 and 1.1. Data from Oruanui apatite presented in this study is plotted with a blue as a general field (see Figure 3.6b for data), L.E and M.E are least evolved and most evolved respectively. Modified from Webster et al. (2009).

Webster et al. (2009) also published a model to calculate the partitioning of chlorine between apatite and exsolving magmatic fluids. The good agreement between the previously estimated melt chlorine contents from apatite compositions and those directly measured from melt inclusions gives confidence in applying their fluid/apatite model to the Taupō data. The partitioning of chlorine between apatite and aqueous vapour is thought to be relatively straightforward. The following model describes a positive linear relationship between the chlorine content of apatite (mol fraction) and

magmatic fluids (weight percent), and was derived from experiments on rhyodacites to low-silica rhyolites at ca. 200 MPa and ~900 °C (Webster et al., 2009):

$$X_{Cl}^{apatite} = 0.011\ x\ (wt\%\ Cl\ in\ fluid[s])$$

Application of this model to Oruanui HSR apatite data gives average aqueous vapour chlorine contents of 12.7 and 10.0 wt% from the orthopyroxene-hosted and microphenocryst apatites respectively, giving a single $D_{Cl}^{fluid/apatite}$ value of ~11. However this value is notably high for the expected concentration of chlorine in an aqueous vapour phase. It is possible that the slightly lower concentration of chlorine in the melt for Oruanui HSR relative to the experimental data (Figure 4.15) leads to erroneously high fluid chlorine concentrations.

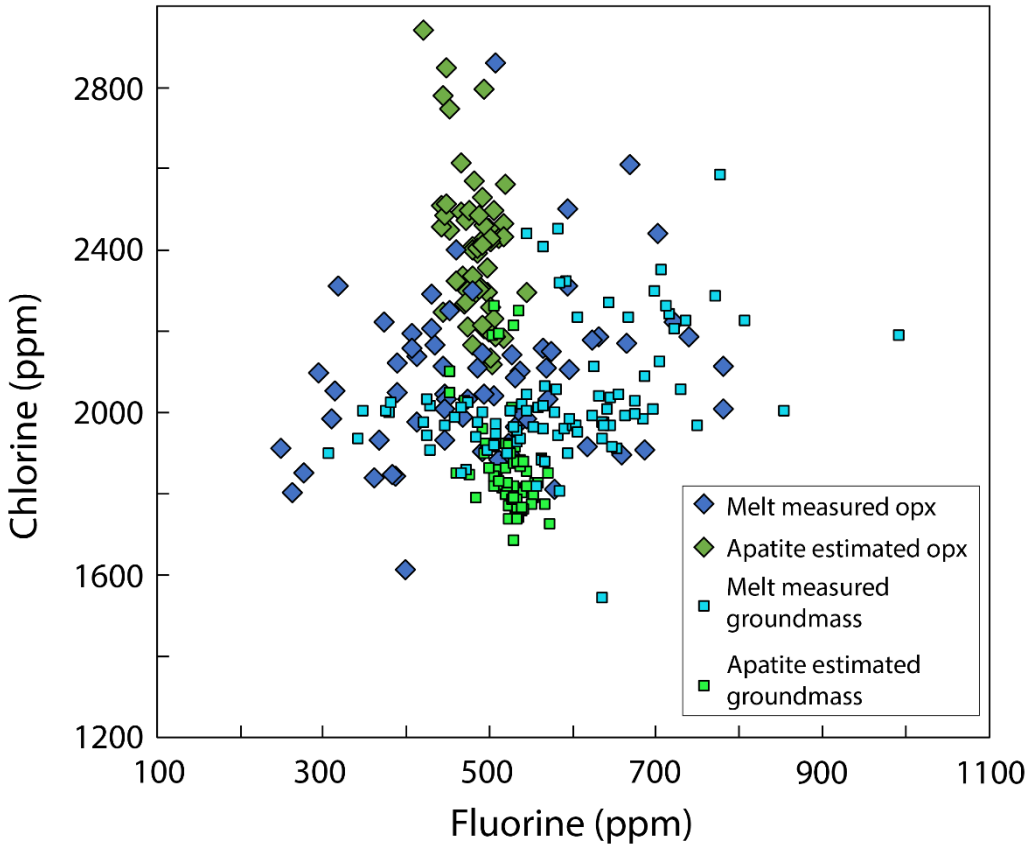

Figure 4. 15. The relationship between fluorine (ppm) and chlorine (ppm) for measured orthopyroxene hosted melt inclusions (Melt measured opx) and groundmass glass (Melt measured groundmass), and for estimated melt compositions from orthopyroxene-hosted apatite (Apatite estimated opx) and microphenocryst apatite (Apatite estimated groundmass) using the model of Webster et al. (2009).

4.4.4 Summary of chlorine transport below Taupō volcano

The inferred transport of chlorine with respect to SiO_2 through the magmatic system beneath Taupō is illustrated schematically in Figure 4.16. The relatively low chlorine content of the basaltic melt inclusions is indicative of the initial chlorine content of the primitive magmas prior to extensive crystallisation. The enrichment trend from basaltic to dacitic melt compositions is inferred to be steady due to the gradual removal of the mafic minerals and increase in the SiO_2 content of the melt. Chlorine is incompatible in all crystallising phases apart from apatite (and to a minor extent amphibole). However neither of these phases contain enough amphibole or occur at high enough abundances to have an impact of melt chlorine levels. At silicic melt compositions inferred to be a few weight percent lower SiO_2 than the least evolved dacitic melt inclusions, an aqueous vapour phase saturates within the melt. Chlorine partitions strongly into the exsolving vapour phase over the melt, which therefore leads to a strong depletion of chlorine in the melt as the amount of exsolved vapour increases with decompression. As melt evolution progresses, the fluid/melt partitioning coefficient increases steadily. The loss of chlorine in both apatite and melt may be indicative of the exsolving vapour phase exiting the system, supplying the nearby hydrothermal system. The clustering of the chlorine in groundmass glass analyses at the lowest respective HSR and post-Oruanui rhyolite melt inclusion chlorine content analyses suggest that little syn-eruptive degassing of chlorine occurred. In contrast, the lower chlorine concentrations of the dacite groundmass relative to the melt inclusions suggests that some syn-eruptive degassing occurred.

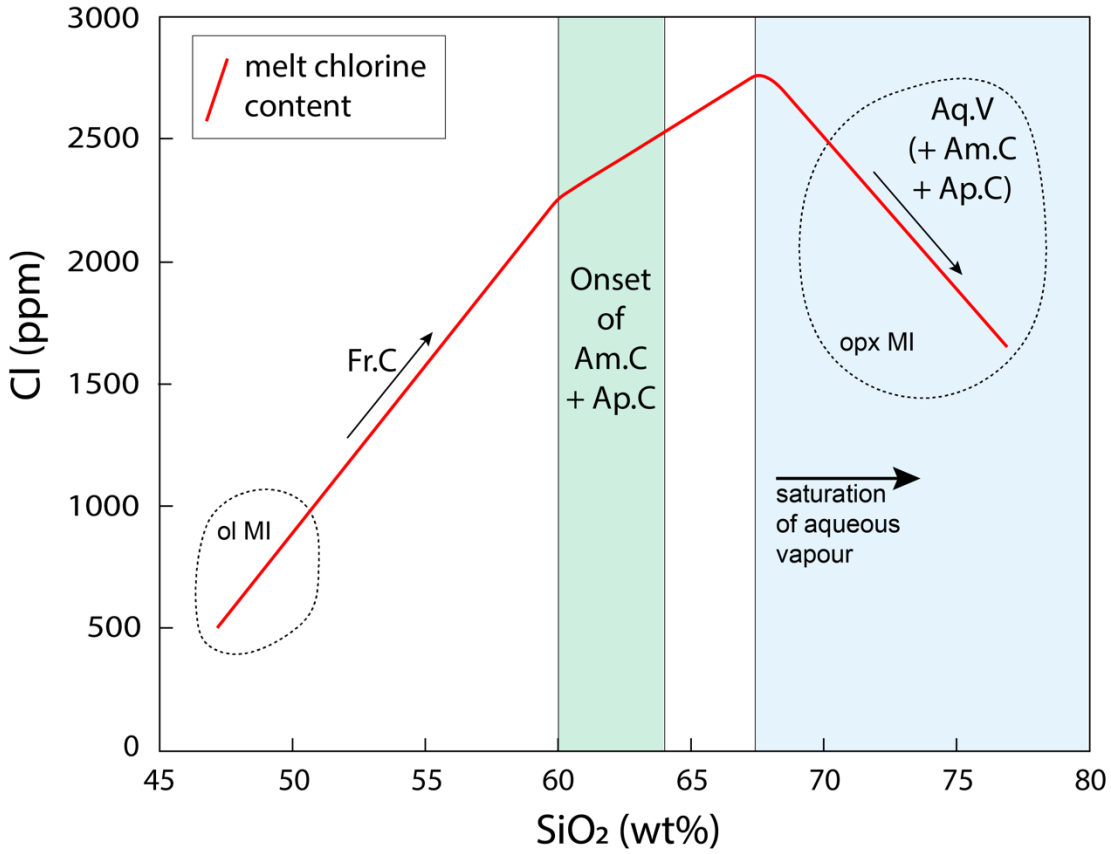

Figure 4. 16. The inferred pathway for chlorine in the melt (red line, ppm) relative to SiO_2 (wt%), between the end-member compositions analysed in this study (see Figure 3.8b for data points: dotted lines = olivine-hosted basaltic melt inclusions [ol MI], and orthopyroxene-hosted dacitic to rhyolitic melt inclusions [opx MI]). Thin black arrows represent the primary control on melt chlorine content at that stage (Fr.C = fractional crystallisation; Aq.V = aqueous vapour saturation; Am.C = amphibole crystallisation; Ap.C = apatite crystallisation). The green field denotes a potential range of melt SiO_2 content that amphibole and apatite might begin to crystallise (apatite at whole-rock ~58 wt% SiO_2). The blue field denotes the saturation of an aqueous vapour phase in the melt. See text for discussion.

4.5 Fluorine

The behaviour exhibited by fluorine in the magmas of Taupō volcano is hard to interpret. Similarities in the range and value of fluorine melt inclusion analyses between the basaltic and silicic compositions do not allow for broad inferences such as the respective depletion and enrichment of sulfur and chlorine as melt evolution progresses. However, as fluorine is expected to favour the melt over an exsolving magmatic fluid, the major fluorine-bearing phases in the Taupō system that are inferred to exert significant controls over melt fluorine contents are amphibole and apatite. Amphibole is not present in the post-Oruanui units analysed here besides Unit

C, for which there are few data points. With these considerations in mind, the following discussion considers possible explanations for the observed trends, but with less confidence than the behaviours described for sulfur and chlorine in the previous discussions.

The fluorine contents of the basaltic melts increase with increasing SiO_2 (Figure 4.17). At some stage in the compositionally intermediate region of the Taupō magmas this trend is thought to be interrupted, as melt fluorine concentrations are ~500 ppm in the dacitic to low-silica rhyolitic melt inclusions, before appearing to increase again at melt SiO_2 contents >76 wt% in the HSR. These inferred trends are proposed to stem from three key factors: (1) The high solubilities of fluorine in silicate magmas and the fractional crystallisation-driven incompatibility of fluorine; (2) the crystallisation of hydrous minerals (chiefly amphibole in the amphibole-bearing magmas, and apatite in the amphibole-absent magmas); and (3) the subsequent destabilisation of amphibole in the more evolved, SiO_2-rich region of the HSR magma. These points are explored further below in the context of Taupō magmatic system, along with assessing the use of apatite as an indicator mineral for constraining the behaviour of fluorine in the magmatic system.

4.5.1 Fluorine solubility in silicate melts

Fluorine has a high solubility in silicate melts relative to other volatile components (e.g. sulfur and chlorine), due to the ease with which fluoride substitutes for oxygen through similarities in ionic radii (London et al., 1988; Piccoli and Candela, 2002; Mathez and Webster, 2005; Dolejš and Baker, 2007; Aiuppa et al., 2009; Webster et al., 2009, 2017; Doherty et al., 2014). This characteristic makes it very uncommon for fluorine to saturate within a melt. Fluorine is also not expected to partition in favour of aqueous vapour relative to melt until melt fluorine concentrations exceed several weight percent (e.g. Webster, 1990; Webster and Holloway, 1990; Dolejš and Baker, 2007). Thus in basaltic magmas, fluorine is expected to become progressively enriched in the melt through fractional crystallisation processes. However, the crystallisation of

hydrous phases at intermediate melt compositions is proposed to interrupt this enrichment trend.

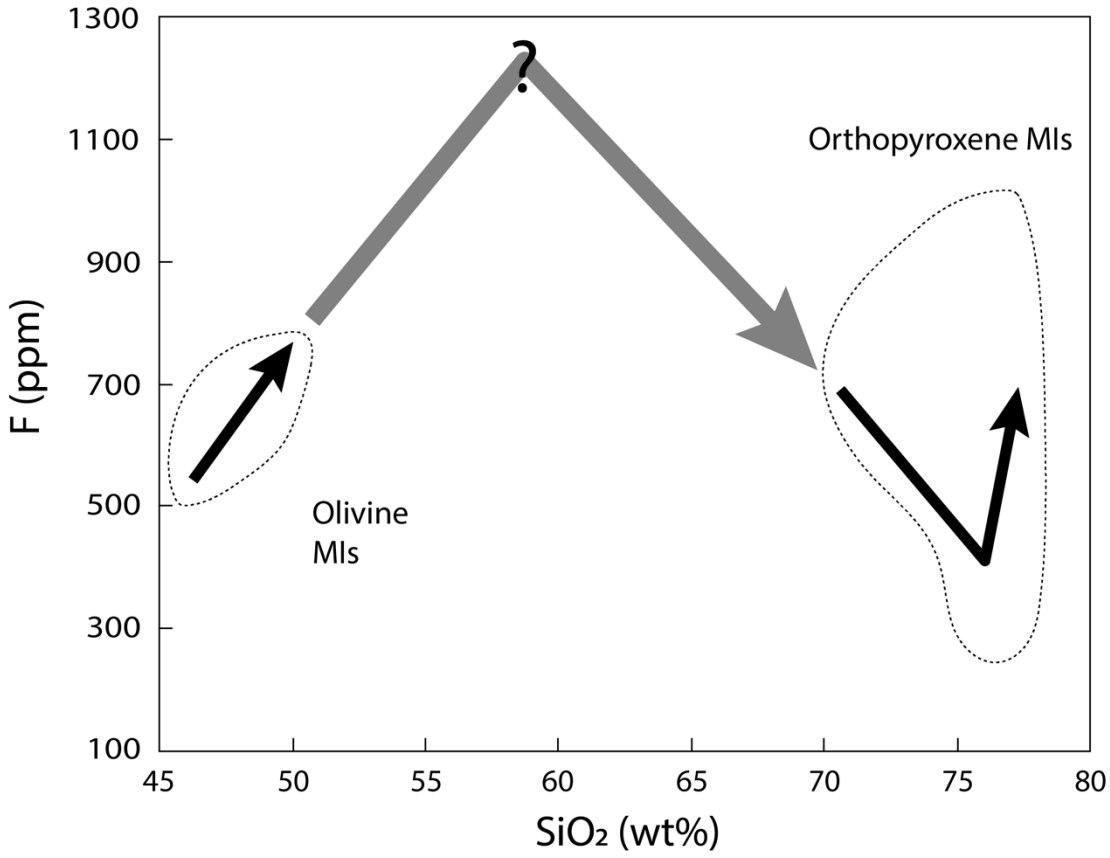

Figure 4. 17. The observed relationships (black lines) between fluorine (ppm) and SiO_2 (wt%) for the olivine and orthopyroxene melt inclusion (MIs) compositions analysed in this study (general fields delineated by dashed black lines). The thick grey arrow represents the simplest trend between the end-member compositions.

4.5.2 The role of amphibole

There have been very few studies on the fluorine content of magmatic amphibole, but it has been known to incorporate fluorine to weight percent levels (Ekstrom, 1972; Chambefort et al., 2013; Van den Bleeken and Koga, 2015). This is largely due to the similarity in the sizes of the F^- and OH^-/O^{2-}ions (1.33, 1.37, and 1.40 Å respectively: Dolejš and Zajacz, 2018). The fluorine concentration of Taupō amphibole has not yet been recorded, but the data presented in this thesis suggests that it may hold significant quantities of fluorine, and is the major fluorine-bearing phase in the amphibole-bearing magmas of Taupō. Although amphibole only makes up 1 to 2 wt%

of the crystalline cargo in the studied eruptive deposits, the high levels of crystallisation (>70 %) and extent of the crystal-rich must be kept in mind (Liu et al., 2006 Barker et al., 2015; Allan et al., 2017). Previous studies on the Oruanui HSR have proposed depths of apparent amphibole crystallisation at pressures >250 MPa, but the base of the mush system is inferred to extend to greater depths (Allan et al., 2013, 2017). There is an apparent hinge point when fluorine is plotted against SiO_2 in the Oruanui compositions at approximately 76 to 77 wt% SiO_2 (Figure 4.18). Fluorine appears to decrease in the LSR, and then appears to increase in the HSR. It is possible that this approximate transition represents the edge of the amphibole stability field, where the LSR magmas are within the amphibole stability field and fluorine is accommodated by crystallising amphibole. In contrast, the HSR magmas may approach or cross the border that defines amphibole stability, leading to a pause in amphibole crystallisation (or even resorption). The melt fluorine contents would then be free to increase with increasing SiO_2. This possible transition from the amphibole stability field could occur do to the differences in factors such as temperature and water content between the magma compositions.

Previous textural work on Oruanui amphibole crystals has suggested that relatively high-silica clasts (whole-rock >76.5 wt% SiO_2) left the amphibole stability field in the most evolved parcels of magma in the melt-dominant body, as evidenced by resorption of amphibole (Allan et al., 2013). The fluorine contents of several HSR groundmass glass samples with SiO_2 >77 wt% exhibit slightly elevated levels relative to the rest of the groundmass population (Figure 4.18). It is suggested that these anomalous points may represent the parcels of most evolved melt, in which amphibole resorption would release fluorine back into the melt.

The control that amphibole is inferred to exert on fluorine is also supported by melt inclusion trace element data. Yttrium (Y) is plotted against fluorine in Figure 3.10, for both the amphibole-bearing and amphibole-absent eruptives analysed in this study. Fluorine decreases with decreasing Y for the amphibole-bearing compositions. Amphibole crystallisation has been shown to deplete Y in the melt with increasing melt evolution in Taupō melts (Barker et al., 2015; Allan et al., 2017). The positive correlation between fluorine and Y for the amphibole-bearing magmas suggests that

fluorine decreases with amphibole crystallisation. In contrast, there are no discernible trends between fluorine and Y for the amphibole-absent compositions.

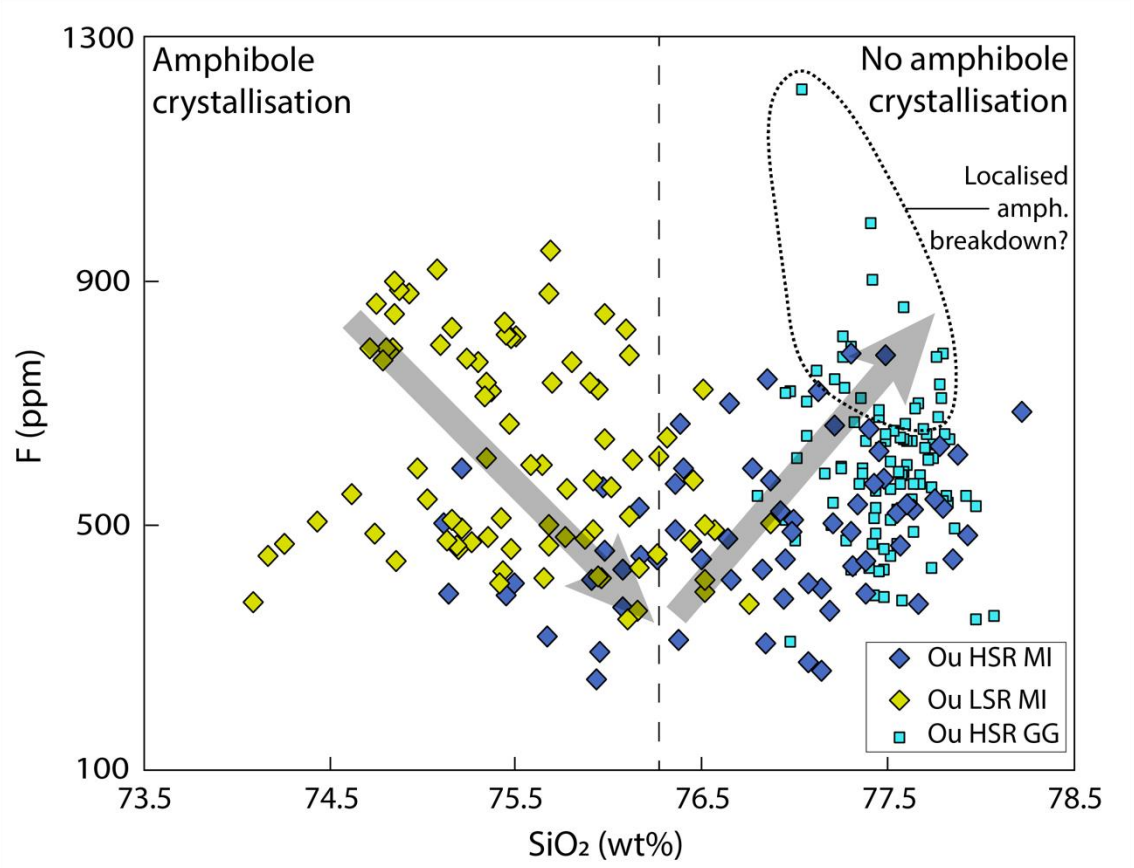

Figure 4. 18. The opposing trends in the relationship between fluorine (ppm) and SiO_2 (wt%) for melt inclusions in the Oruanui low-silica rhyolite (Ou LSR MI) and the Oruanui high-silica rhyolite (Ou HSR MI). The grey arrows represent the inferred control exerted by amphibole stability, with the dashed line denoting the approximate SiO_2 content at which amphibole becomes unstable in the Oruanui system. The black dotted lines denote a possible area of localised significant amphibole breakdown in HSR groundmass glass (GG) compositions.

4.5.3 Apatite as an indicator mineral

The average fluorine content of Oruanui microphenocryst apatite is approximately 2 wt% (Figure 3.6a). Although modelling the amount of apatite crystallisation in the Oruanui magmas suggests that apatite may contribute up to 3 wt% of the mush zone crystal cargo (section 4.2.3), apatite is only present as a trace mineral in the Oruanui eruptive deposits, and as such is not inferred to have a large control over total melt fluorine contents in the Oruanui compositions. However, the decrease in melt fluorine with increasing SiO_2 in the post-Oruanui dacite and rhyolite units is thought to be

associated with apatite crystallisation. The concentrations of apatite in these units were not analysed here, but the lack of any other fluorine-bearing phase in the magmas suggests that apatite exerts the primary control.

4.5.3.1 Volatile elements

The potential of using apatite to track changes in melt fluorine contents is long established, and fluorine has been shown to favourably partition into apatite relative to silicic melt (Candela, 1986; Piccoli and Candela, 2002; Mathez and Webster, 2005; Webster et al., 2009, 2017; Marks et al., 2012; Doherty et al., 2014; Scott et al., 2015). A study on the partition coefficient of fluorine between apatite and melt, with similar experimental conditions to those in the Taupō melts (dacitic to low-silica rhyolite compositions in equilibrium with a magmatic vapour phase, 200 MPa, 900 to 924 °C, and NNO to NNO+2.1: Webster et al., 2009), reported that the mol fraction of fluorine in apatite (X_F^{ap}) increases with an increasing fluorine (and decreasing chlorine) content of the melt. The calculated partition coefficients from their data range from ~13 to ~37, with the highest coefficients correlated with the most evolved samples. Application of this coefficient to the Oruanui HSR apatite compositions closely matches the average measured melt content of both the orthopyroxene-hosted and groundmass-derived melt analyses (Figure 4.15). However there is a significantly larger range in the direct fluorine measurements of both the orthopyroxene-hosted and groundmass-derived melt analyses. Three possible reasons for this difference are suggested here. (1) The melt inclusions were hosted in orthopyroxene cores that sampled a greater range of pressures within the magmatic system than the smaller sample size of orthopyroxene-hosted apatite. (2) The errors involved with measuring apatite in the melt, apatite, or both, produce non-representative results. (3) The model was calculated at a stable pressure of 200 MPa. Of these possibilities, it is inferred here that the single pressure of 200 MPa under which the experiments of Webster et al. (2009) were conducted is thought to cause the observed differences. The Oruanui HSR melt compositions from groundmass glass and orthopyroxene-hosted inclusions are thought to represent melt ranging from pressures of 90 to >250 MPa, nearly ± 100 MPa either side of the pressure from which the model was derived.

4.5.3.2 Trace elements

Through its ability to accommodate nearly half the periodic table, apatite has great potential for use in geochemical studies that include trace element analyses (Sha and Chappell, 1999; Piccoli and Candela, 2002; Belousova et al., 2001, 2002). However the selected trace elements plotted against chlorine and fluorine presented in Figure 3.11 do not exhibit the trends generally expected for each respective element. The zirconium (Zr) content of apatite increases with increasing melt evolution, which contrasts with the decreasing Zr content of the melt, driven primarily by zircon crystallisation (Allan et al., 2017). In addition, the europium (Eu) trends observed in the analysed apatite are similar to those for Zr, in that Eu increases with increasing melt evolution. Again this trend is opposite to melt compositions, which become steadily depleted in Eu as SiO_2 increases due to the crystallisation of feldspar (Allan et al., 2017). Lanthanum (La), a typically incompatible element expected to enrich in silicic melt with increasing evolution, decreases in apatite with increasing melt evolution. The most probable explanation for these contradictory trends is thought to be the anomalous behaviour of CaO in the Oruanui apatite. The relationship between CaO and P_2O_5 is tightly constrained, but with two suites of similar CaO values and differing P_2O_5 values describing each of the orthopyroxene-hosted apatite and microphenocryst apatite populations (Figure 3.6d). The cause behind this distinct relationship is inferred to be the ease with which available divalent cations substitute for calcium.

4.5.5 Summary of fluorine transport below Taupō volcano

Discerning the dominant controls on the behaviour of fluorine below Taupō volcano is challenging. The observed trends are hard to interpret, and although amphibole and apatite appear to be the two most likely fluorine-bearing phases in the magma system, the data is not convincing. Keeping these considerations in mind, the following interpretations lead to a potential magmatic pathway for fluorine, as displayed schematically in Figure 4.19. The increasing fluorine values relative to SiO_2 in the basaltic melt compositions are inferred to be due to the fractional crystallisation of non-hydrous minerals, enriching the melt in fluorine. Without any compositionally

intermediate melt inclusions it is not possible to constrain the onset of amphibole and apatite crystallisation to an exact melt composition, but a general estimate of SiO_2 melt content of approximately 60 to 64 wt% is suitable for the purposes of this discussion (after ~58 wt% SiO_2 whole-rock contents for apatite crystallisation: section 4.2.3). The effect of apatite crystallisation on the observed fluorine behaviour of the amphibole-bearing magmas is inferred to be negligible, and amphibole is suggested to exert the strongest control. In contrast, apatite is thought to be the major fluorine-bearing phase in the post-Oruanui amphibole-absent magmas, and thus is inferred to have the largest impact on melt fluorine content.

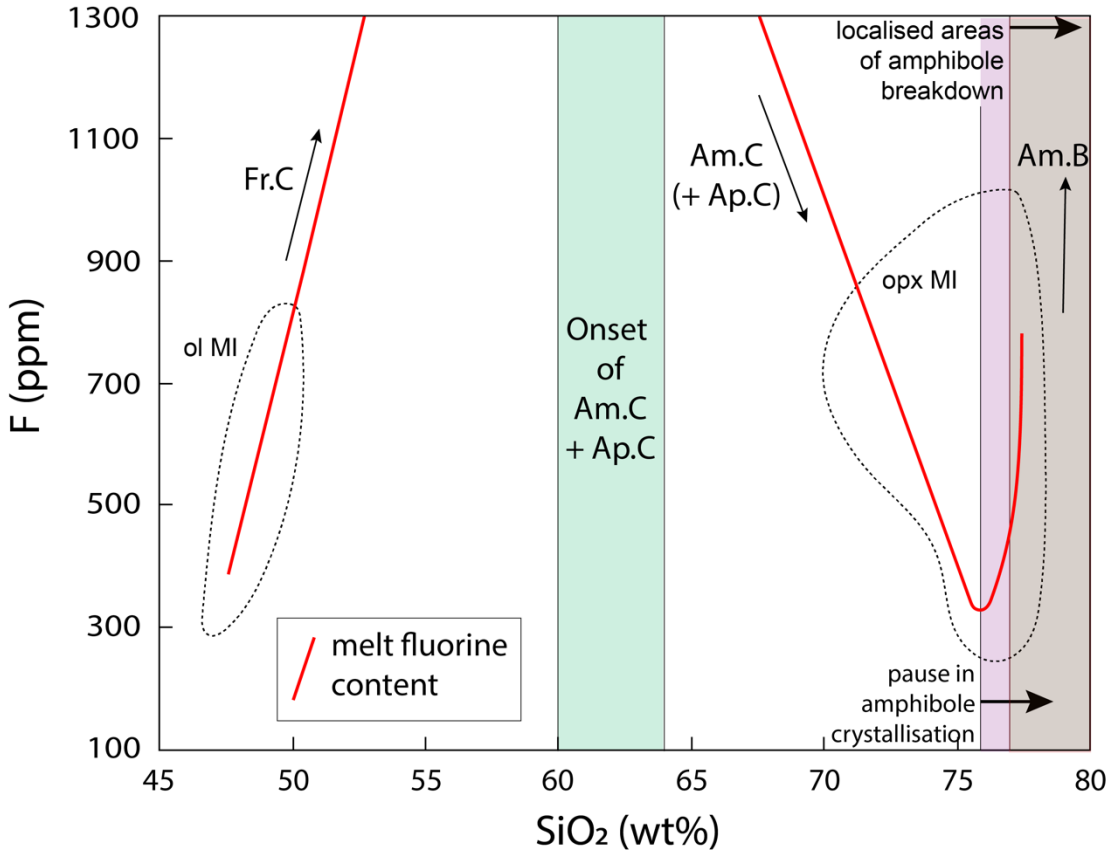

Figure 4. 19. The inferred pathway for fluorine in the melt (red line, ppm) relative to SiO2 (wt%), between the end-member compositions analysed in this study (see Figure 3.8b for data points: dotted lines = olivine-hosted basaltic melt inclusions [ol MI], and orthopyroxene-hosted dacitic to rhyolitic melt inclusions [opx MI]). Thin black arrows represent the primary control on melt fluorine content at that stage (Fr.C = fractional crystallisation; Am.C = amphibole crystallisation; Ap.C = apatite crystallisation; Am.B = amphibole breakdown). The green field denotes a potential range of melt SiO_2 content that amphibole and apatite might begin to crystallise (apatite at whole-rock ~58 wt% SiO_2). The purple field represents the pause in amphibole crystallisation at ~76 wt% SiO_2. The brown field represents amphibole breakdown/resorption in localised parcels of highly evolved magma. See text for discussion.

The steady decrease from intermediate melt compositions down to ~76 wt% SiO_2 is inferred to be controlled by the effects of amphibole and apatite crystallisation on the amphibole-bearing and amphibole-absent Taupō magmas respectively. The apparent increase at HSR compositions is potentially a marker for the cessation of amphibole crystallisation in the mush zone of the Oruanui. The further increase in fluorine contents in the HSR melt inclusions may well represent the resorption of amphibole in the most evolved parcels of HSR melt, but could also be indicative of the compatibility of fluorine in silicate melt. In addition, the post-Oruanui dacite and post-Oruanui rhyolite compositions exhibit opposite trends between their groundmass glass and melt inclusion populations. The depleted dacite groundmass glass values are inferred to represent syn-eruptive degassing, whereas the increase in fluorine from the melt inclusions to the groundmass glass of the rhyolites is consistent with fluorine compatibility in the melt. These differences are inferred to stem from the varying eruptive styles and magma storage conditions (dacites = relatively small volume pyroclastic units sourced from ~920 ˚C and >200 MPa; Y6 = caldera-forming large rhyolitic eruption sourced from ~850 ˚C and ~100 MPa: Barker et al., 2015).

4.6 An integrated volatile pathway model

A schematic model focusing on the parental basaltic magmas, the silicic mush zone, and the melt-dominant magma body is presented in Figure 4.20. The key stages of magma evolution as inferred from the results presented in this thesis are numbered, and summarised in the following text.

1. *Fractional crystallisation of primitive melts* – This is inferred to be the main control on the early behaviour of sulfur, chlorine, and fluorine in the primitive basaltic melts as revealed by high-Mg olivine melt inclusions. The early crystallising assemblage is dominated by olivine and pyroxene, in which the volatile elements are highly incompatible. No magmatic fluids are thought to be saturated at this early stage.
2. *Sulfur saturation* – At depths between the rising basaltic magmas and the base of the silicic mush zone, sulfur is inferred to reach saturation within the melt.

Saturation is due to increasing sulfur content in the melt from fractional crystallisation, and a reducing sulfur solubility level with decreasing fO_2 and increasing SiO_2 content. This leads to the exsolution of a sulfur-rich phase. The proportion of this phase increases relative to the parental magma with further fractional crystallisation and the lowering of sulfur solubility (through decreasing fO_2).

3. *Crystallisation of magnetite, apatite, pyrrhotite, and amphibole* – The exact order in which these minerals crystallise is not fully understood, but the magnetite crisis likely triggers apatite crystallisation. Additional effects include a decrease in fO_2, converting the majority of sulfate present in the melt to sulfide, lowering the sulfur saturation threshold. This is inferred to cause a period of rapid pyrrhotite crystallisation, and the depletion of sulfur in the melt down to near minimum values. The onset of amphibole crystallisation results in the steady depletion of fluorine in the melt of amphibole-bearing magmas. Apatite crystallisation is not thought to have a significant impact on chlorine melt contents, but may be the strongest control on the melt fluorine contents of the amphibole-absent magmas analysed.
4. *Aqueous vapour saturation* – It is possible that the H_2O and CO_2 contents of the melt exceed those required for aqueous vapour saturation at pressures close to those sampled by the deepest Oruanui HSR and post-Oruanui dacites (>250 MPa, 900-950 ˚C: Figure 4.13) , and an aqueous vapour exsolves from the melt. The vapour phase strongly fractionates both sulfur and chlorine, but has little to no effect on fluorine. Melt sulfur contents immediately prior to vapour saturation are near minimum values. Partitioning of sulfur into the aqueous vapour phase keeps sulfur below the saturation threshold, precluding further pyrrhotite crystallisation and buffering melt sulfur at minimal values (<150 ppm) for the remainder of the magma pathway (as sampled by silicic melt inclusions). The vapour is the first phase that significantly fractionates chlorine, and the chlorine content of the melt begins to decrease at a near-constant rate with respect to increasing SiO_2.
5. *Pause in amphibole crystallisation* – Amphibole crystallisation in the Oruanui compositions appears to pause at melt SiO_2 contents >76 wt%. This produces a

transition in fluorine behaviour from depletion to enrichment relative to increasing SiO_2 contents.

6. *Amphibole resorption* – the most evolved parcels of amphibole-bearing magma in the melt-dominant magma body are inferred to have left the amphibole stability field, leading to amphibole resorption (Allan et al., 2013). The concentration of fluorine increases in the melt, having been liberated from the dissolving amphibole crystals.
7. *Syn-eruptive sulfur degassing* – During the final stages of magma ascent and eruption, sulfur degasses strongly from the melt relative to both chlorine and fluorine. However the erupted Taupō magmas are thought to release minor amounts of sulfur through syn-eruptive degassing, due to the marginal differences between the sulfur contents of the silicic melt inclusions and the groundmass glass. Rather, any potential sources of sulfur released during eruptions, such as the 232 CE Taupō eruption, are inferred to be originate from the intrusion of relatively sulfur-rich mafic magmas.

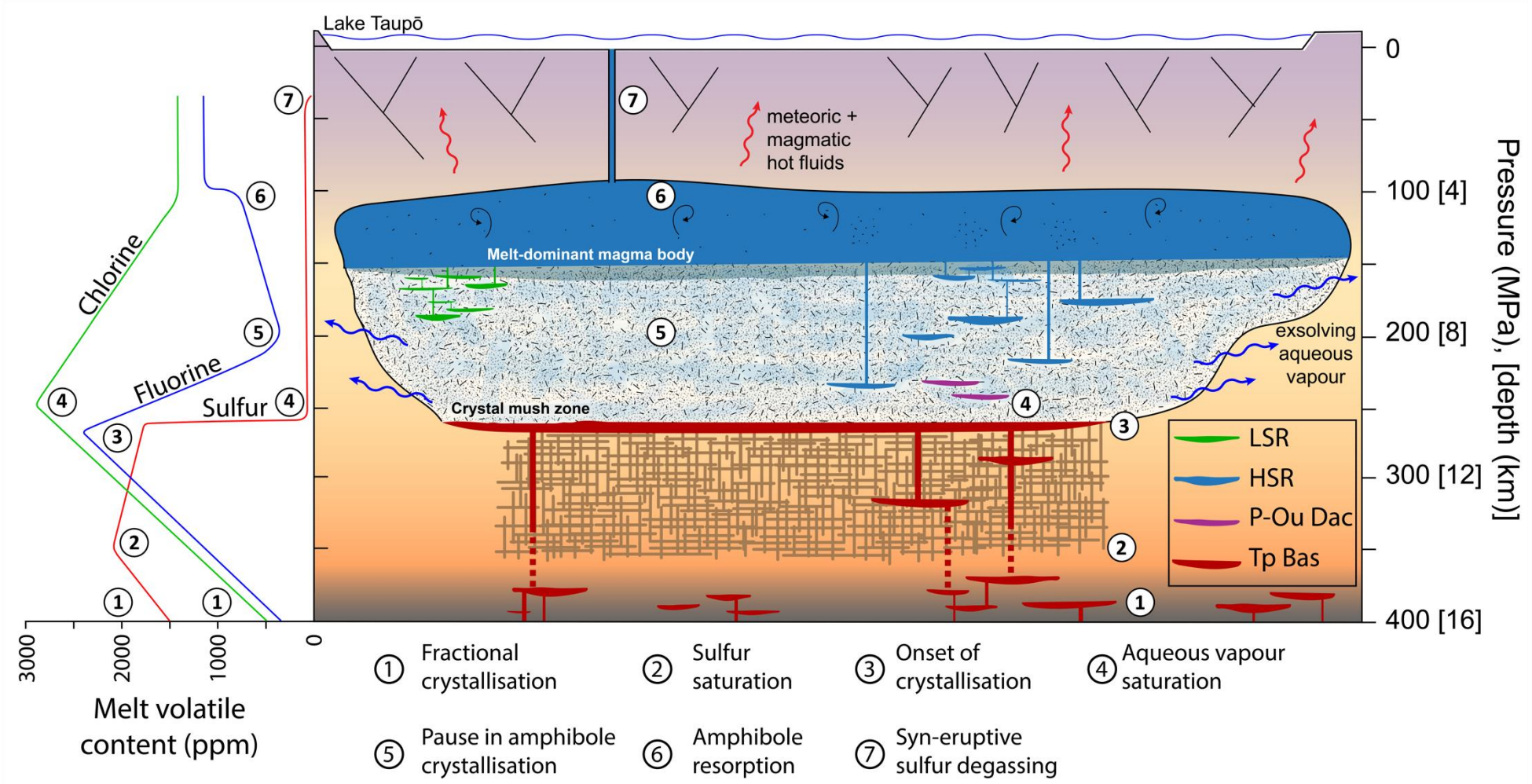

Figure 4. 20. A schematised cross section of the magmatic system beneath Taupō volcano prior to a large silicic eruption, reproduced from Figure 4.1, focusing on the behaviour of volatiles up through the system. Numbers denote the inferred major controls on sulfur, chlorine, and fluorine, from the primitive basalts to silicic syn-eruptive processes. The inferred variations in sulfur, chlorine, and fluorine from the primitive basaltic melts up through the mush system and into the melt-dominant magma body are graphed relative to each other (ppm) against inferred pressure (MPa [km]), with each significant change in their respective trends associated with one of the labelled controls.

5. Conclusions

The volatile data recorded from melt inclusions and groundmass glass from a large range of depths in the magmatic system beneath Taupō volcano, combined with recent and well-established studies of mineral textures and melt inclusion volatile contents (Dunbar et al., 1989a; Hervig et al., 1989; Dunbar and Kyle, 1993; Liu et al., 2006; Charlier et al., 2008, 2012; Allan et al., 2013, 2017; Barker et al., 2015; Bégué et al., 2015a, 2015b, 2017; Myers et al., 2018, 2019), provide new insight into the processes that control volatile transport from source to surface. When coupled with the olivine-hosted melt inclusion data, both recorded in this study and provided by Barker et al. (manuscript in prep), a volatile pathway for sulfur, chlorine, and fluorine can be inferred, from the source basalts, up into and through the more silicic magmas to the shallow crust. In addition, the new suite of apatite data presented in this thesis complements the melt volatile data, and highlights the value of including apatite compositions in geochemical mineral analyses.

5.1 Summary of key findings

The results presented and discussed in this thesis show that the concentrations of sulfur, chlorine, and fluorine in the deep magmas of Taupō volcano can be accurately measured using mafic and silicic melt inclusions, and apatite compositions, hosted within the cores of major mineral phases. In addition, the defining controls on the respective abundances of sulfur, chlorine, and fluorine are inferred to be different for each element. Initial concentrations of all three volatile elements are shown to increase in the basaltic melt as the magmas evolve, but subsequently diverge due to a variety of different processes. The considerable differences in sulfur abundances between the basaltic melts and the dacitic to rhyolitic melts suggest that a significant level of depletion has occurred at intermediate compositions. The saturation of sulfur within the melt and the subsequent crystallisation of pyrrhotite is inferred to be the cause of this depletion, with melt sulfur contents potentially decreased to near-minimum values during rapid pyrrhotite growth associated with magnetite

crystallisation. In contrast, the chlorine content of the melt is observed to increase by 2000 ppm from basaltic (~500 ppm) to more silicic (~1500 to >2000 ppm) compositions. This is a result of the high chlorine solubilities at compositions less evolved than rhyolite. Chlorine does favourably partition into apatite relative to the melt, but the small contribution of apatite to the total crystalline cargo held in the mush- and melt-dominant regions of the magma system is thought to negate any potential fractionating effect. Fluorine contents between the end-member melt compositions show little difference in the spread and values, in contrast to the behaviour exhibited by sulfur and by chlorine. The main control on this uniformity in the amphibole-bearing Taupō magmas is inferred to be amphibole crystallisation (with a subsidiary effect from apatite crystallisation), into which fluorine is fractionated over silicate melt. The melt fluorine contents of post-Oruanui magmas in which amphibole is absent is inferred to be controlled through the crystallisation of apatite.

Sulfur and chlorine both partition strongly into aqueous vapour phases relative to silicate melt, while fluorine is highly soluble in silicate melt under the estimated P-T-composition conditions. These characteristics are clearly expressed in the silicic melt inclusion data (Chapter 3), albeit with a slightly suppressed response from sulfur due to its already depleted concentrations in the melt. Chlorine shows a steady decrease in the melt through favourable partitioning into vapour throughout the entire range of inherited core-hosted melt inclusions, whereas the lack of trends in the sulfur values below 80 ppm is suggested to be produced by a constant buffering effect from the vapour phase. These trends imply that an aqueous vapour phase was already saturated within the melt at less evolved magmatic conditions than those sampled by the melt inclusions analysed here, inferred to be near the base of the magmatic mush zone (900-950 ˚C, >250 MPa).

The apatite halogen data from Oruanui high-silica rhyolite support the general behaviours of both chlorine and fluorine displayed by the melt inclusion data. The fluorine content of the apatite increases with increasing melt evolution and between the orthopyroxene-hosted and microphenocryst apatite, whereas the chlorine content decreases. In addition, the decreasing Cl/F ratio of the apatite from the mush zone to the melt-dominant magma body could be indicative of an actively exsolving aqueous

vapour phase. These trends are relative, however, and so a significant advantage to including apatite in an investigation of magmatic volatile transport is found by using calculated partition coefficients to either support direct melt and/or fluid inclusion halogen analyses, or estimate the halogen content of melt and/or fluid that was not analysed.

The largest contribution to the sulfur emitted during the 232 CE Taupō eruption is inferred to have been supplied by relatively sulfur-rich primitive mafic magma intrusions into the overlying silicic mush. Although it is likely that sulfur was released from an aqueous vapour phase saturated within the silicic magma, and from the significantly disrupted hydrothermal envelope in the surrounding country rock, the total contribution from these two sources is inferred to be insignificant. The involvement of mafic magma in the Oruanui supereruption is clear (Allan et al., 2017; Rooyakkers et al., 2018), and although a sulfur signal associated with the Oruanui has yet to be identified, it is possible that any sulfur released during the eruption was supplied by the intruding primitive magmas.

5.2 Suggestions for future studies

There are a range of potential avenues that could be explored in future studies to further develop a better understanding of the volatile pathways in the magmatic system beneath Taupō volcano:

1. The lack of compositionally intermediate melt inclusions from silicic eruptive deposits of Taupō limits the establishment of a complete magmatic volatile pathway from the source mafic magmas to syn-eruptive degassing of rhyolite. However, further crystal-specific studies could further the work presented in this thesis. An in-depth analysis of the halogen contents of Taupō amphibole would be a valuable area of research to complement the data suites presented here. This work would effectively constrain the role of amphibole crystallisation in controlling the halogen budget of the melt, and illuminate any small-scale variations in halogen behaviours up through the silicic system.

2. In broadening the scope of potential future work to outside crystal-specific investigations, there would be significant benefit in measuring the volatile contents (particularly sulfur) of the central Taupō volcanic zone (TVZ) geothermal systems. Constraining the sulfur budget of magmatic fluid contributions to the geothermal systems would support the data presented here, and vastly improve our knowledge of the sulfur budget of Taupō magmatic system.
3. An expansion of this study to other volcanoes in the TVZ. Comparing the results presented here for Taupō volcano with those from another hyperactive silicic caldera-forming volcano (e.g. Okataina) would help constrain whether the volatile pathways presented in this thesis are typical or unique for large silicic magma systems. The effects of a different crystalline assemblage (e.g. biotite is common in Okataina eruptives: Ewart et al., 1975; Shane et al., 2008b; Charlier and Wilson, 2010; Johnson et al., 2013), on the behaviour of volatiles could be assessed. In addition, further comparison with the volatile budgets of the northern and southern andesite-dominated regions may illuminate any variations in the supply of sulfur, fluorine, and chlorine along the length of the TVZ.

6. References

Aiuppa, A., Baker, D. R., Webster, J. D. 2009. Halogens in volcanic systems. Chemical Geology, 263, 1-18.

Allan, A. S. R. 2013. The Oruanui Eruption: Insights into the Generation and Dynamics of the World's Youngest Supereruption. Ph. D. thesis. Victoria University of Wellington, Wellington, New Zealand.

Allan, A. S. R., Wilson, C. J. N., Millet, M.-A., Wysoczanski, R. J. 2012. The invisible hand: Tectonic triggering and modulation of a rhyolitic supereruption. Geology, 40, 563-566.

Allan, A. S. R., Morgan, D. J., Wilson, C. J. N., Millet, M.-A. 2013. From mush to eruption in centuries: Assembly of the super-sized Oruanui magma body. Contributions to Mineralogy and Petrology, 166, 143-164.

Allan, A. S. R., Barker, S. J., Millet, M.-A., Morgan, D. J., Rooyakkers, S. M., Schipper, C. I., Wilson, C. J. N. 2017. A cascade of magmatic events during the assembly and eruption of a super-sized magma body. Contributions to Mineralogy and Petrology, 172, 49.

Ayers, J. C., Watson, E. B. 1993. Apatite/fluid partitioning of rare-earth elements and strontium: Experimental results at 1.0 GPa and 1000 °C and application to models of fluid-rock interaction. Chemical Geology, 110, 299-314.

Bachmann, O., Bergantz, G. W. 2004. On the origin of crystal-poor rhyolites: Extracted from batholithic crystal mushes. Journal of Petrology, 45, 1565-1582.

Bachmann, O., Bergantz, G. W. 2008. Rhyolites and their source mushes across tectonic settings. Journal of Petrology, 49, 2277-2285.

Bachmann, O., Huber, C. 2016. Silicic magma reservoirs in the Earth's crust. American Mineralogist, 101, 2377-2404.

Baker, D. R., Alletti, M. 2012. Fluid saturation and volatile partitioning between melts and hydrous fluids in crustal magmatic systems: The contribution of experimental measurements and solubility models. Earth-Science Reviews, 114, 298-324.

Baker, D. R., Moretti, R. 2011. Modeling the solubility of sulfur in magmas: A 50-year old geochemical challenge. Reviews in Mineralogy and Geochemistry, 73, 167-213.

Barker, S. J. 2014. Post-Oruanui supereruption recovery, reconstruction and evolution of Taupo volcano, New Zealand. Ph. D. thesis. Victoria University of Wellington, Wellington, New Zealand.

Barker, S. J., Wilson, C. J. N., Smith, E. G. C., Charlier, B. L. A., Wooden, J. L., Hiess, J., Ireland, T. R. 2014. Post-supereruption magmatic reconstruction of Taupo volcano (New Zealand), as reflected in zircon ages and trace elements. Journal of Petrology, 55, 1511-1533.

Barker, S. J., Wilson, C. J. N., Allan, A. S. R., Schipper, C. I. 2015. Fine-scale temporal recovery, reconstruction and evolution of a post-supereruption magmatic system. Contributions to Mineralogy and Petrology, 170, 5.

Barker, S. J., Wilson, C. J. N., Morgan, D. J., Rowland, J. V. 2016. Rapid priming, accumulation, and recharge of magma driving recent eruptions at a hyperactive caldera volcano. Geology, 44, 323-326.

Barker, S. J., Rowe, M. C., Wilson C. J. N., Gamble, J. A., Rooyakkers, S. M., Charlier, B. L. A, Wysoczanski, R. J., Baker, J. A., Kenworthy, C. C. (manuscript in prep). Reconstructing the primitive magmas fueling voluminous silicic volcanism using olivine-hosted melt inclusions. Geology.

Bégué, F., Deering, C. D., Gravley, D. M., Kennedy, B. M., Chambefort, I., Gualda, G. A. R., Bachmann, O. 2014. Extraction, storage and eruption of multiple isolated magma batches in the paired Mamaku and Ohakuri eruption, Taupo volcanic zone, New Zealand. Journal of Petrology, 55, 1653-1684.

Bégué, F., Deering, C. D., Chambefort, I., Gravley, D. M., Kennedy, B. M. 2015a. Link between magmatic degassing and geothermal systems; Taupo Volcanic Zone, New Zealand. In: Proceedings of the World Geothermal Congress. Melbourne, Australia, 19-25 April, (p. 12).

Bégué, F., Gravley, D. M., Chambefort, I., Deering, C. D., Kennedy, B. M. 2015b. Magmatic volatile distribution as recorded by rhyolitic melt inclusions in the Taupo Volcanic Zone, New Zealand. Geological Society of London, Special Publications, 410, 71-94.

Bégué, F., Deering, C. D., Gravley, D. M., Chambefort, I., Kennedy, B. M. 2017. From source to surface: Tracking magmatic boron and chlorine input into the geothermal systems of the Taupo Volcanic Zone, New Zealand. Journal of Volcanology and Geothermal Research, 346, 141-150

Behr, Y., Townend, J., Bannister, S., Savage, M. K. 2011. Crustal shear wave tomography of the Taupo Volcanic Zone, New Zealand, via ambient noise correlation between multiple three-component networks. Geochemistry, Geophysics, Geosystems, 12, Q03015.

Behrens, H., Gaillard, F. 2006. Geochemical aspects of melts: Volatiles and redox behavior. Elements, 2, 275-280.

Belousova, E. A., Walters, S., Griffin, W. L., O'Reilly, S. Y. 2001. Trace-element signatures of apatites in granitoids from the Mt Isa Inlier, Northwestern Queensland. Australian Journal of Earth Sciences, 48, 603-619.

Belousova, E. A., Griffin, W. L., O'Reilly, S. Y., Fisher, N. I. 2002. Apatite as an indicator mineral for mineral exploration: Trace-element compositions and their relationship to host rock type. Journal of Geochemical Exploration, 76, 45-69.

Beresford, S. W., Cole, J. W., Weaver, S. D. 2000. Weak chemical and mineralogical zonation in the Kaingaroa Ignimbrite, Taupo Volcanic Zone, New Zealand. New Zealand Journal of Geology and Geophysics, 43, 639-650.

Bernal, N. F., Gleeson, S. A., Dean, A. S., Liu, X. M., Hoskin, P. 2014. The source of halogens in geothermal fluids from the Taupo Volcanic Zone, North Island, New Zealand. Geochimica et Cosmochimica Acta, 126, 265-283.

Bibby, H. M., Caldwell, T. G., Davey, F. J., Webb, T. H. 1995. Geophysical evidence on the structure of the Taupo Volcanic Zone and its hydrothermal circulation. Journal of Volcanology and Geothermal Research, 68, 29-58.

Bindeman, I. N., Simakin, A. G. 2014. Rhyolites-hard to produce, but easy to recycle and sequester: Integrating microgeochemical observations and numerical models. Geosphere, 10, 930-957.

Binder, B., Wenzel, T., Keppler, H. 2018. The partitioning of sulfur between multicomponent aqueous fluids and felsic melts. Contributions to Mineralogy and Petrology, 173, 18.

Bloomberg, S., Werner, C., Rissmann, C., Mazot, A., Horton, T., Gravley, D., Kennedy, B., Oze, C. 2014. Soil CO_2 emissions as a proxy for heat and mass flow assessment, Taupō Volcanic Zone, New Zealand. Geochemistry, Geophysics, Geosystems, 15, 4885-4904.

Bonifacie, M., Busigny, V., Mevel, C., Philippot, P., Agrinier, P., Jendrzejewski, N., Scambelluri, M., Javoy, M. 2008. Chlorine isotopic composition in seafloor

serpentinites and high-pressure metaperidotites. Insights into oceanic serpentinization and subduction processes. Geochimica et Cosmochimica Acta, 72, 126-139.

Botcharnikov, R. E., Behrens, H., Holtz, F., Koepke, J., Sato, H. 2004. Sulfur and chlorine solubility in Mt. Unzen rhyodacitic melt at 850 °C and 200 MPa. Chemical Geology, 213, 207-225.

Boyce, J. W., Hervig, R. L. 2008. Magmatic degassing histories from apatite volatile stratigraphy. Geology, 36, 63-66.

Brenan, J. 1994. Kinetics of fluorine, chlorine and hydroxyl exchange in fluorapatite. Chemical Geology, 110, 195-210.

Bureau, H., Keppler, H. 1999. Complete miscibility between silicate melts and hydrous fluids in the upper mantle: Experimental evidence and geochemical implications. Earth and Planetary Science Letters, 165, 187-196.

Burnham, C. W. 1979. Magmas and hydrothermal fluids. In: Barnes, H. L. (ed.). Geochemistry of Hydrothermal Ore Deposits, 2nd edn. 71-133. John Wiley and Sons, New York, NY.

Candela, P. A. 1986. Toward a thermodynamic model for the halogens in magmatic systems: An application to melt-vapor-apatite equilibria. Chemical Geology, 57, 289-301.

Carroll, M. R., Rutherford, M. J. 1985. Sulfide and sulfate saturation in hydrous silicate melts. Journal of Geophysical Research, 90, 601-612.

Carroll, M. R., Rutherford, M. J. 1987. The stability of igneous anhydrite: Experimental results and implications for sulfur behavior in the 1982 El Chichon trachyandesite and other evolved magmas. Journal of Petrology, 28, 781-801.

Carroll, M. R., Webster, J. D. 1994. Solubilities of sulfur, noble gases, nitrogen, chlorine, and fluorine in magmas. Reviews in Mineralogy and Geochemistry, 30, 231-279.

Chambefort, I., Dilles, J. H., Longo, A. 2013. Amphibole Geochemistry of the Yanacocha Volcanics, Peru: Evidence for Diverse Sources of Magmatic Volatiles Related to Gold Ores. Journal of Petrology, 54, 1017-1046.

Chambefort, I., Lewis, B., Wilson, C. J. N., Rae, A. J., Coutts, C., Bignall, G., Ireland, T. R. 2014. Stratigraphy and structure of the Ngatamariki geothermal system from new zircon U-Pb geochronology: Implications for Taupo Volcanic Zone evolution. Journal of Volcanology and Geothermal Research, 274, 51-70.

Charlier, B. L. A., Wilson, C. J. N. 2010. Chronology and evolution of caldera-forming and post-caldera magma systems at Okataina volcano, New Zealand from zircon U-Th model-age spectra. Journal of Petrology, 51, 1121-1141.

Charlier, B. L. A., Wilson, C. J. N., Lowenstern, J. B., Blake, S., van Calsteren, P. W., Davidson, J. P. 2005. Magma generation at a large, hyperactive silicic volcano (Taupo, New Zealand) revealed by U-Th and U-Pb systematics in zircons. Journal of Petrology, 46, 3-32.

Charlier, B. L. A., Wilson, C. J. N., Davidson, J. P. 2008. Rapid open-system assembly of a large silicic magma body: Time-resolved evidence from cored plagioclase crystals in the Oruanui eruption deposits, New Zealand. Contributions to Mineralogy and Petrology, 156, 799-813.

Charlier, B. L. A., Wilson, C. J. N., Mortimer, N. 2010. Evidence from zircon U-Pb age spectra for crustal structure and felsic magma genesis at Taupo volcano, New Zealand. Geology, 38, 915-918.

Charlier, B. L. A., Morgan, D. J., Wilson, C. J. N., Wooden, J. L., Allan, A. S. R., Baker, J. A. 2012. Lithium concentration gradients in feldspar and quartz record the final minutes of magma ascent in an explosive supereruption. Earth and Planetary Science Letters, 319-230, 218-227.

Chou, I. M. 1987. Phase relations in the system NaCl-KCl-H_2O. III: Solubilities of halite in vapor-saturated liquids above 445 °C and redetermination of phase equilibrium properties in the system NaCl-H_2O to 1000 °C and 1500 bars. Geochimica et Cosmochimica Acta, 51, 1965-1976.

Christenson, B. W., Mroczek, E. K., Kennedy, B. M., Van Soest, M. C., Stewart, M. K., Lyon, G. 2002. Ohaaki reservoir chemistry: Characteristics of an arc-type hydrothermal system in the Taupo Volcanic Zone, New Zealand. Journal of Volcanology and Geothermal Research, 115, 53-82.

Chu, M. F., Wang, K. L., Griffin, W. L., Chung, S. L., O'Reilly, S. Y., Pearson, N. J., Iizuka, Y. 2009. Apatite composition: Tracing petrogenetic processes in Transhimalayan granitoids. Journal of Petrology, 50, 1829-1855.

Clemente, B., Scaillet, B., Pichavant, M. 2004. The solubility of sulphur in hydrous rhyolitic melts. Journal of Petrology, 45, 2171-2196.

Cole, J. W., Lewis, K. B. 1981. Evolution of the Taupo-Hikurangi subduction system. Tectonophysics, 72, 1-21.

Cole, J. W., Darby, D. J., Stern, T. A. 1995. Taupo Volcanic Zone and Central Volcanic Region backarc structures of North Island, New Zealand. In: Taylor, B. (ed.). Backarc Basins, 1-28. Springer, Boston, MA.

Cole, J. W., Deering, C. D., Burt, R. M., Sewell, S., Shane, P. A. R., Matthews, N. E. 2014. Okataina Volcanic Centre, Taupo Volcanic Zone, New Zealand: A review of volcanism and synchronous pluton development in an active, dominantly silicic caldera system. Earth-Science Reviews, 128, 1-17.

Cooper, G. F., Morgan, D. J., Wilson, C. J. N. 2017. Rapid assembly and rejuvenation of a large silicic magmatic system: Insights from mineral diffusive profiles in the Kidnappers and Rocky Hill deposits, New Zealand. Earth and Planetary Science Letters, 473, 1-13.

Crisp, J. A. 1984. Rates of magma emplacement and volcanic output. Journal of Volcanology and Geothermal Research, 20, 177-211.

Dalou, C., Koga, K. T., Le Voyer, M., Shimizu, N. 2014. Contrasting partition behavior of F and Cl during hydrous mantle melting: implications for Cl/F signature in arc magmas. Progress in Earth and Planetary Science, 1, 26.

De Vivo, B., Lima A., Webster J.D. 2005. Volatiles in magmatic-volcanic systems. Elements, 1, 19-24.

Deering, C. D., Cole, J. W., Vogel, T. A. 2008. A rhyolite compositional continuum governed by lower crustal source conditions in the Taupo volcanic zone, New Zealand. Journal of Petrology, 49, 2245-2276.

Deering, C. D., Gravley, D. M., Vogel, T. A., Cole, J. W., Leonard, G. S. 2010. Origins of cold-wet-oxidizing to hot-dry-reducing rhyolite magma cycles and distribution in the Taupo Volcanic Zone, New Zealand. Contributions to Mineralogy and Petrology, 160, 609-629.

Deering, C. D., Cole, J. W., Vogel, T. A. 2011. Extraction of crystal-poor rhyolite from a hornblende-bearing intermediate mush: A case study of the caldera-forming Matahina eruption, Okataina volcanic complex. Contributions to Mineralogy and Petrology, 161, 129-151.

Devine, J. D., Sigurdsson, H., Davis, A. N., Self, S. 1984. Estimates of sulfur and chlorine yield to the atmosphere from volcanic eruptions and potential climatic effects. Journal of Geophysical Research, 89, 6309-6325.

Doherty, A. L., Webster, J. D., Goldoff, B. A., Piccoli, P. M. 2014. Partitioning behavior of chlorine and fluorine in felsic melt-fluid(s)-apatite systems at 50 MPa and 850-950 °C. Chemical Geology, 384, 94-111.

Dolejš, D., Baker, D. R. 2007. Liquidus equilibria in the system K_2O–Na_2O–Al_2O_3–SiO_2–F_2O–1–H_2O to 100 MPa: I. Silicate-fluoride liquid immiscibility in anhydrous systems. Journal of Petrology, 48, 785-806.

Dolejš, D., Zajacz, Z. 2018. Halogens in silicic magmas and their hydrothermal systems. In: Harlov, D. E., Aranovich, L. (eds.). The Role of Halogens in Terrestrial and Extraterrestrial Geochemical Processes, Springer, 31-543.

Dunbar, N. W., Kyle, P. R. 1993. Lack of volatile gradient in the Taupo plinian-ignimbrite transition: evidence from melt inclusion analysis. American Mineralogist, 78, 612-618.

Dunbar, N. W., Hervig, R. L., Kyle, P. R. 1989a. Determination of pre-eruptive H_2O, F and Cl contents of silicic magmas using melt inclusions: Examples from Taupo volcanic center, New Zealand. Bulletin of Volcanology, 51, 177-184.

Dunbar, N. W., Kyle, P. R., Wilson, C. J. N. 1989b. Evidence for limited zonation in silicic magma systems, Taupo Volcanic Zone, New Zealand. Geology, 17, 234-236.

Eastwood, A. A., Gravley, D. M., Wilson, C. J. N., Chambefort, I., Oze, C., Cole, J. W., Ireland, T. R. 2013. U-Pb dating of subsurface pyroclastic deposits (Tahorakuri Formation) at Ngatamariki and Rotokawa geothermal fields. In: Proceedings of the 35th New Zealand Geothermal Workshop, 8. Rotorua, New Zealand. 18-21 November.

Edmonds, M., Wallace, P. J. 2017. Volatiles and exsolved vapor in volcanic systems. Elements, 13, 29-34.

Eichelberger, J. C., Izbekov, P. E., Browne, B. L. 2006. Bulk chemical trends at arc volcanoes are not liquid lines of descent. Lithos, 87, 135-154.

Ekström, T. K. 1972. The distribution of fluorine among some coexisting minerals. Contributions to Mineralogy and Petrology, 34, 192-200.

Ersoy, E. Y. 2013. PETROMODELER (Petrological Modeler) a Microsoft Excel spreadsheet program for modelling melting, mixing, crystallization and assimilation processes in magmatic systems. Turkish Journal of Earth Sciences, 22, 115-125.

Ewart, A. 1982. The mineralogy and petrology of Tertiary-Recent orogenic volcanic rocks: with special reference to the andesitic–basaltic compositional range. In: Thorpe, R.S. (ed.). Andesites. John Wiley and Sons, Chichester, 25-95.

Ewart, A., Hildreth, W., Carmichael, I. S. E. 1975. Quaternary acid magma in New Zealand. Contributions to Mineralogy and Petrology, 51, 1-27.

Fincham, C. J. B., Richardson, F. D. 1954. The behaviour of sulphur in silicate and aluminate melts. Proceedings of the Royal Society of London, A223, 40-62.

Gelman, S. E., Deering, C. D., Gutierrez, F. J., Bachmann, O. 2013. Evolution of the Taupo Volcanic Center, New Zealand: Petrological and thermal constraints from the Omega dacite. Contributions to Mineralogy and Petrology, 166, 1355-1374.

Giggenbach, W. F. 1995. Variations in the chemical and isotopic composition of fluids discharged from the Taupo Volcanic Zone, New Zealand. Journal of Volcanology and Geothermal Research, 68, 89-116.

Goldoff, B., Webster, J. D., Harlov, D. E. 2012. Characterization of fluor-chlorapatites by electron probe microanalysis with a focus on time-dependent intensity variation of halogens. American Mineralogist, 97, 1103-1115.

Graeter, K. A., Beane, R. J., Deering, C. D., Gravley, D., Bachmann, O. 2015. Formation of rhyolite at the Okataina Volcanic Complex, New Zealand: New insights from analysis of quartz clusters in plutonic lithics. American Mineralogist, 100, 1778-1789.

Graf, H.-F., Feichter, J., Langmann, B. 1997. Volcanic sulfur emissions: Estimates of source strength and its contribution to the global sulfate distribution. Journal of Geophysical Research, 102, 10727-10738.

Graham, I. J., Cole, J. W., Briggs, R. M., Gamble, J. A., Smith, I. E. M. 1995. Petrology and petrogenesis of volcanic rocks from the Taupo Volcanic Zone: a review. Journal of Volcanology and Geothermal Research, 68, 59-87.

Gravley, D. M., Wilson, C. J. N., Leonard, G. S., Cole, J. W. 2007. Double trouble: Paired ignimbrite eruptions and collateral subsidence in the Taupo Volcanic Zone, New Zealand. Bulletin of the Geological Society of America, 119, 18-30.

Gravley, D. M., Deering, C. D., Leonard, G. S., Rowland, J. V. 2016. Ignimbrite flare-ups and their drivers: A New Zealand perspective. Earth-Science Reviews, 162, 65-82.

Harrison, A. J., White, R. S. 2004. Crustal structure of the Taupo Volcanic Zone, New Zealand: Stretching and igneous intrusion. Geophysical Research Letters, 31, L13615.

Harrison, A. J., White, R. S. 2006. Lithospheric structure of an active backarc basin: The Taupo Volcanic Zone, New Zealand. Geophysical Journal International, 167, 968-990.

Hawkesworth, C. J., Blake, S., Evans, P., Hughes, R., Macdonald, R., Thomas, L. E., Turner, S. P., Zellmer, G. 2000. Time scales of crystal fractionation in magma chambers-integrating physical, isotopic and geochemical perspectives. Journal of Petrology, 41, 991-1006.

Heise, W., Caldwell, T. G., Bibby, H. M., Bennie, S. L. 2010. Three-dimensional electrical resistivity image of magma beneath an active continental rift, Taupo Volcanic Zone, New Zealand. Geophysical Research Letters, 37, L10301.

Hellstrom, J., Paton, C., Woodhead, J. D., Hergt, J. M. 2008. Iolite: software for spatially resolved LA-(quad and MC) ICPMS analysis. In: Sylvester, P. (ed.). Laser Ablation ICP-MS in the Earth Sciences: Current Practices and Outstanding Issues. Mineralogical Association of Canada Short Course Series, 40, 343-348.

Hervig, R. L., Dunbar, N., Westrich, H. R., Kyle, P. R. 1989. Pre-eruptive water content of rhyolitic magmas as determined by ion microprobe analyses of melt inclusions in phenocrysts. Journal of Volcanology and Geothermal Research, 36, 293-302.

Hildreth, W. 1981. Gradients in silicic magma chambers: implications for lithospheric magmatism. Journal of Geophysical Research, 86, 10153-10192.

Hildreth, W. 2004. Volcanological perspectives on Long Valley, Mammoth Mountain, and Mono Craters: Several contiguous but discrete systems. Journal of Volcanology and Geothermal Research, 136, 169-198.

Hildreth, W., Moorbath, S. 1988. Crustal contributions to arc magmatism in the Andes of Central Chile. Contributions to Mineralogy and Petrology, 98, 455-489.

Hildreth, W., Wilson, C. J. N. 2007. Compositional zoning of the Bishop Tuff. Journal of Petrology, 48, 951-999.

Hochstein, M. P. 1995. Crustal heat transfer in the Taupo Volcanic Zone (New Zealand): comparison with other volcanic arcs and explanatory heat source models. Journal of Volcanology and Geothermal Research, 68, 117-151.

Hogg, A. G., Lowe, D. J., Palmer, J., Boswijk, G., Bronk Ramsey, C. 2012. Revised calendar date for the Taupo eruption derived by ^{14}C wiggle-matching using a New Zealand kauri ^{14}C calibration data set. The Holocene, 22, 439-449.

Houghton, B. F., Wilson, C. J. N., McWilliams, M. O., Lanphere, M. A., Weaver, S. D., Briggs, R. M., Pringle, M. S. 1995. Chronology and dynamics of a large silicic magmatic system: Central Taupo Volcanic Zone , New Zealand. Geology, 23, 13-16.

Hughes, J. M., Rakovan, J. 2002. The crystal structure of apatite, $Ca_5(PO_4)_3(F,OH,Cl)$. Reviews in Mineralogy and Geochemistry, 48, 1-12.

Jenner, F. E., O'Neill, H. St. C. 2012. Analysis of 60 elements in 616 ocean floor basaltic glasses. Geochemistry, Geophysics, Geosystems, 13, Q02005.

Jenner, F. E., O'Neill, H. St. C., Arculus, R. J., Mavrogenes, J. A. 2010. The magnetite crisis in the evolution of arc-related magmas and the initial concentration of Au, Ag and Cu. Journal of Petrology, 51, 2445-2464.

Joachim, B., Pawley, A., Lyon, I. C., Marquardt, K., Henkel, T., Clay, P. L., Ruzié, L., Burgess, R., Ballentine, C. J. 2015. Experimental partitioning of F and Cl between olivine, orthopyroxene and silicate melt at Earth's mantle conditions. Chemical Geology, 416, 65-78.

John, T., Scambelluri, M., Frische, M., Barnes, J. D., Bach, W. 2011. Dehydration of subducting serpentinite: Implications for halogen mobility in subduction zones and the deep halogen cycle. Earth and Planetary Science Letters, 308, 65-76.

Johnson, E. R., Kamenetsky, V. S., McPhie, J., Wallace, P. J. 2011. Degassing of the H_2O-rich rhyolites of the Okataina Volcanic Center, Taupo Volcanic Zone, New Zealand. Geology, 39, 311-314.

Johnson, E. R., Kamenetsky, V. S., McPhie, J. 2013. The behavior of metals (Pb, Zn, As, Mo, Cu) during crystallization and degassing of rhyolites from the Okataina Volcanic Center, Taupo Volcanic Zone, New Zealand. Journal of Petrology, 54, 1641-1659.

Jugo, P. J. 2009. Sulfur content at sulfide saturation in oxidized magmas. Geology, 37, 415-418.

Jugo, P. J., Luth, R. W., Richards, J. P. 2005a. An experimental study of the sulfur content in basaltic melts saturated with immiscible sulfide or sulfate liquids at 1300 °C and 1.0 GPa. Journal of Petrology, 46, 783-798.

Jugo, P., Luth, R., Richards, J. 2005b. Experimental data on the speciation of sulfur as a function of oxygen fugacity in basaltic melts. Geochimica et Cosmochimica Acta, 69, 497-503.

Keppler, H. 2010. The distribution of sulfur between haplogranitic melts and aqueous fluids. Geochimica et Cosmochimica Acta, 74, 645-660.

Kravchuk, I. F., Keppler, H. 1994. Distribution of chloride between aqueous fluids and felsic melts at 2 kbar and 800 °C. European Journal of Mineralogy 6, 913-924.

Larocque, A. C. L., Stimac, J. A. 2000. Evidence for open-system behavior in immiscible Fe-S-O liquids in silicate magmas: implications for contributions of metals and sulfur to ore-forming fluids. Canadian Mineralogist, 38, 1233-1249.

Liu, Y., Comodi, P. 1993. Some aspects of the crystal-chemistry of apatites. Mineralogical Magazine, 57, 709-719.

Liu, Y., Anderson, A. T., Wilson, C. J. N., Davis, A. M., Steele, I. M. 2006. Mixing and differentiation in the Oruanui rhyolitic magma, Taupo, New Zealand: Evidence from volatiles and trace elements in melt inclusions. Contributions to Mineralogy and Petrology, 151, 71-87.

Liu, Y., Samaha, N. T., Baker, D. R. 2007. Sulfur concentration at sulfide saturation (SCSS) in magmatic silicate melts. Geochimica et Cosmochimica Acta, 71, 1783-1799.

Liu, Z., Shao, Y., Zhou, H., Liu, N., Huang, K., Liu, Q., Zhang, J., Wang, C. 2018. Major and trace element geochemistry of pyrite and pyrrhotite from stratiform and lamellar orebodies: Implications for the ore genesis of the Dongguashan copper (gold) deposit, Eastern China. Minerals, 8, 380.

London, D., Hervig, R. L., Morgan VI, G. B. 1988. Melt-vapor solubilities and elemental partitioning in peraluminous granite-pegmatite systems: experimental results with Macusani glass at 200 MPa. Contributions to Mineralogy and Petrology, 99, 360-373.

Lowenstern J. B. 1995. Applications of silicate-melt inclusions to the study of magmatic volatiles. In: Thompson J. F. H. (ed.) Magmas, Fluids, and Ore Deposits. Mineralogical Association of Canada Short Course, 23, 71-99.

Lowenstern, J. B. 2000. A review of the contrasting behavior of two magmatic volatiles: Chlorine and carbon dioxide. Journal of Geochemical Exploration, 69, 287-290.

Lowenstern, J. B. 2003. Melt inclusions come of age: Volatiles, volcanoes, and Sorby's legacy. In: Bodnar, R. J., De Vivo, B. (eds.). Melt Inclusions in Volcanic Systems: Developments in Volcanology, Elsevier, Amsterdam, 5, 1-21.

Luhr, J. F. 1990. Experimental phase relations of water- and sulfur-saturated arc magmas and the 1982 eruptions of El Chichón volcano. Journal of Petrology, 31, 1071-1114.

Luth, R. W. 2003. Mantle volatiles-distribution and consequences. Treatise on Geochemistry, 2, 319-361.

Marks, M. A. W., Wenzel, T., Whitehouse, M. J., Loose, M., Zack, T., Barth, M., Worgard, L., Krasz, V., Eby, G. N.,Stosnach, H., Markl, G. 2012. The volatile inventory (F, Cl, Br, S, C) of magmatic apatite: An integrated analytical approach. Chemical Geology, 291, 241-255.

Marschall, H. R., Altherr, R., Gméling, K., Kasztovszky, Z. 2009. Lithium, boron and chlorine as tracers for metasomatism in high-pressure metamorphic rocks: A case study from Syros (Greece). Mineralogy and Petrology, 95, 291-302.

Marsh, B. D. 1981. On the crystallinity, probability of occurrence, and rheology of lava and magma. Contributions to Mineralogy and Petrology, 78, 85-98.

Martin, D., Nokes, R. 1988. Crystal settling in a vigorously converting magma chamber. Nature, 332, 534-536.

Marzoli, A., Callegaro, S., Baker, D. R., Geraki, K., Maneta, V. 2015. Investigating sulfur partitioning between nominally volatile-free minerals and silicate melts. In: AGU Fall Meeting Abstracts. San Francisco, CA. 14-18 December, V43C-3164.

Mathez, E. A., Webster, J. D. 2005. Partitioning behavior of chlorine and fluorine in the system apatite-silicate melt-fluid. Geochimica et Cosmochimica Acta, 69, 1275-1286.

McCubbin, F. M., Kaaden, K. E. V., Tartèse, R., Klima, R. L., Liu, Y., Mortimer, J., Barnes, J. J., Shearer, C. K., Treiman, A. H., Lawrence, D. J., Elardo, S. M., Hurley, D. M., Boyce, J. W., Anand, M. 2015. Magmatic volatiles (H, C, N, F, S, Cl) in the lunar mantle, crust, and regolith: Abundances, distributions, processes, and reservoirs. American Mineralogist, 100, 1668-1707.

Métrich, N., Mandeville, C. W. 2010. Sulfur in magmas. Elements, 6, 81-86.

Moretti, R., Baker, D. R. 2008. Modeling the interplay of fO_2 and fS_2 along the FeS-silicate melt equilibrium. Chemical Geology, 256, 286-298.

Morgan VI, G. B., London, D. 1996. Optimizing the electron microprobe analysis of hydrous alkali aluminosilicate glasses. American Mineralogist, 81, 1176-1185.

Mungall, J. E. 2003. Magmatic Ore Deposits. Treatise on Geochemistry, 3, 1-33.

Myers, M. L., Wallace, P. J., Wilson, C. J., Watkins, J. M., Liu, Y. 2018. Ascent rates of rhyolitic magma at the onset of three caldera-forming eruptions. American Mineralogist, 103, 952-965.

Myers, M. L., Wallace, P. J., Wilson, C. J. N. 2019. Inferring magma ascent timescales and reconstructing conduit processes in explosive rhyolitic eruptions using diffusive losses of hydrogen from melt inclusions. Journal of Volcanology and Geothermal Research, 369, 95-112.

Nairn, I. A. 2002. Geology of the Okataina Volcanic Centre, scale 1:50,000, Institute of Geological and Nuclear Sciences geological map 25. 1 sheet + 156 p. Institute of Geological and Nuclear Sciences Limited, Lower Hutt, New Zealand.

Newman, S., Lowenstern, J. B. 2002. VolatileCalc: a silicate melt–H_2O–CO_2 solution model written in Visual Basic for excel. Computers & Geosciences, 28, 597-604.

Oppenheimer, C. 2003. Volcanic degassing. Treatise on Geochemistry, 3, 123-166.

Parat, F., Holtz, F. 2004. Sulfur partitioning between apatite and melt and effect of sulfur on apatite solubility at oxidizing conditions. Contributions to Mineralogy and Petrology, 147, 201-212.

Parat, F., Holtz, F. 2005. Sulfur partition coefficient between apatite and rhyolite: The role of bulk S content. Contributions to Mineralogy and Petrology, 150, 643-651.

Parat, F., Dungan, M. A., Streck, M. J. 2002. Anhydrite, pyrrhotite, and sulfur-rich apatite: Tracing the sulfur evolution of an Oligocene andesite (Eagle Mountain, CO, USA). Lithos, 64, 63-75.

Patterson, D. B., Graham, I. J. 1988. Petrogenesis of andesitic lavas from Mangatepopo valley and Upper Tama lake, Tongariro volcanic centre, New Zealand. Journal of Volcanology and Geothermal Research, 35, 17-29.

Pearce, N. J. G., Westgate, J. A., Perkins, W. T. 1996. Developments in the analysis of volcanic glass shards by laser ablation ICP–MS: quantitative and single internal standard multi-element methods. Quaternary International, 34–36, 213–227.

Peng, G., Luhr, J. F., McGee, J. J. 1997. Factors controlling sulfur concentrations in volcanic apatite. American Mineralogist, 82, 1210-1224.

Perkins, W. T., Pearce, N. J. G. 1995. Mineral microanalysis by laserprobe inductively coupled plasma mass spectrometry. In: Potts, P. J., Bowles, J. F. W., Reed, S. J. B., Cave, M. R. (eds). Microprobe Techniques in the Earth Sciences. Mineralogical Society, London, Mineralogical Society Series, 6, 291-325.

Philippot, P., Agrinier, P., Scambelluri, M. 1998. Chlorine cycling during subduction of altered oceanic crust. Earth and Planetary Science Letters, 161, 33-44.

Piccoli, P., Candela, P. 1994. Apatite in felsic rocks: a model for the estimation of initial halogen concentrations in the Bishop Tuff (Long Valley) and Tuolumne Intrusive Suite (Sierra Nevada batholith) magmas. American Journal of Science, 294, 92-135.

Piccoli, P. M., Candela, P. A. 2002. Apatite in igneous systems. Reviews in Mineralogy and Geochemistry, 48, 255-292.

Potts, P. J., Tindle, A. G. 1989. Analytical characteristics of a multilayer dispersion element (2d = 60 Å) in the determination of fluorine in minerals by electron microprobe. Mineralogical Magazine, 53, 357-362.

Price, R. C., Gamble, J. A., Smith, I. E. M., Stewart, R. B., Eggins, S., Wright, I. C. 2005. An integrated model for the temporal evolution of andesites and rhyolites and crustal development in New Zealand's North Island. Journal of Volcanology and Geothermal Research, 140, 1-24.

Pyle, D. M., Mather, T. A. 2009. Halogens in igneous processes and their fluxes to the atmosphere and oceans from volcanic activity: A review. Chemical Geology, 263, 110-121.

Qin, Z., Lu, F., Anderson, A. T. 1992. Diffusive reequilibration of melt and fluid inclusions. American Mineralogist, 77, 565-576.

Ridolfi, F., Renzulli, A., Puerini, M. 2010. Stability and chemical equilibrium of amphibole in calc-alkaline magmas: an overview, new thermobarometric formulations and application to subduction-related volcanoes. Contributions to Mineralogy and Petrology, 160, 45-66.

Robock, A. 2000. Volcanic eruptions and climate. Reviews of Geophysics, 38, 191-219.

Rønsbo, J. G. 2008. Apatite in the Ilímaussaq alkaline complex: Occurrence, zonation and compositional variation. Lithos, 106, 71-82.

Rooyakkers, S. M., Wilson, C. J. N., Schipper, C. I., Barker, S. J., Allan, A. S. R. 2018. Textural and micro-analytical insights into mafic-felsic interactions during the Oruanui eruption, Taupo. Contributions to Mineralogy and Petrology, 175, 35.

Rowland, J. V., Sibson, R. H. 2001. Extensional fault kinematics within the Taupo Volcanic Zone, New Zealand: Soft-linked segmentation of a continental rift system. New Zealand Journal of Geology and Geophysics, 44, 271-283.

Rowland, J. V, Wilson, C. J. N., Gravley, D. M. 2010. Spatial and temporal variations in magma-assisted rifting, Taupo Volcanic Zone, New Zealand. Journal of Volcanology and Geothermal Research, 190, 89-108.

Rubin, A., Cooper, K. M., Leever, M., Wimpenny, J., Deering, C., Rooney, T., Gravley, D., Yin, Q. 2016. Changes in magma storage conditions following caldera collapse at Okataina Volcanic Center, New Zealand. Contributions to Mineralogy and Petrology, 171, 4.

Scaillet, B., Clemente, B., Evans, B. W., Pichavant, M. 1998. Redox control of sulfur degassing in silicic magmas. Journal of Geophysical Research, 103, 23937-23949.

Scambelluri, M., Müntener, O., Ottolini, L., Pettke, T. T., Vannucci, R. 2004. The fate of B, Cl and Li in the subducted oceanic mantle and in the antigorite breakdown fluids. Earth and Planetary Science Letters, 222, 217-234.

Scott, J. A. J., Humphreys, M. C. S., Mather, T. A., Pyle, D. M., Stock, M. J. 2015. Insights into the behaviour of S, F, and Cl at Santiaguito Volcano, Guatemala, from apatite and glass. Lithos, 232, 375-394.

Seebeck, H., Nicol, A., Villamor, P., Ristau, J., Pettinga, J. 2014. Structure and kinematics of the Taupo Rift, New Zealand. Tectonics, 33, 1178-1199.

Seifert, W., Kämpf, H., Wasternack, J. 2000. Compositional variation in apatite, phlogopite and other accessory minerals of the ultramafic Delitzsch complex, Germany: Implication for cooling history of carbonatites. Lithos, 53, 81-100.

Self, S. 1983. Large-scale phreatomagmatic silicic volcanism: A case study from New Zealand. Journal of Volcanology and Geothermal Research, 17, 433-469.

Self, S., Sparks, R. S. J. 1978. Characteristics of widespread pyroclastic deposits formed by the interaction of silicic magma and water. Bulletin Volcanologique, 41, 196-212.

Sha, L. K., Chappell, B. W. 1999. Apatite chemical composition, determined by electron microprobe and laser-ablation inductively coupled plasma mass spectrometry, as

a probe into granite petrogenesis. Geochimica et Cosmochimica Acta, 63, 3861-3881.

Shane, P., Smith, V. C., Nairn, I. 2008a. Millennial timescale resolution of rhyolite magma recharge at Tarawera volcano: Insights from quartz chemistry and melt inclusions. Contributions to Mineralogy and Petrology, 156, 397-411.

Shane, P., Nairn, I. A., Smith, V. C., Darragh, M., Beggs, K., Cole, J. W. 2008b. Silicic recharge of multiple rhyolite magmas by basaltic intrusion during the 22.6 ka Okareka Eruption Episode, New Zealand. Lithos, 103, 527-549.

Shane, P., Storm, S., Schmitt, A. K., Lindsay, J. M. 2012. Timing and conditions of formation of granitoid clasts erupted in recent pyroclastic deposits from Tarawera Volcano (New Zealand). Lithos, 140, 1-10.

Shishkina, T. A., Botcharnikov, R. E., Holtz, F., Almeev, R. R., Portnyagin, M. V. 2010. Solubility of H_2O- and CO_2-bearing fluids in tholeiitic basalts at pressures up to 500 MPa. Chemical Geology, 277, 115-125.

Sigl, M., McConnell, J. R., Layman, L., Maselli, O., McGwire, K., Pasteris, D., Dahl-Jensen, D., Steffensen, J. P., Vinther, B., Edwards, R., Mulvaney, R., Kipfstuhl, S. 2013. A new bipolar ice core record of volcanism from WAIS Divide and NEEM and implications for climate forcing of the last 2000 years. Journal of Geophysical Research: Atmospheres, 118, 1151-1169.

Sigl, M., Winstrup, M., McConnell, J. R., Welten, K. C., Plunkett, G., Ludlow, F., Büntgen, U., Caffee, M., Chellman, N., Dahl-Jensen, D., Fischer, H., Kipfstuhl, S., Kostick, C., Maselli, O. J., Mekhaldi, F., Mulvaney, R., Muscheler, R., Pasteris, D. R., Pilcher, J. R., Salzer, M., Schüpbach, S., Steffensen, J. P., Vinther, B. M., Woodruff, T. E. 2015. Timing and climate forcing of volcanic eruptions for the past 2,500 years. Nature, 523, 543-549.

Signorelli, S., Carroll, M. R. 2000. Solubility and fluid-melt partitioning of Cl in hydrous phonolitic melts. Geochimica et Cosmochimica Acta, 64, 2851-2862.

Sillitoe, R. H., Hedenquist, J. W. 2003. Linkages between volcanotectonic settings , ore-fluid compositions , and epithermal precious metal deposits. Society of Economic Geologists - Special Publication, 10, 315-343.

Sisson, T. W., Ratajeski, K., Hankins, W. B., Glazner, A. F. 2005. Voluminous granitic magmas from common basaltic sources. Contributions to Mineralogy and Petrology, 148, 635-661.

Sobolev, A. V. 1996. Melt inclusions in minerals as a source of principle petrological information. Petrology, 4, 209-220.

Stern, T., Benson, A. 2011. Wide-angle seismic imaging beneath an andesitic arc: Central North Island, New Zealand. Journal of Geophysical Research, 116, B09308.

Stock, M. J., Humphreys, M. C. S., Smith, V. C., Johnson, R. D., Pyle, D. M. 2015. New constraints on electron-beam induced halogen migration in apatite. American Mineralogist, 100, 281-293.

Stock, M. J., Humphreys, M. C. S., Smith, V. C., Isaia, R., Brooker, R. A., Pyle, D. M. 2018. Tracking volatile behaviour in sub-volcanic plumbing systems using apatite and glass: Insights into pre-eruptive processes at Campi Flegrei, Italy. Journal of Petrology, 59, 2463-2492.

Storm, S., Shane, P., Schmitt, A. K., Lindsay, J. M. 2011. Contrasting punctuated zircon growth in two syn-erupted rhyolite magmas from Tarawera volcano: Insights to crystal diversity in magmatic systems. Earth and Planetary Science Letters, 301, 511-520.

Storm, S., Shane, P., Schmitt, A. K., Lindsay, J. M. 2012. Decoupled crystallization and eruption histories of the rhyolite magmatic system at Tarawera volcano revealed by zircon ages and growth rates. Contributions to Mineralogy and Petrology, 163, 505-519.

Stormer, J. C., Pierson, M. L., Tacker, R. C. 1993. Variation of F and Cl X-ray intensity due to anisotropic diffusion in apatite during electron microprobe analysis. American Mineralogist, 78, 641-648.

Stratford, W. R., Stern, T. A. 2004. Strong seismic reflections and melts in the mantle of a continental back-arc basin. Geophysical Research Letters, 31, L06622.

Stratford, W. R., Stern, T. A. 2006. Crust and upper mantle structure of a continental backarc: Central North Island, New Zealand. Geophysical Journal International, 166, 469-484.

Straub, S. M., Layne, G. D. 2003. The systematics of chlorine, fluorine, and water in Izu arc front volcanic rocks: Implications for volatile recycling in subduction zones. Geochimica et Cosmochimica Acta, 67, 4179-4203.

Streck, M. J. 2014. Evaluation of crystal mush extraction models to explain crystal-poor rhyolites. Journal of Volcanology and Geothermal Research, 284, 79-94.

Streck, M. J., Dilles, J. H. 1998. Sulfur evolution of oxidized arc magmas as recorded in apatite from a porphyry copper batholith. Geology, 26, 523-526.

Streck, M. J., Grunder, A. L. 2008. Phenocryst-poor rhyolites of bimodal, tholeiitic provinces: The Rattlesnake Tuff and implications for mush extraction models. Bulletin of Volcanology, 70, 385-401.

Sun, W., Arculus, R. J., Kamenetsky, V. S., Binns, R. A. 2004. Release of gold-bearing fluids in convergence margin magmas prompted by magnetite crystallization. Nature, 431, 975-978.

Sutton, A. N., Blake, S., Wilson, C. J. N. 1995. An outline geochemistry of rhyolite eruptives from Taupo volcanic centre, New Zealand. Journal of Volcanology and Geothermal Research, 68, 153-175.

Sutton, A. N., Blake, S., Wilson, C. J. N., Charlier, B. L. A. 2000. Late Quaternary evolution of a hyperactive rhyolite magmatic system: Taupo volcanic centre, New Zealand. Journal of the Geological Society, London, 157, 537-552.

Urann, B. M., Le Roux, V., Hammond, K., Marschall, H. R., Lee, C. T. A., Monteleone, B. D. 2017. Fluorine and chlorine in mantle minerals and the halogen budget of the Earth's mantle. Contributions to Mineralogy and Petrology, 172, 51.

Van den Bleeken, G., Koga, K. T., 2015. Experimentally determined distribution of fluorine and chlorine upon hydrous slab melting, and implications for F–Cl cycling through subduction zones. Geochimica et Cosmochimica Acta, 171, 353-373.

Van Eaton, A. R., Wilson, C. J. N. 2013. The nature, origins and distribution of ash aggregates in a large-scale wet eruption deposit: Oruanui, New Zealand. Journal of Volcanology and Geothermal Research, 250, 129-154.

Van Eaton, A. R., Herzog, M., Wilson, C. J. N., McGregor, J. 2012. Ascent dynamics of large phreatomagmatic eruption clouds: The role of microphysics. Journal of Geophysical Research, 117, B03203.

Vigneresse, J. L., Barbey, P., Cuney, M. 1996. Rheological transitions during partial melting and crystallization with application to felsic magma segregation and transfer. Journal of Petrology, 37, 1579-1600.

Villamor, P., Berryman, K. 2001. A late Quaternary extension rate in the Taupo Volcanic Zone, New Zealand, derived from fault slip data. New Zealand Journal of Geology and Geophysics, 44, 243-269.

Wallace, L. M., Beavan, J., McCaffrey, R., Darby, D. 2004. Subduction zone coupling and tectonic block rotations in the North Island, New Zealand. Journal of Geophysical Research, 109, B12406.

Wallace, P. J. 2005. Volatiles in subduction zone magmas: Concentrations and fluxes based on melt inclusion and volcanic gas data. Journal of Volcanology and Geothermal Research, 140, 217-240.

Wallace, P. J., Edmonds, M. 2011. The sulfur budget in magmas: evidence from melt inclusions, submarine glasses, and volcanic gas emissions. Reviews in Mineralogy and Geochemistry, 73, 215-246.

Watson, E. B. 1979. Apatite saturation in basic to intermediate magmas. Geophysical Research Letters, 6, 937-940.

Webster, J. D. 1990. Partitioning of F between H_2O and CO_2 fluids and topaz rhyolite melt. Contributions to Mineralogy and Petrology, 104, 424-438.

Webster, J. D. 1997. Chloride solubility in felsic melts and the role of chloride in magmatic degassing. Journal of Petrology, 38, 1793-1807.

Webster, J. D. 2004. The exsolution of magmatic hydrosaline chloride liquids. Chemical Geology, 210, 33-48.

Webster, J. D., Botcharnikov, R. E. 2011. Distribution of sulfur between melt and fluid in S-O-H-C-Cl-bearing magmatic systems at shallow crustal pressures and temperatures. Reviews in Mineralogy and Geochemistry, 73, 247-283.

Webster, J. D., Holloway, J. R. 1990. Partitioning of F and Cl between magmatic hydrothermal fluids and highly evolved granitic magmas. Geological Society of America Special Papers, 246, 21-34.

Webster, J. D., Piccoli, P. M. 2015. Magmatic apatite: A powerful, yet deceptive, mineral. Elements, 11, 177-182.

Webster, J. D., Kinzler, R. J., Mathez, E. A. 1999. Chloride and water solubility in basalt and andesite melts and implications for magmatic degassing. Geochimica et Cosmochimica Acta, 63, 729-738.

Webster, J. D., Tappen, C. M., Mandeville, C. W. 2009. Partitioning behavior of chlorine and fluorine in the system apatite-melt-fluid. II: Felsic silicate systems at 200 MPa. Geochimica et Cosmochimica Acta, 73, 559-581.

Webster, J. D., Vetere, F., Botcharnikov, R. E., Goldoff, B., McBirney, A., Doherty, A. L. 2015. Experimental and modeled chlorine solubilities in aluminosilicate melts at 1

to 7000 bars and 700 to 1250 °C: Applications to magmas of Augustine Volcano, Alaska. American Mineralogist, 100, 522-535.

Webster, J. D., Goldoff, B. A., Flesch, R. N., Nadeau, P. A., Silbert, Z. W. 2017. Hydroxyl, Cl, and F partitioning between high-silica rhyolitic melts-apatite-fluid(s) at 50-200 MPa and 700-1000 °C. American Mineralogist, 102, 61-74.

Wendlandt, R. F. 1982. Sulfide saturation of basalt and andesite melts at high pressures and temperatures. American Mineralogist, 67, 877-885.

Westrich, H. R., Gerlach, T. M. 1992. Magmatic gas source for the stratospheric SO_2 cloud from the June 15, 1991, eruption of Mount Pinatubo. Geology, 20, 867-870.

Whittington, A. G., Hellwig, B. M., Behrens, H., Joachim, B., Stechern, A., Vetere, F. 2009. The viscosity of hydrous dacitic liquids: Implications for the rheology of evolving silicic magmas. Bulletin of Volcanology, 71, 185-199.

Wilke, M., Klimm, K., Kohn, S. C. 2011. Spectroscopic studies on sulfur speciation in synthetic and natural glasses. Reviews in Mineralogy and Geochemistry, 73, 41-78.

Wilson, C. J. N. 1993. Stratigraphy, chronology, styles and dynamics of late Quaternary eruptions from Taupo Volcano, New Zealand. Philosophical Transactions of the Royal Society of London, A343, 205-306.

Wilson, C. J. N. 2001. The 26.5 ka Oruanui eruption, New Zealand: An introduction and overview. Journal of Volcanology and Geothermal Research, 112, 133-174.

Wilson, C. J. N., Charlier, B. L. A. 2009. Rapid rates of magma generation at contemporaneous magma systems, Taupo volcano, New Zealand: Insights from U-Th model-age spectra in zircons. Journal of Petrology, 50, 875-907.

Wilson, C. J. N., Rowland, J. V. 2016. The volcanic, magmatic and tectonic setting of the Taupo Volcanic Zone, New Zealand, reviewed from a geothermal perspective. Geothermics, 59, 168-187.

Wilson, C. J. N., Rogan, A. M., Smith, I. E. M., Northey, D. J., Nairn, I. A., Houghton, B. F. 1984. Caldera volcanoes of the Taupo Volcanic Zone, New Zealand. Journal of Geophysical Research, 89, 8463-8484.

Wilson, C. J. N., Houghton, B. F., McWilliams, M. O., Lanphere, M. A., Weaver, S. D., Briggs, R. M. 1995. Volcanic and structural evolution of Taupo Volcanic Zone, New-Zealand: a review. Journal of Volcanology and Geothermal Research, 68, 1-28.

Wilson, C. J. N., Blake, S., Charlier, B. L. A., Sutton, A. N. 2006. The 26.5 ka Oruanui eruption, Taupo Volcano, New Zealand: Development, characteristics and evacuation of a large rhyolitic magma body. Journal of Petrology, 47, 35-69.

Wilson, C. J. N., Gravley, D. M., Leonard, G. S., Rowland, J. V. 2009. Volcanism in the central Taupo Volcanic Zone, New Zealand: tempo, styles, and controls. In: Thordarson, T., Self, S., Larsen, G., Rowland, S. K., Höskuldsso, A. (eds.). Studies in Volcanology: The Legacy of George Walker, IAVCEI Proceedings in Volcanology, 2, 225-247.

Wilson, C. J. N., Seward, T. M., Charlier, B. L. A., Allan, A. S. R., Bello, L.. 2012. A comment on: 'TitaniQ under pressure: the effect of pressure and temperature on the solubility of Ti in quartz', by Jay B. Thomas, E. Bruce Watson, Frank S. Spear, Philip T. Shemella, Saroj K. Nayak and Antonio Lanzirotti. Contributions to Mineralogy and Petrology 164, 359-368.

Witter, J. B., Kuehner, S. M. 2004. A simple empirical method for high-quality electron microprobe analysis of fluorine at trace levels in Fe-bearing minerals and glasses. American Mineralogist, 89, 57-63.

Wood, B. J., Banno, S. 1973. Garnet-orthopyroxene and orthopyroxene-clinopyroxene relationships in simple and complex systems. Contributions to Mineralogy and Petrology, 42, 109-124.

Woodhead, J. D., Harmon, R. S., Fraser, D. G. 1987. O, S, Sr, and Pb isotope variations in volcanic rocks from the Northern Mariana Islands: implications for crustal recycling in intra-oceanic arcs. Earth and Planetary Science Letters, 83, 39-52.

Zajacz, Z., Candela, P. A., Piccoli, P. M., Sanchez-Valle, C. 2012. The partitioning of sulfur and chlorine between andesite melts and magmatic volatiles and the exchange coefficients of major cations. Geochimica et Cosmochimica Acta, 89, 81-101.

Zhang, C., Koepke, J., Wang, L. X., Wolff, P. E., Wilke, S., Stechern, A., Almeev, R., Holtz, F. 2016. A practical method for accurate measurement of trace level fluorine in Mg- and Fe-bearing minerals and glasses using electron probe microanalysis. Geostandards and Geoanalytical Research, 40, 351-363.

Zhu, C., Sverjensky, D. A. 1991. Partitioning of F-Cl-OH between minerals and hydrothermal fluids. Geochimica et Cosmochimica Acta, 55, 1837-1858.

7. Appendix 1 – Tables: analytical standards and uncertainties

Table A1.1a. Summary of EPMA data acquired for international glass standard VG-568 USNM 72854. All major oxide values are given in wt%, and all volatile elements are given in ppm. Preferred values are from Jarosweich et al. (1980).

	VG-568 (rhyolitic glass)						
	n = 63						
	Average	**Minimum**	**Maximum**	**2sd**	**%2sd**	**Preferred***	**% diff**
SiO_2	77.34	76.78	78.28	0.65	0.8	76.96	0.50
TiO_2	0.07	0.04	0.10	0.03	37.9	12.17	-13.35
Al_2O_3	12.33	12.08	12.67	0.29	2.4	0.08	1.33
FeO	1.08	0.83	1.31	0.20	18.4	1.08	0.19
MnO	0.02	0.00	0.06	0.03	130.6	0.02	13.80
MgO	0.03	0.00	0.06	0.02	74.6	0.03	-1.67
CaO	0.46	0.41	0.49	0.04	8.4	0.45	1.13
Na_2O	3.49	2.52	3.85	0.50	14.4	3.52	-0.73
K_2O	4.92	4.68	5.09	0.22	4.4	4.93	-0.29
Cr_2O_3	0.01	0.00	0.04	0.02	289.3	-	-
S	33	12	61	25	75.3	20	65.67
F	1610	1303	2022	398	24.7	1400	15.03
Cl	1090	945	1219	131	12.0	1013	7.65
Total	100.02					99.483	

Table A1.1b. Summary of EPMA data acquired for microbeam mineral standard Elba Pyrite. Sulfur and metal values are given in wt%.

	Elba Pyrite						
	n = 5						
	Average	**Minimum**	**Maximum**	**2sd**	**%2sd**	**Preferred**	**% diff**
Cu	0.01	0.00	0.03	0.02	194.81	0	-
V	0.01	0.00	0.03	0.02	173.97	0	-
Co	0.55	0.00	1.67	1.22	221.65	0	-
Si	0.00	0.00	0.01	0.01	309.84	0	-
Ni	0.03	0.00	0.07	0.06	223.74	0	-
Fe	46.98	46.46	47.57	0.85	1.81	46.55	0.92
S	53.82	53.57	54.00	0.32	0.59	53.45	0.69
Cr	0.03	0.00	0.07	0.05	189.21	0	-
Mn	0.01	0.00	0.04	0.03	236.32	0	-
Total	101.44					100	

Table A1.1c. Summary of EPMA data acquired for international mineral standard Durango Apatite USNM 104021. All major oxide, F and Cl values are given in wt%, and S^{6+} values are given in ppm. Preferred values are from Yang et al. (2014).

	Durango Apatite						
	n = 35						
	Average	**Minimum**	**Maximum**	**2sd**	**%2sd**	**Preferred**	**% diff**
CaO	54.37	53.53	54.82	0.67	1.23	53.9	0.86
F	3.97	3.58	4.48	0.46	11.65	3.71	6.97
P_2O_5	40.31	39.69	41.13	0.70	1.75	41.88	-3.74
Cl	0.42	0.35	0.47	0.07	15.78	0.41	2.46
S^{6+}	1679	957	2106	673	249	1482	13.30
Total	99.49					100.27	

Table A1.1d. Summary of EPMA data acquired for international mineral standard VG-A99 USNM 113498/1. All major oxide values are given in wt%, and all volatile element values are given in ppm. Preferred values are from Jarosweich et al. (1980).

	VG-A99 (basaltic glass)						
	n = 70						
	Average	**Minimum**	**Maximum**	**2sd**	**%2sd**	**Preferred**	**% diff**
SiO_2	50.70	50.00	51.12	0.47	0.9	51.15	-0.87
TiO_2	4.01	3.85	4.10	0.11	2.7	4.105	-2.35
Al_2O_3	12.42	12.19	12.81	0.27	2.1	12.38	0.30
FeO	13.31	12.48	14.56	0.85	6.4	13.345	-0.28
MnO	0.17	0.12	0.23	0.05	29.5	0.2	-12.75
MgO	5.09	4.83	5.36	0.22	4.4	5.07	0.32
CaO	9.25	9.01	9.40	0.15	1.6	9.26	-0.14
Na_2O	2.55	2.31	2.78	0.20	7.9	2.68	-4.82
K_2O	0.85	0.79	0.92	0.05	6.1	0.831	2.77
Cr_2O_3	0.01	0.00	0.06	0.03	257.4	0.015	-20.67
S	167	113	240	45	26.8	160	4.41
F	506	333	700	175	34.5	-	-
Cl	259	226	304	37	14.2	205	26.29
Total	98.45					99.07	

Table A1.1e. Summary of EPMA data acquired for international mineral standard Johnstown Meteorite Hypersthene USNM 746. All major oxide values are given in wt%. Preferred values are from Jarosweich et al. (1980)

	Johnstown Meteorite (hypersthene)						
	n = 45						
	Average	**Minimum**	**Maximum**	**2sd**	**%2sd**	**Preferred**	**% diff**
SiO_2	54.10	53.71	54.50	0.41	0.8	54.09	0.01
CaO	1.51	1.44	1.60	0.09	6.0	1.52	-0.61
Na_2O	0.05	0.00	0.10	0.06	115.3	0.05	0.41
Al_2O_3	1.23	1.15	1.31	0.08	6.8	1.23	0.13
MgO	26.82	26.62	27.00	0.23	0.9	26.79	0.10
FeO	15.22	14.41	15.66	0.74	4.8	15.22	0.02
TiO_2	0.16	0.04	0.26	0.13	81.0	0.16	0.68
MnO	0.49	0.45	0.52	0.04	7.6	0.49	0.03
Cr_2O_3	0.75	0.70	0.82	0.06	8.3	0.75	-0.01
Total	100.33					100.30	

Table A1.1f. Summary of EPMA data acquired for international mineral standard Indian Ocean (IO) Basalt NMNH 113716-1. All major oxide values are given in wt%, and all volatile elements are given in ppm. Preferred values are from Jarosewich et al. (1980).

	Indian Ocean (basaltic glass)						
	n = 57						
	Average	**Minimum**	**Maximum**	**2sd**	**%2sd**	**Preferred**	**% diff**
SiO_2	51.39	50.61	51.98	0.54	1.1	51.52	-0.25
TiO_2	1.29	1.15	1.45	0.09	7.3	1.30	-0.98
Al_2O_3	15.24	14.91	15.97	0.43	2.8	15.39	-0.96
FeO	8.98	8.25	11.31	0.85	9.4	9.13	-1.66
MnO	0.16	0.11	0.21	0.04	28.4	0.17	-8.42
MgO	8.13	6.99	8.86	0.68	8.4	8.21	-0.97
CaO	11.43	10.82	12.46	0.48	4.2	11.31	1.03
Na_2O	2.51	1.54	2.91	0.39	15.4	2.48	1.21
K_2O	0.08	0.05	0.11	0.03	36.1	0.09	-10.82
Cr_2O_3	0.04	0.00	0.08	0.04	90.6	-	-
S	1107	956	1278	104	9.4	1200	-7.78
F	412	234	562	133	32.4	-	-
Cl	54	11	292	82	151.8	-	-
Total	99.40					99.17	

Table A1.2a. Summary of LA-ICP-MS data acquired for international glass standard NIST SRM610. All values are given in wt%. Preferred values are compiled from the GeoRem online database.

	NIST SRM610 (rhyolitic glass)						
	n = 9						
	Average	**Minimum**	**Maximum**	**2sd**	**%2sd**	**Preferred**	**% diff**
Li	458.90	429.90	492.60	51.62	11.2	468	-1.9
Sc	452.10	442.00	466.90	21.39	4.7	455	-0.6
Ti	446.14	412.50	509.30	69.62	15.6	452	-1.3
V	487.00	449.00	526.00	62.89	12.9	450	8.2
Cr	407.86	399.20	422.90	16.76	4.1	408	0.0
Mn	418.68	406.40	429.30	15.31	3.7	444	-5.7
Co	408.58	395.50	434.90	27.39	6.7	410	-0.3
Ni	440.50	410.60	496.20	61.70	14.0	458.7	-4.0
Cu	396.20	358.60	440.00	67.04	16.9	441	-10.2
Zn	471.56	445.00	497.00	44.06	9.3	460	2.5
Ga	428.53	422.60	440.00	16.22	3.8	433	-1.0
Se	151.00	118.00	168.00	46.68	30.9	138	9.4
Rb	430.90	420.70	439.00	15.23	3.5	425.7	1.2
Sr	544.00	514.00	560.00	42.46	7.8	515.5	5.5
Y	455.00	446.00	466.00	16.57	3.6	462	-1.5
Zr	432.28	419.90	469.40	37.30	8.6	448	-3.5
Nb	457.00	417.00	500.00	67.90	14.9	465	-1.7
Mo	436.67	435.00	439.00	3.40	0.8	417	4.7
Cs	365.10	355.00	377.00	18.14	5.0	366	-0.2
Ba	471.33	446.00	501.00	45.32	9.6	452	4.3
La	449.67	444.00	457.00	10.87	2.4	440	2.2
Ce	455.00	444.30	485.40	30.94	6.8	453	0.4
Pr	403.33	345.00	456.00	90.98	22.6	448	-10.0
Nd	416.33	374.00	475.00	85.64	20.6	430	-3.2
Sm	443.67	422.00	479.00	50.39	11.4	453	-2.1
Eu	438.94	426.30	455.00	19.47	4.4	447	-1.8
Gd	430.93	420.80	437.00	14.42	3.3	449	-4.0
Tb	449.03	422.10	497.00	68.01	15.1	437	2.8
Dy	462.33	449.00	488.00	36.31	7.9	437	5.8
Ho	429.33	383.00	464.00	68.16	15.9	449	-4.4
Er	418.40	343.00	491.00	120.91	28.9	455	-8.0
Tm	415.00	385.00	469.00	76.52	18.4	435	-4.6
Yb	440.67	413.00	468.00	44.91	10.2	450	-2.1
Lu	434.47	419.00	453.00	28.10	6.5	439	-1.0
Hf	396.27	394.00	397.80	3.27	0.8	435	-8.9
Ta	448.94	405.80	521.50	84.84	18.9	446	0.7
W	493.00	471.00	535.00	59.42	12.1	444	11.0
Pb	428.06	413.60	438.30	22.15	5.2	426	0.5
Th	452.42	442.90	466.50	16.50	3.6	457.2	-1.0
U	447.06	423.10	496.80	53.48	12.0	461.5	-3.1

Table A1.2b. Summary of LA-ICP-MS data acquired for international glass standard NIST SRM612. All values are given in wt%. Preferred values are compiled from the GeoRem online database.

	NIST SRM612 (rhyolitic glass)						
	n = 9						
	Average	**Minimum**	**Maximum**	**2sd**	**%2sd**	**Preferred**	**% diff**
Li	41.86	40.20	42.89	2.08	5.0	40.2	4.0
Sc	40.69	39.80	41.54	1.35	3.3	39.9	1.9
Ti	43.98	42.80	45.90	2.13	4.8	44	0.0
V	39.07	38.47	40.01	1.09	2.8	38.8	0.7
Cr	36.22	34.70	38.40	2.64	7.3	36.4	-0.5
Mn	37.94	36.70	39.30	1.90	5.0	38.7	-2.0
Co	35.39	34.26	36.80	1.93	5.4	35.5	-0.3
Ni	38.83	37.81	39.70	1.27	3.3	38.8	0.1
Cu	37.53	36.26	39.50	2.43	6.5	37.8	-0.7
Zn	38.35	36.00	40.00	3.18	8.3	39.1	-2.0
Ga	36.48	34.97	37.90	2.14	5.9	36.9	-1.2
Se	13.43	10.90	15.90	3.57	26.6	16.3	-21.4
Rb	31.43	30.72	32.43	1.19	3.8	31.4	0.1
Sr	78.18	77.00	79.60	2.13	2.7	78.4	-0.3
Y	38.58	37.10	40.50	2.50	6.5	38.3	0.7
Zr	37.85	36.87	38.62	1.51	4.0	37.9	-0.1
Nb	40.11	38.20	42.10	2.78	6.9	38.9	3.0
Mo	37.90	37.00	38.95	1.41	3.7	37.4	1.3
Cs	41.92	41.40	42.30	0.65	1.6	42.7	-1.9
Ba	39.78	38.50	41.00	1.90	4.8	39.3	1.2
La	36.13	34.60	38.00	2.44	6.8	36	0.3
Ce	38.52	37.62	39.24	1.44	3.7	38.4	0.3
Pr	37.58	36.28	39.20	2.14	5.7	37.9	-0.9
Nd	35.97	34.90	37.70	1.91	5.3	35.5	1.3
Sm	38.10	35.80	40.50	3.38	8.9	37.7	1.1
Eu	35.02	34.25	35.52	0.90	2.6	35.6	-1.7
Gd	36.63	35.70	37.40	1.22	3.3	37.3	-1.8
Tb	36.24	34.91	37.80	2.19	6.0	37.6	-3.8
Dy	35.98	35.23	37.09	1.35	3.8	35.5	1.3
Ho	38.30	36.70	39.90	2.33	6.1	38.3	0.0
Er	37.80	36.40	38.81	1.88	5.0	38	-0.5
Tm	38.31	36.80	40.40	2.65	6.9	36.8	3.9
Yb	39.03	36.80	40.40	2.76	7.1	39.2	-0.4
Lu	37.04	36.20	38.10	1.36	3.7	37	0.1
Hf	34.98	34.30	35.80	1.21	3.5	36.7	-4.9
Ta	39.93	38.20	41.60	2.41	6.0	37.6	5.8
W	39.70	38.20	41.19	2.10	5.3	38	4.3
Pb	38.57	37.82	39.75	1.38	3.6	38.57	0.0
Th	37.83	35.90	39.40	2.54	6.7	37.79	0.1
U	37.20	36.00	38.13	1.63	4.4	37.38	-0.5

8. Appendix 2 – EPMA analytical techniques

A2.1 Rhyolite glass analysis procedure

Unless specified otherwise, the analytical conditions for glass analysis were 15 kV, 8 nA, 5 mm upper and lower from peak, with a 10 µm circular beam. To minimise Na loss the peak search was skipped and count times were shorter at 10 s peak and 5 s background.

A2.1.1 Primary standards

1) VG658 was used to calibrate for the following elements, on the corresponding channels and crystals: Na channel 2 TAP, Si and Al on channel 3 TAP, K on channel 4 PETJ. The elements were analysed at 30 s peak and 15 s background times, under default conditions and a narrow peak search.
2) VG568 was used to re-calibrate for Na to mitigate time-dependent element migration during electron bombardment (Gedeon et al., 2000, and references therein): Na channel 2 TAP. 10 s peak and 5 s background times were used, under default conditions and skipping the peak search.
3) VGA99 was used to calibrate for the following elements, on the corresponding channels and crystals: Ca channel 1 PETL, Mg channel 2 Tap, Fe channel 4 LIF. The elements were analysed at 30 s peak and 15 s background times, under default conditions and a narrow peak search.
4) A synthetic TiO_2 standard was used to calibrate Ti on channel 1 PETL, with 30 s peak and 15 s background times, under default conditions and a narrow peak search.
5) A synthetic MnO standard was used to calibrate Mn on channel 5 LIFL, with 30 s peak and 15 s background times, under default conditions and a narrow peak search.

6) A synthetic Cr_2O_3 standard was used to calibrate Cr on channel 5 LIFL, with 30 s peak and 15 s background times, under default conditions and a narrow peak search.
7) Elba Pyrite was used to calibrate for S on channel 1 PETL, with 10 s peak and 5 s background, under default conditions and a narrow peak search. The current was set to 60 nA.
8) VG568 was used to calibrate F and Cl under the following conditions: F channel 2 LDE1, 120 s peak and 60 s background, with 4 mm upper distance from the peak and 0 mm lower. The peak search was skipped, and the following conditions specified after Witter and Kuehner (2004): peak position = 87.007, gain = 4, Hv[V] = 1830, base level [V] = 0.5, window [V] = 3.00, diff. Cl was analysed on both channels 4 and 5 on the PETF and PETL crystals respectively, with 60 s peak and 30 s background search, under default conditions and a narrow peak search. The current was set to 60 nA.

A2.1.2 Major element run

All elements apart from Na were run under the same conditions as stated for the primary standardisation. Na was analysed with 10 s peak and 5 s background times, and skipping the peak search with the following specified conditions: peak position = 129.512, gain = 32, Hv[V] = 1700, base level [V] = 0.7, window [V] = 9.3, diff. VG568, VGA99, IO, and VG2 glass standards were run as secondary standards throughout the analysis to monitor any potential EPMA beam drift. The glass standards DR-N, GS-N, and AC-E (diorite, granite, and granite respectively) synthesised by Zhang et al. (2016) were also run as secondary standards at the end of the run.

A2.1.3 Volatile element run

All elements were run on the same channels and crystals as stated for the primary standardisation. The peak times were as follows: for sulfur - 60 s peak and 30 s background times; for fluorine - 120 s peak and 60 s background times. The peak

search was skipped, and the same conditions as previously stated following Witter and Kuehner (2004) were specified: peak position = 87.007, gain = 4, Hv[V] = 1830, base level [V] = 0.5, window [V] = 3.00, diff. Cl 60 s peak and 30 s background search. The current was set to 60 nA.

VG568, VGA99, IO, and VG2 glass standards were run as secondary standards throughout the analysis to monitor any potential EPMA beam drift. The glass standards DR-N, GS-N, and AC-E (diorite, granite, and granite respectively) synthesised by Zhang et al. (2016) were also run as secondary standards at the end of the run.

A2.1.4 Fluorine correction standards

Due to the interference of the Fe-induced X-ray lines, a suite of secondary standards with known Fe and F values is used to correct the raw data from the EPMA (Zhang et al., 2016). Ferrobasalt, high-Mg Basalt, Andesite, MORB, Rhyodacite, and Rhyolite standards synthesised by Zhang et al. (2016) were run. The elements and conditions are the same as in section A2.1.3.

A2.2 Basaltic glass analysis procedure

For basaltic glass EPMA analysis the same procedure as that for analysing rhyolite glass in section A2.1 was undertaken, with the exception of omitting VG568 as a secondary standard, and with the following amendments to primary standard calibration:

1) VG658 was used to calibrate for the following elements, on the corresponding channels and crystals: Na channel 2 TAP, K on channel 4 PETJ. The elements were analysed at 30 s peak and 15 s background times, under default conditions and a narrow peak search.
2) VG568 was used to re-calibrate for Na to mitigate time-dependent element migration during electron bombardment (Gedeon et al., 2000, and references therein): Na channel 2 TAP. 10 s peak and 5 s background times were used, under default conditions and skipping the peak search.

3) VGA99 was used to calibrate for the following elements, on the corresponding channels and crystals: Ca channel 1 PETL, Mg channel 2 TAP, Si and Al on channel 3 TAP, Fe channel 4 LIF. The elements were analysed at 30 s peak and 15 s background times, under default conditions and a narrow peak search.

A2.3 Orthopyroxene analysis procedure

Orthopyroxene analyses were conducted around the analysed melt inclusions, and at crystal rims and interiors (Figure 2.2). The analytical conditions for the primary standards and the unknown crystals were the same; 12 nA, 15 kV, spot beam, 30 s peak and 15 s background, default conditions and a narrow peak search.

A2.3.1 Primary standards

1. Johnstown Meteorite Hypersthene was used to calibrate for the following elements, on the corresponding channels and crystals: Mg on channel 2 TAP, Si and Al on channel 3 TAP, Fe on channel 4 LIF.
2. Kakanui Augite was used to calibrate for the following elements, on the corresponding channels and crystals: Ca on channel 1 PETL, Na and Mg channel 2 TAP, Si and Al channel 3 TAP, Fe on channel 4 LIF.
3. Orthoclase Or-1A was used to calibrate for K on channel 4 PETJ.
4. A synthetic TiO_2 standard was used to calibrate Ti on channel 1 PETL.
5. A synthetic MnO was used to calibrate Mn on channel 5 LIFL.
6. A synthetic Cr_2O_3 was used to calibrate Cr on channel 5 LIFL.

A2.3.2 Orthopyroxene analysis

All elements were run under the same conditions as stated for the primary standardisation.

Hypersthene and Kakanui Augite standards were run as secondary standards throughout the analysis to monitor any EPMA current drift.

A2.4 Apatite analysis procedure

The analytical conditions (besides peak search times) for the primary standards and the unknown crystals were the same; 4 nA, 10 kV, 10 µm beam, default conditions and a narrow peak search. Peak search times are specified in the following text.

A2.4.1 Primary standards

1. Durango apatite was used to calibrate for the following elements, at the corresponding channels, crystals, and peak search times: Ca on channel 1 PETL with 10 s peak and 5 s background searches, F on channel 2 LDE1 with 10 s peak and 5 s background searches, P on channel 3 TAP with 10 s peak and 5 s background searches, Cl on channel 5 PETL with 10 s peak and 5 s background searches.
2. Celestine was used to calibrate for S on channel 4 PETJ with 10 s peak and 5 s background searches.

A2.4.2 Apatite analysis

All elements were run on the same channels and crystals as stated for the primary standardisation. The peak times were as follows: Ca 30 s peak and 15 s background search, F 60 s peak and 15 s background search, P 30 s peak and 15 s background search, S 60 s peak and 15 s background search, Cl analysed on channel 5 PETL, 60 s peak and 15 s background search. Durango and Beeson standards were run as secondary standards throughout the analysis to monitor any EPMA current drift.

A2.5 Pyrrhotite analysis procedure

The analytical conditions for the primary standards and the unknown crystals were the same; 60 nA, 15 kV, 1 µm beam, 30 s peak and 15 s background, default conditions and a narrow peak search (Liu et al., 2018).

A2.5.1 Primary standards

1. Cu metal standard was used to standardise for Cu: channel 1 LIFL
2. V metal standard was used to standardise for V: channel 1 PETL.
3. Co metal standard was used to standardise for Co: channel 3 TAP.
4. A synthetic SiO_2 standard was used to standardise for Si: channel 3 TAP.
5. Ni metal standard was used to standardise for Ni: channel 4 LIF.
6. Elba Pyrite was used to standardise for the following elements, on the corresponding channels and crystals: Fe on channel 4 LIF, S on channel 4 PETJ.
7. A synthetic Cr_2O_3 standard was used to standardise for Cr: channel 4 LIF.
8. A synthetic MnO standard was used to standardise for Mn: channel 5 LIFL.

A2.5.2 Pyrrhotite analysis

All elements were run under the same conditions as stated for the primary standardisation. Elba Pyrite was run as a secondary standard throughout the analysis to monitor any EPMA current drift.

A2.6 Glass fluorine correction

The determination of accurate F levels in magmatic samples is difficult. The standard TAP analytical crystal has an interplanar spacing of 12.95 Å, which results in a high detection limit and large analytical errors when measuring F due to the low count rate for FKα X-rays (Zhang et al., 2016). With the use of a different pseudocrystal, LDE1, which has a far greater interplanar spacing of 30 Å, higher count rates (by a factor of

30 for F analyses) for low atomic-number elements can be achieved (Anzelmo and Boyer, 1986; Witter and Kuehner, 2004; Zhang et al., 2016). Use of the LDE1 pseudocrystal does add a complication, which has to be accounted for through an extra suite of analyses. Small but significant spectral interferences occur between the F*Kα* peak and the Fe- and Mg-induced X-ray lines (Donovan et al., 1992; Witter and Kuehner, 2004; Zhang et al., 2016). The first order FeLα line overlaps the F*Kα* peak position, and the second order Mg*K*β line overlaps the at the F*Kα* right-side background position. These peak interferences cannot be ignored when analysing F in Fe- and Mg-bearing samples, such as glass inclusions, and must be eliminated or accounted for.

A2.6.1 Mg interference elimination

X-ray lines with similar wavelengths but differing energies can be removed through modifying the pulse height analysis (PHA) conditions. Thus the competing effects from the Mg X-ray line were mitigated by pre-setting the PHA to the following conditions: Differential mode, peak position = 87.007, gain = 4, base level = 0.5v, window = 3v, bias = 1830v.

A2.6.2 Fe interference calibration

The overlap of the Fe peak cannot be removed through alteration of PHA conditions (Figure A2.1). Thus the interference has to be quantitatively calibrated in terms of total FeO, in order to accurately measure the F*Kα* signal. For a complete explanation of Fe overlap quantification, refer to Zhang et al. (2016).

A2.6.3 F interference correction

Using the procedure outlined in Zhang et al. (2016), the raw data acquired from the EPMA can be corrected, producing results that give accurate F abundances. For an

overview of the Fe-bearing F-free standards used for the Fe overlap calibration, and of the Fe-bearing F-known standards used as secondary standards, refer to Zhang et al. (2016).

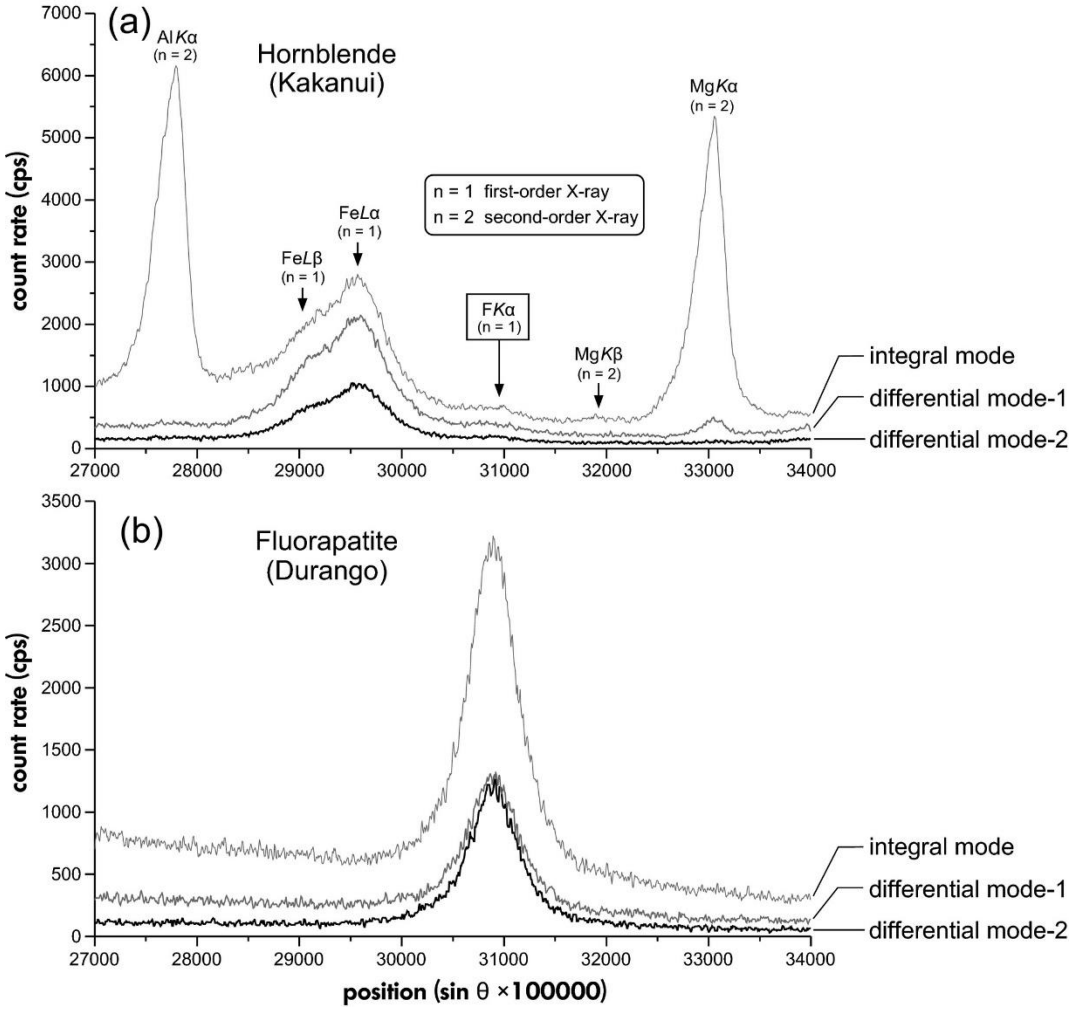

Figure A2. 1. Spectral scans for two EPMA standards with varying pulse height analysis (PHA) settings. a) Hornblende Kakanui standard (USNM 143965). b) Fluorapatite Durango (USNM 104021). Changing the PHA conditions removes the interference on F*K*α from the Mg*K*β line, and lessens the interference from the Fe*L*α line (a), without depressing F*K*α (b). Sourced from Zhang et al. (2016).

9. Appendices references

Anzelmo, J. A., Boyer, B. W. 1986. The analysis of carbon and other light elements using layered synthetic microstructures. Advances in X-ray Analysis, 30, 193-200.

Donovan, J. J., Snyder, D. A., Rivers, M. L. 1992. An improved interference correction for trace element analysis. Microbeam Analysis, 2, 23-28.

Gedeon, O., Hulínský, V., Jurek, K. 2000. Microanalysis of glass containing alkali ions. Mikrochimica Acta, 132, 505-510.

Jarosewich, E., Nelen, J. A., Norberg, J. A. 1980. Reference samples for electron microprobe analysis. Geostandards Newsletter, 4, 43-47.

Liu, Z., Shao, Y., Zhou, H., Liu, N., Huang, K., Liu, Q., Zhang, J., Wang, C. 2018. Major and trace element geochemistry of pyrite and pyrrhotite from stratiform and lamellar orebodies: Implications for the ore genesis of the Dongguashan copper (gold) deposit, Eastern China. Minerals, 8, 380.

Witter, J. B., Kuehner, S. M. 2004. A simple empirical method for high-quality electron microprobe analysis of fluorine at trace levels in Fe-bearing minerals and glasses. American Mineralogist, 89, 57-63.

Yang, Y. H., Wu, F. Y., Yang, J. H., Chew, D. M., Xie, L. W., Chu, Z. Y., Zhang, Y. B., Huang, C. 2014. Sr and Nd isotopic compositions of apatite reference materials used in U–Th–Pb geochronology. Chemical Geology, 385, 35-55.

Zhang, C., Koepke, J., Wang, L. X., Wolff, P. E., Wilke, S., Stechern, A., Almeev, R., Holtz, F. 2016. A practical method for accurate measurement of trace level fluorine in Mg- and Fe-bearing minerals and glasses using electron probe microanalysis. Geostandards and Geoanalytical Research, 40, 351-363.